2020

A Physical and Numerical Study of an Interconnected Wave Energy Array

Howey, Ben

http://hdl.handle.net/10026.1/15773

---

http://dx.doi.org/10.24382/393
University of Plymouth

UNIVERSITY OF
PLYMOUTH

A Physical and Numerical Study of an Interconnected Wave Energy Array

by

Ben Howey

A thesis submitted to the University of Plymouth
in partial fulfilment for the degree of

DOCTOR OF PHILOSOPHY

School of Engineering

April 2020

UNIVERSITY OF
PLYMOUTH

A Physical and Numerical Study of an Interconnected Wave Energy Array

by

Ben Howey

A thesis submitted to the University of Plymouth
in partial fulfilment for the degree of

DOCTOR OF PHILOSOPHY

School of Engineering

April 2020

Acknowledgements

FIRST and foremost, I would like to thank my supervisory team who has supported me tirelessly throughout my studies at the University of Plymouth. Their expert guidance has been called upon on countless times and they have helped steer me when stuck in the research doldrums. I would like to thank the technical staff in the COAST Laboratory for their patience and dedication during experimentation and often meeting very tight deadlines. Finally, I would like to thank my soon to be wife for putting up with my midnight "eureka" moments as I figured out problems, and my parents for their constant support, both financially and emotionally.

Declaration

At no time during the registration for the degree of Doctor of Philosophy has the author been registered for any other University award without prior agreement of the Doctoral College Quality Sub-Committee.

Work submitted for this research degree at the University of Plymouth has not formed part of any other degree either at the University of Plymouth or at another establishment.

Word count for the main body of this thesis: **31,213**

Signed: ______________________

Date: ______________________

Posters and conference presentations:

Howey, B. & Collins, K. & Vicente, P. & Gomes, R. & Harnois, V. & Hann, M. & Iglesias, G. & Greaves, D. *A Physical Mooring Comparison for a Floating OWC* EWTEC Cork, Ireland, 2017

Howey, B. & Iglesias, G & Collins, K. & Hann, M. & Greaves, D. & Gomes, R. & Henriques, J. *Wave Energy Converter Arrays: Motion response of inter-connected arrays* ReNEW, Lisbon, Portugal, 2018

Howey, B. & Collins, K. & Vicente, P. & Gomes, R. & Harnois, V. & Hann, M. & Iglesias, G. & Greaves, D. *D6.1 - Analysis of different potential configurations for non-rigid inter-moored devices* WETFEET, 2016

Howey, B. & Collins, K. & Arber, P. *D6.3 - Report on the 1:40 scale models* WETFEET, 2017

Harnois, V. & Collins, K. & Greaves, D. & Howey, B. & Portillo, P. & Gomes, R. & Vicente, P. & Vicente, M. *D6.4 - Validated numerical simulation of hydrodynamic interaction between devices for different compact array layouts.* WETFEET, 2017

Collins, K. & Howey, B. & Greaves, D. & Hann, M. & Iglesias, G. & Gomes, R. & Harnois, V. *D6.5 - Design guidance on the use of shared mooring systems in compact arrays* WETFEET, 2018

Abstract

KEY to the progression of the wave energy extraction sector is reducing capital costs whilst maintaining or improving energy extraction efficiency. To achieve this, multiple devices in farm configurations, known as arrays, are likely to be developed. Mooring and anchorage systems of large scale arrays have been highlighted as notable contributors to high structural costs. To minimize the number of anchors required, and thus the cost, one option is to interconnect devices within the arrays. The implication on array performance and line tension of this mooring design needs to be understood to realize the true possibility for cost reduction. Large scale physical tests were performed in the COAST Laboratory at the University of Plymouth. An array of five individually moored oscillating water column type wave energy converters (WEC) were initially tested in operational and extreme conditions, followed by four interconnected designs of reducing levels of interconnectivity. Results showed considerable performance implications due to the interconnecting of devices, with a 75% increase in annual yield for all levels of connectivity, relative to the individually moored control case. The performance enhancement was attributed to the interconnecting moorings altering the system resonant frequency, resulting in a beneficial phase difference between the water column and the device. Whilst the overall array performance was not significantly effected by the level of connectivity the spatial variation in power distribution within the array was. The fatigue line loading experienced by the interconnecting lines in operational states showed beneficial results compared to that experienced by the individually moored array. However, in extreme sea states, some interconnecting and seabed lines displayed higher extreme loads compared to the individually moored array and so would require a higher strength material, incurring possible higher costs. Due to the improved fatigue characteristics of the interconnected arrays during operational conditions, these higher performance lines required would likely have an increased service life that requires complex cost modelling. This thesis demonstrates a beneficial potential for interconnected WEC arrays worthy of further investigation.

Contents

9 Appendix

List of Figures

List of Tables

Nomenclature

α	Attenuation parameter [-].
β	Ratio of measured to nominal RAO [-].
δ	Displacement [mm].
$\hat{P}_{lim}$	Maximum power available to an ideal heaving point absorber within a linear array [W].
λ	Scaling factor [-].
$\overline{P}$	Time averaged power with subscripts *dev*, *array* or *iso* for a device within an array, total array power output or an isolated device respectively [W].
ρ	Fluid density $[kg/m^3]$.
σ_*	Root mean square with subscripts T and w for mooring load and surface elevation respectively.
θ	Angle between linear array and wave front [degrees].
ε	Efficiency
ξ	Damping equivalent $[s^{-1}]$
ζ	Surface elevation [mm]
A_∞	Added mass at infinite frequency [kg].
A_{wp}	Water plane area of device $[m^2]$.
B_{33}	Damping in heave direction [kg/s].
C_{33}	Hydrostatic restoring force in heave [N].
C_D	Discharge coefficient [-].

C_g	Wave group celerity [m/s].
CW	Capture width [m].
CWR	Capture width ratio [-].
E	Energy [Wh]
F	Force [N].
f	Frequency [Hz].
F_b	Buoyancy force [N].
f_c	Cavity resonance frequency of an OWC [Hz].
F_e	Excitation force [N].
F_m	Mooring force [N].
F_{PTO}	PTO force [N].
f_p	Peak frequency [Hz].
F_{rad}	Radiation force [N].
F_v	Damping force [N].
f_z	Body resonance frequency of an OWC [Hz].
g	Acceleration due to gravity - assumed to be 9.81 [m/s^2].
H	Incident wave height [m].
h	Planck constant
H_{mo}	Significant wave height calculated from the zeroth spectral moment [m].
H_s	Significant wave height derived from a zero crossing time domain analysis [m].
I	Mass moment of inertia [kgm^2].
J	Occurrence matrix [%].
K_r	Impulse response function

l	Array Spacing [m].
L_1	Draught length [m].
$L_1^{'}$	Effective length [m].
L_m	Length at model scale [m].
L_p	Length at prototype scale [m].
L_w	Wavelength [m].
M	Moments [Nm].
m	Device mass [kg].
m_n	Spectral moment of the n^{th} degree.
m_w	Device added mass [kg].
N	Number of devices within the array [-].
N_c	Number of cycles to failure [-]
p	Differential pressure [Pa].
P_*	Power output with numbered subscript relating to the device number [W].
P_{95}	95% confidence interval.
P_{lim}	Maximum power available to an ideal heaving point absorber [W].
Q_*	Volumetric flow rate with subscript I or C for incompressible or compressible flow conditions [m^3/s].
q_*	q factor with subscripts 0 for relative to an isolated device or A for relative to the central device of configuration A. Subscripts b and f are used to represent the front and back of an array [-].
R	Ratio of cyclic stress to ultimate tensile stress [-].
RAO_*	Response amplitude operator with subscripts 1-3 for translations surge, sway, heave respectively [-] and subscripts 4-6 for rotations roll, pitch and yaw [deg/m] respectively.
S	Spectral energy density [m^2/Hz].

T	Mooring line tension [N].
t	Time [s].
T_c	Ratio of root mean square mooring line tension to root mean square of fluid surface elevation [N/m].
T_0	Mooring line pre-tension [N].
T_e	Energy period [s].
T_m	Average cyclic mooring load calculated from a zero crossing analysis [N].
T_N	Natural period of oscillation [s].
T_p	Peak period [s].
V	Volume [m^3].
W	Device width [m].
W_n	Device weight [N].
Z_{cg}	Position of the centre of gravity [mm].

Abbreviations

CAPEX capital expenditure

DFT Discrete Fourier Transform

FFT Fast Fourier Transform

LCOE levelized cost of energy

NIDAQ National Instruments data acquisition chassis

PM Pierson-Moskowitz

RAO response amplitude operator

rms root mean square

WEC wave energy converter

WG wave gauge

1

Introduction

The introduction chapter aims to provide a broad overview of the potential wave energy resource and why wave energy is a commodity worthy of focussed research. Previous work on wave energy device costs is summarised, before experimental and numerical studies relating to single devices, Wave energy converter (WEC) arrays, interconnected arrays and moorings are discussed. To conclude the chapter, knowledge gaps are identified to provide the aims and objectives of this thesis.

1.1 Wave Energy Resource

Ocean gravity waves are the transmission of energy propagating away from a source. These sources can include radiation from submerged bodies, seismic activity, celestial gravitational fields and local winds [1]. The latter are often described as a concentrated form of solar energy due to local wind fields being generated by thermal gradients caused by the sun [2]. Due to the relative densities of each medium through which the energy is transferred, the power intensities from solar to wind to wave increase approximately ten-fold [3]. The characteristics of the wave field are determined by the strength, fetch (the distance over which the wind transfers energy to the sea surface) and the duration of the storm [1]. These parameters determine the period and wave height, which in turn determines the energy transported and available power within the wave field [2]. Wave energy as a global resource, within a 30-nautical mile zone of land masses capable of extracting energy (i.e neglecting the poles), has been quantified at 2.11 ± 0.05 terawatts (TW) within a 95% confidence interval [4], as shown in Figure 1.1.

If one uses figures for 2015 global energy consumption provided by International Energy Statistics of 13,761 mega tonne of oil equivalent (Mtoe)(160,040 TWh), one can estimate an average annual power consumption of 18.27 TW [5]. Thus, recent estimates show the global wave energy resource has the potential to supply ≈12% of the global energy demand. This figure is concurrent with the findings of the 2010 Survey of Energy Resources [6].

Within the UK, the practical and economic tidal and wave resource has been valued at 20% of the current UK electricity demand [7]. The wave re-

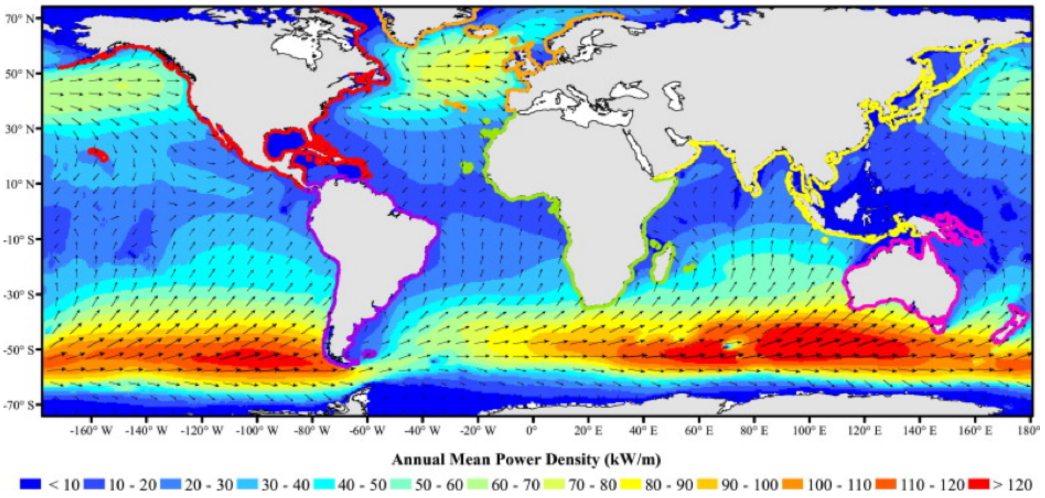

Figure 1.1: The global wave power resource with the 30 nautical miles extractable boundaries [4]

source is less variable than that of wind on an hourly basis and can be forecast accurately four days in advance relieving some of the pressures on the national power network compared with other types of renewable energy source. Due to increased resource during winter months, wave energy extraction also boasts increased supply during seasonally higher demand periods [8]. These benefits provide the UK with potential to reduce the dependence on imported non-renewable resources, as well as making considerable contributions to the long-term climate change objectives [7].

1.2 WEC Arrays

As wave energy device technology becomes more developed, research is looking beyond single deployments and towards multiple devices arranged in close proximity to one another. Wave farms of this nature allow the developer to improve the energy extraction per unit of capital. This is achieved through cost saving with regard to moorings, electrical architecture and maintenance. Another notable benefit of array deployment is from the realization that radiated and reflected wave fields within the farm could be extracted by neighbouring devices, resulting in a total power output not directly proportional to the number of deployed devices. The spacing and shape of arrays will be dependent on many factors including the site characteristics of the proposed deployment site, the device operating principals, mooring limitations and cost [9].

1.2.1 Physical Experiments - Arrays

The literature on physical testing of wave energy converter arrays is limited. In order to further the knowledge of inter-array effects, the WECwakes project was set up by the hlUniversity of Ghent to test near-field effects between the converters and far-field effects on other users [10]. A large scale physical experiment was carried out on a point absorber farm of up to 25 devices in various configurations and sea conditions [11]. To simulate the inertia of a PTO system, a friction brake comprising of PTFE blocks held in place against a heave shaft with four linear springs was used as shown in Figure 1.2.

The heave motion of the point absorber was measured in varying conditions with a potentiometer. The array configurations tested become gradually more complex, beginning with a single device leading to a 5x5 staggered case. A total of 41 resistive type wave gauges were used to monitor surface elevations inside and outside the array. Regular, irregular and diffraction cases were tested, with the latter being achieved through locking the WECs in position allowing no motion response. Effects on the wave field due to the

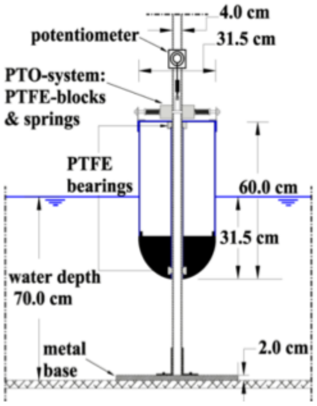

Figure 1.2: A cross section of the point absorber and fraction brake used in the WECwakes project [11].

presence of the varying geometric configurations of array are presented as a percentage of the original wave field. For the 5x5 array, a wave field attenuation of up to 18.1% and 20.8% was found in the lee of both the linear and staggered configurations respectively. Furthermore, the wave field alterations within the array were found to be highly dependent upon the configuration geometric layout, WEC spacing and the number of WECs [12]. Repeat runs indicated a ±10% variation in measured power output. An interaction factor q was used as a measure to quantify the intra-array interactions on the array output as shown in Eq. 1.1.

$$q = \frac{\sum_{i=1}^{N} P_i}{NP_0} \tag{1.1}$$

where N is the number of devices in the array, P_i is the power output of the i^{th} device and P_0 is the power output of an isolated device.

From Eq. 1.1 it can be noted that when the average WEC power from the array is greater than the power output of a single device (in isolation) the q factor will be greater than unity due to the intra-array effects. In the case of a 5x5 rectilinear arrangement, it can be seen from Figure 1.3 that almost 50% of WECs displayed constructive array effects ($q > 1$) within the interior of the array, with the remaining destructive array interactions ($q < 1$) affecting the front and rear devices. Similar results were found in 1:25 scale testing of an array of Seaforce Energy Converter point absorbers in Crews Bay, Trinidad, where the array performance was found to be dependent on the number of WECs and the geometry of the array [13].

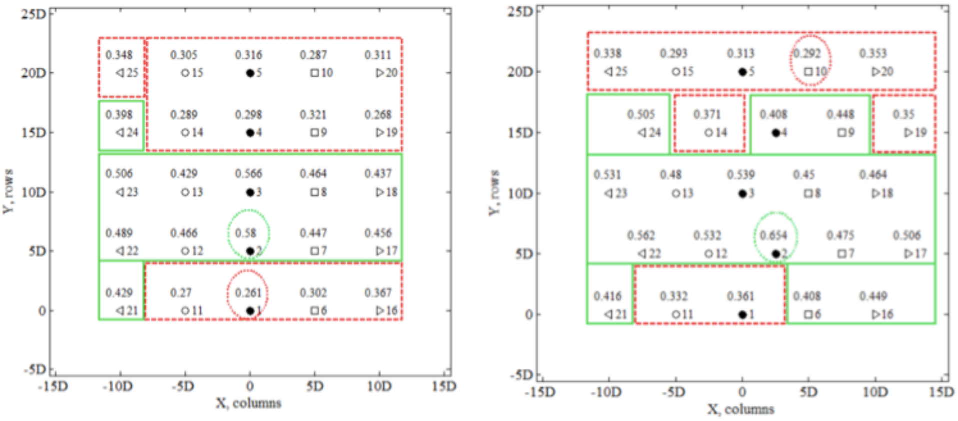

Figure 1.3: Absolute time-averaged instantaneous power of each WEC in a 5x5 rectilinear (a) and staggered (b) configuration tested in irregular long crested sea states ($H_{mo} = 0.104m$, $T_p = 1.260s$). Green and red box outlines indicate higher and lower power outputs than an individual isolated device (0.374W) respectively and circle outlines indicate the maximum and minimum. Waves propagate in a positive Y direction [12]

The q factors for the columns and rows were calculated separately. The results indicate that the number of columns did not significantly affect the array performance (ranging from -6% to +16% of q=1). Conversely the q factors by row indicate a large variation (-16% to +31% of q=1), indicating that the array performance is linked to the number of rows. In the case of the linear staggered array, the percentage of constructive interactions increases to 60% and a total q factor of 1.160, compared to 1.029 of the rectilinear array. Results show that the staggering of row 2 and 4 significantly optimizes the row q factor for all rows [12]. This technique of array performance evaluation will be useful during experimental stages of the project, as well as indicating that a staggered array configuration would be more suitable for physical testing than a linear configuration.

Array spacing has also been found to have large impact on array performance, indicated by q factor of 0.802 for a 3x3 array of five device diameter (5D) spacing, compared to a q factor of 1.684 for a 10D spacing of identical layout and testing conditions. This suggests the existence of an optimal spacing by which constructive interactions can be utilized before the spacing becomes so great that the devices are essentially isolated [12].

Flexibly moored arrays have been investigated as part of the EU Hydralabs III initiative to validate numerical models in operational conditions [14]. $1/20^{th}$ scale physical tank tests were carried out on a 3x2 staggered array of five close-packed OWC devices. Mooring line loads, device motion, acceleration and differential pressure were measured in regular and irregular conditions (short and long crested). An adjustable damping orifice plate, similar to a spear valve, was fitted to each device, as well as an internal wave gauge to measure surface elevations within the cylinder. Results suggest that line tensions within a multiple WEC array are considerably higher (double in some cases) than a single isolated device, but less frequent [14]. This is concurrent with the findings discussed above of improved average device efficiencies due to constructive array interaction resulting in higher mooring loads in the moored case. There will be a point at which high line loads will cause a project to become non-viable unless the loading can be mitigated through higher levels of interconnectivity.

1.2.2 Numerical Models - Arrays

Numerical studies of wave energy converter arrays are vital at early stages of the design process to understand how the body interactions will effect the performance of the array. As covered in Section 1.2.1, these interactions can make significant differences to the behaviour of devices. Once the numerical model for a single device has been validated, the next step is to model the device within an array. The influence of separation distance on array performance has been of particular interest in the field of numerical modelling of wave energy converter arrays. A parametric study using a linear potential flow BEM code was carried out to investigate the effects of separation distance and layout on two arbitrary geometry arrays [15]. To simplify the problem, the PTO was modelled with a linear damper, and a theoretical deployment site of Yeu island, France. Irregular sea states were simulated in the frequency domain by multiplying the power spectra by the incident wave field energy density spectrum. The yearly yield was then considered as the sum of the energy extracted for all possible sea states within the year. The separation distance parameters can be seen in Figure 1.4a. It can be seen from Figure 1.4b that an an optimum exists for the cylinder being analysed. The PTO damping was found in this study to be better calibrated from the annual energy production rather than the power at the device resonant frequency and was shown to significantly alter the annual energy extraction and intra-array effects. Furthermore, when designing an array, as previously discussed triangular/staggered layout is beneficial to energy extraction due to minimized shadowing in the lee of other devices [15]. The PTO system has also been shown to be a contributing factor to the effect of the separation distance on array performance [16]. It was found that the device separation distance effects became greater as the hydraulic system pressures increases. Furthermore, the frequency array of peak efficiency was shown to be linked to the hydraulic PTO system pressure. Therefore, for any given sea state there was an optimum spacing and PTO pressure to maximize energy extraction [16].

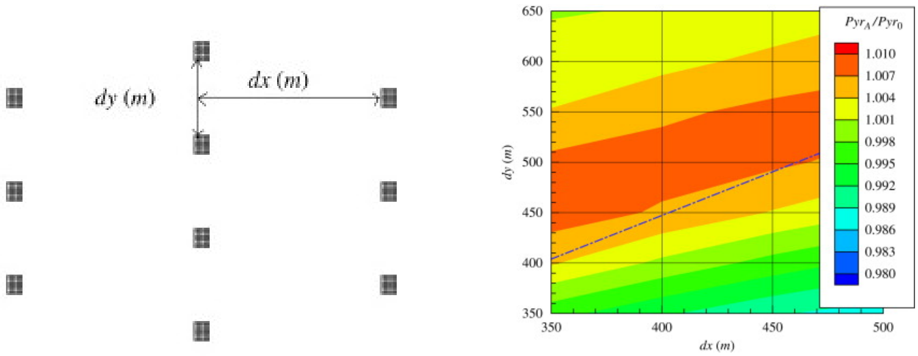

(b)

(a)

Figure 1.4: Array performance of an array of floating cylinders with varying seperation distances [15].

Similar dependency on the number of devices and array geometry was found in the power smoothing and power density benefits of large scale arrays in linear potential flow numerical models [17]. Rectangular and circular arrays of devices were compared to one another for measured sea states from a site 2 km offshore of Lysekil, Sweden. Significant array effects were predicted from both arrays. The rectangular geometry array was shown to outperform the circular array, however the spatial variance in power was greater [17].

These studies have been carried out neglecting non-linear system components such as moorings. It has been shown that the PTO characteristics, array layout and device separation distance significantly alter array responses, so one could suppose that the moorings and interconnection characteristics could also cause similar alterations to the device responses.

1.3 Interconnected WEC Arrays

1.3.1 Physical Experiments - Interconnected Arrays

The influence of interconnection has recently been tested to validate numerical models and investigate the potential to improving performance and reducing cost. Tests have been carried out in University of Plymouth Coast Laboratory on an array of three Sparbuoy devices interlinked as depicted in Figure 1.5, as part of the Marinet infrastructure access project [18].

A number of tests were carried out including the effect of changing the buoy and clump weight masses on the seabed lines (See Figure 1.6). The heavier weights and larger float configuration resulted in a stiffer system due to the increased pre-tension. The interlinking of the devices in an array configuration were found to reduce the power outputs for incident wave frequency equal to the single device natural period. However, higher power capture than obtained by a single device was observed at lower frequencies. These changes were attributed to the modification of the natural period of the system when moored [19]. In order to assess the contributions of each, the

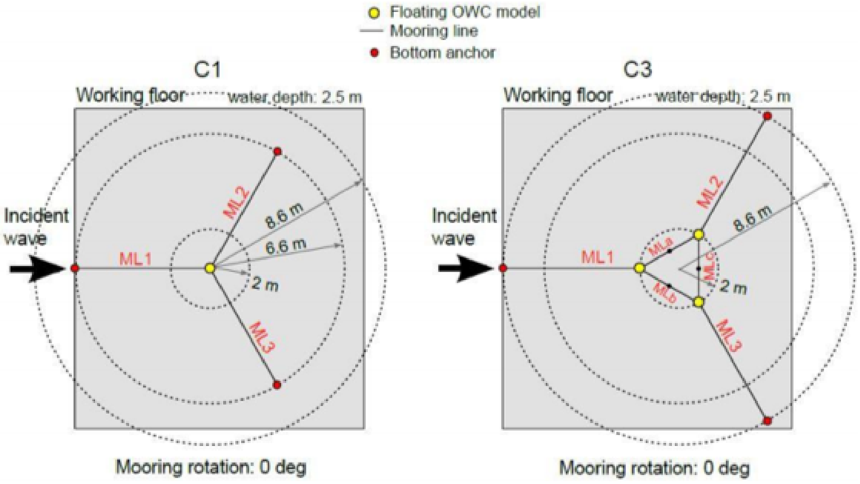

Figure 1.5: Isolated and array configurations tested in the Plymouth University COAST Laboratory by IST [18]

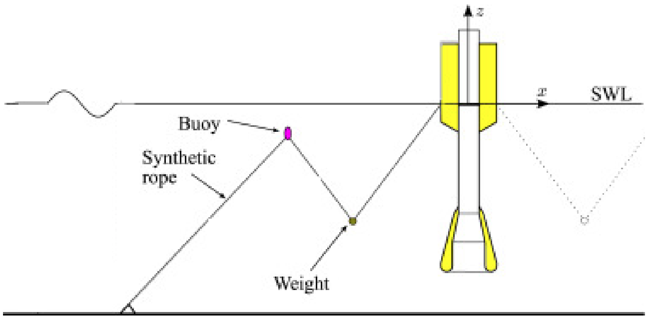

Figure 1.6: Seabed mooring configuration used for array testing [19]

array would need to be individually moored and then interlinked, comparing the performance and motion results.

With regard to mooring line tensions, it was found that in both isolated and array configurations, line ML1 (Figure 1.5) suffered the highest loading conditions. Large tension spikes and snatch loading were observed in both cases, resulting in fatigue damage to the point of failure. Due to load cell overload, it was not possible to determine maximum loading conditions, however due to the repeatability of snatch loading, analysis was carried out on the number of load spikes above a given threshold. The recorded data shows that the array configuration has little effect on the ML1 line tension, with only small differences noted in the magnitude rather than the number of spikes [18]. Further work into the level of inter-connectivity and the effect on line tensions would show how the load is being distributed, leading to an optimal level of connection, in which performance is enhanced and loading is minimized. Furthermore, the importance of suitable sensor selection for physical testing is highlighted.

Figure 1.7 shows an arrays of floating OWC type converters with taught leg and shared anchor points have been tested at the Norwegian University of Science and Technology [20]. The array effects on the performance and line loading was investigated on an array of five devices in a staggered linear configuration, similar to that tested in [12]. Complex device motion dynamics and associated tension characteristics were measured, particularly noticable by the front most devices and respective mooring lines. Results showed that the cyclic line tensions of the array configuration were greater (up to double) than that of an isolated device, but may be less frequent. Furthermore,

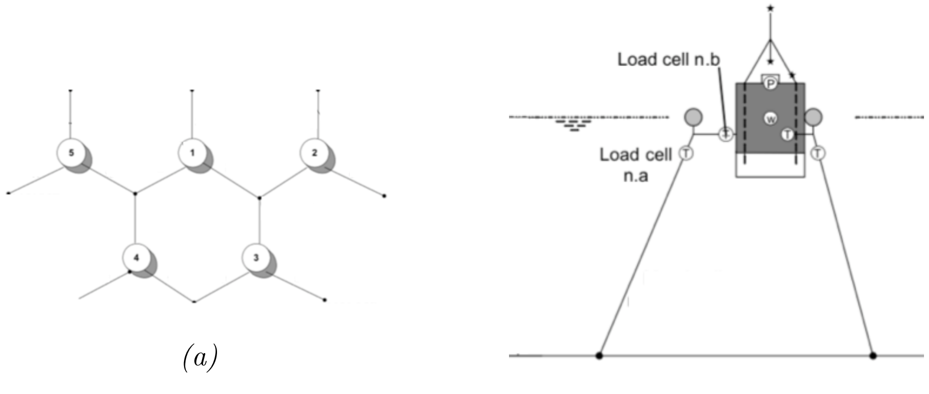

(a)

(b)

Figure 1.7: Taught leg mooring systems with shared components tested at the Norwegian University of Science and Technology [20].

results suggested that the greater the number of devices within the array, the greater the extreme loads but the lower the frequency of occurrence [20]. In terms of performance, array effects were measured, with identical devices extracting circa 6% more energy when situated within an array than an isolated configuration [21]. It is clear from this work that array effects alter the line tension and performance characteristics. The interlinking of devices to one another is the next level of increased connectivity and complexity to understand.

In the oil and gas sector the effect of the interlinking of semi-submersible platforms to slack moored spars has been investigated. The study showed a reduction of the surge, heave and pitch motion responses when the semi-submersible was rigidly tethered to the spar, however an associated increase in the spar mooring loads was also measured [22]. In the aquaculture industry, submerged interlinked fish cage grids have been tested at full scale in the Gulf of Maine over a seven year deployment period. The design comprised of a taut mooring system made from a combination of chain and polymer rope sections, secured to the seabed with drag embedment anchors. The structure was designed in a way to minimize motion responses in all degrees of freedom, with a maximum design load from a 50 year return period storm [23]. A study of the static mooring line tensions was carried out, where highest static mooring loads were noted in the interconnections rather than the seabed lines [24]. After the seven year deployment the structure was removed and the condition of the components remained relatively unimpaired, indicating that the concept of interlinked and shared mooring components is possible [23]. The transfer of this to the wave energy extraction field involves considering that the mooring design will need to allow motion responses in the power extraction degrees of freedom, whilst performing their station keeping duties.

1.3.2 Numerical Models - Interconnected Arrays

Numerical models have been used in order to investigate the possibilities of interconnectivity and geometric layout of point absorber arrays. Initial models consisted of three point absorbers, each with one seabed line and one line connected to a central clump weight as seen in Figure 1.8 [25].

The frequency dependent hydrodynamic coefficients for the device, added mass, radiation damping and exitation forces, were calculated using WAMIT in order to compute the motion responses. The central clump weight (body 4) was not included in the hydrodynamic calculations, and so does not impart any radiation damping or excitation force on the devices within the model. The added mass of the clump was modelled as an accelerating sphere in an unbound fluid. The mooring forces are resolved in a quasistatic manner as

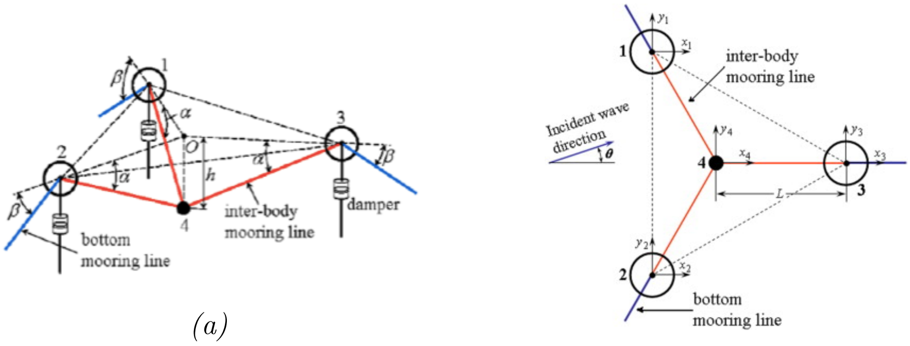

(a)

(b)

Figure 1.8: Perspective and plan view of the numerical interconnected point absorber array with the linear damping terms acting on each device [25]

a result of device perturbations in each respective degree of freedom. Comparisons have been drawn between individually moored, interconnected and unmoored cases with performance results shown with a q factor as defined in Eq. 1.1.

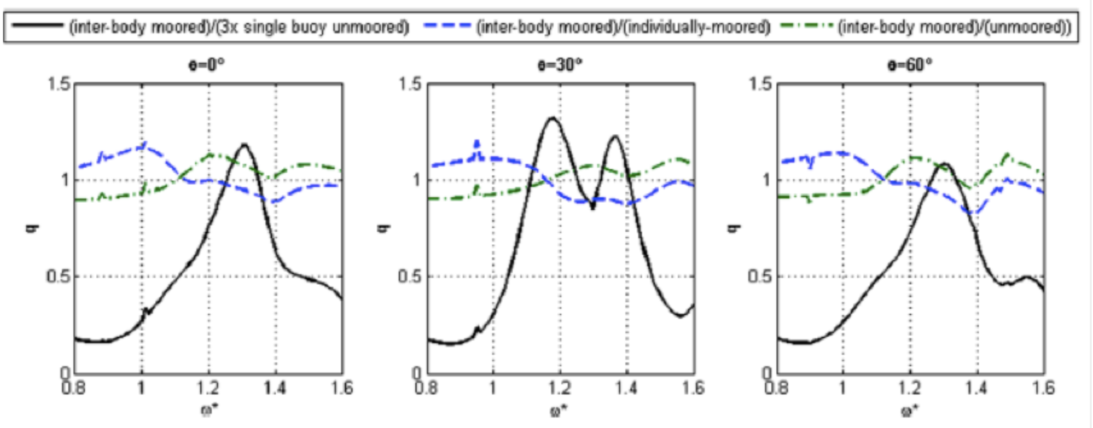

Figure 1.9: The q factor for the individually moored, interconnected and unmoored cases with varying incident wave angle [25].

It can be seen from the blue dashed lines in Figure 1.9 that the ratio of inter-body moored power to the individually moored case is reasonably inde-

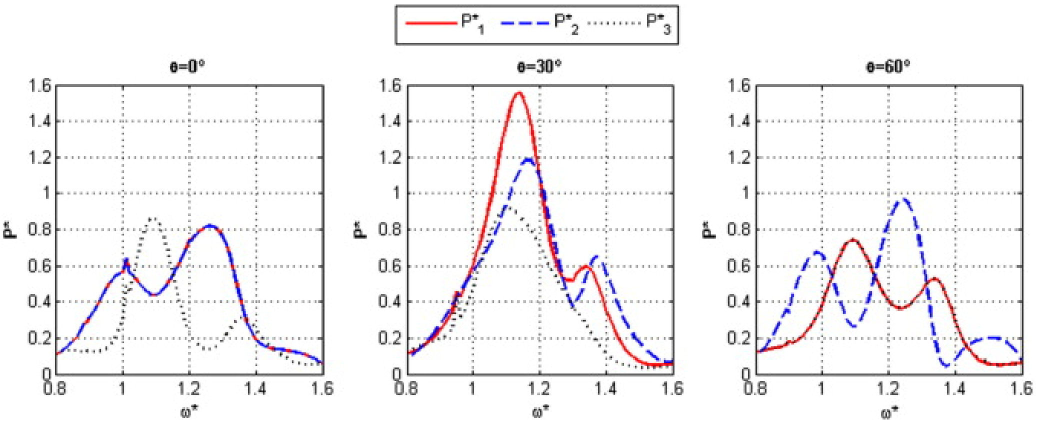

Figure 1.10: The dimensionless time averaged power output plotted against angular frequency, from device 1,2 and 3 for the inter-connected case [25]. Where two devices are normal to the incident wave the response is identical, hence only two lines appear when $\theta = 0°$ and $\theta = 60°$.

pendent of the incident wave angle. Furthermore, the inter-body moorings appear to enhance the power outputs at lower frequencies and the opposite effect at higher frequencies, indicating the possibilty to improve performance through inter-connection. Upon inspection of the individual device power output spectra, shown in Figure 1.10, it becomes clear that device 1 and 2 contribute a larger proportion of the array power output over the majority of the frequency space [25]. This is not in agreement with the unmoored/rigid structure array physical testing carried out by Stratigaki [12] as discussed in Section 1.3.1, although this could be due to the array spacing or the device type being tested. Although the findings from the Marinet tests are in agreement with the higher power outputs from the front device, the symmetry between power outputs within rows is not correlated [18]. Line tensions and the mitigation/minimization of load through increasing the interconnectivity was not considered as part of the numerical study, but would play an important role in the realization of any interconnected array designs.

Shared anchor systems for arrays of multi-body point absorbers have been considered as part of a levelized cost of energy (LCOE) study [26]. Only the diffraction induced hydrodynamic interactions were considered in the study comparing four different array configurations of 10 WECs, two of which utilize shared components (See Figure 1.11a). To simplify the model a linear damper was used to represent the PTO and a time averaged absorbed power was calculated for two of the most probable sea states for the deployment site of Rundle, Norway (Figure 1.11b). The fatigue damage to the mooring lines was considered with a stress based approach and compared to an isolated device case. The mooring line cost was then considered linearly proportional to the ratio of the fatigue damage in an array case to an isolated case.

The shared anchor system of the star configuration yields an increased average power output of 3% for seastate two, although it can be seen from Figure 1.11b that there is a greater variation in device power outputs compared to configuration A which has a larger device spacing and no shared anchors [26]. A similar approach was undertaken for the line tension characteristics and similar finding was concluded: there is more variability for the compact array with shared anchors than the array with a larger device spacing and no shared components. Due to the linear assumptions of cost and fatigue damage, a similar effect on the LCOE was concluded, however the extra cost required for heavier gravity anchors for tethering multiple devices was not considered in this study [26]. This research provides the grounding for the potential of improved performance through the utilization of shared components. To further this work, increased levels of interconnec-

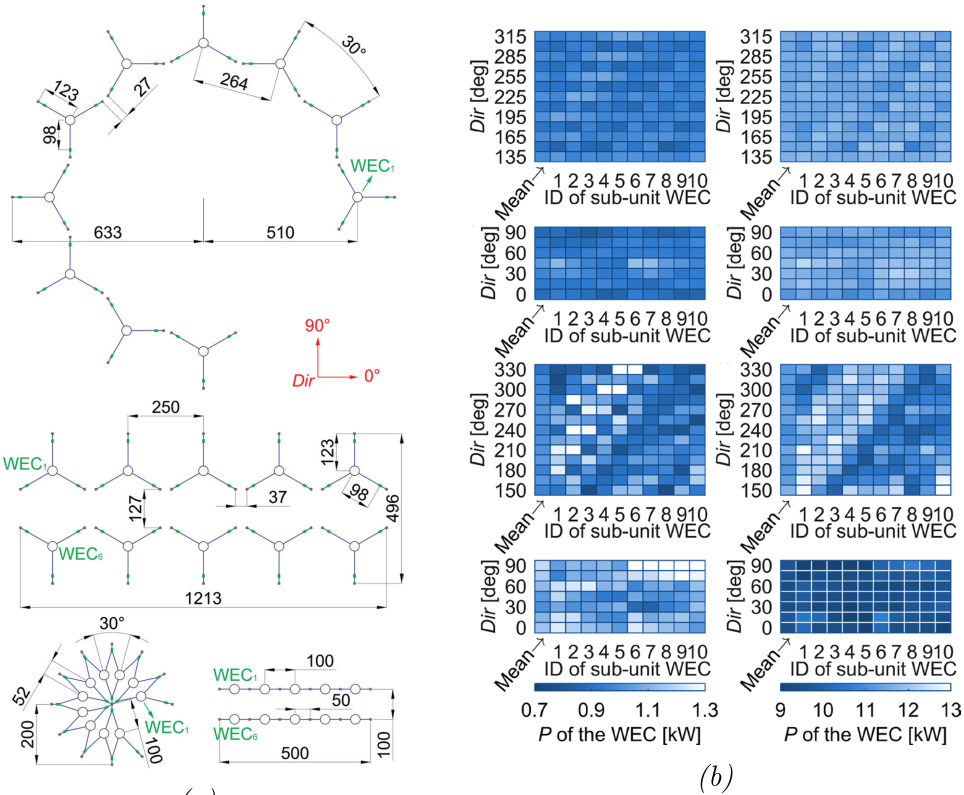

(a)

(b)

Figure 1.11: The numerically tested array configurations (a) and the time averaged power outputs for each device within the arrays, with their respective total average, for varying incident wave angles. The two columns are outputs for two sea states and the rows are for each respective array configuration [26].

tivity directly to other devices, provides the next step into cost reduction and performance implication studies. Physical testing would further strengthen these numerical predictions.

From the aquaculture case described in Section 1.3.1, a finite element time domain model was designed in Aqua-FE to determine the hydrodynamic loading on the structures. Float masses and numbers of seabed lines were altered on account of the numerical predictions and mooring lines were designed in a way that the anchor would be the 'weak link' in the system to prevent component damage. Complex mooring load distributions were noticed from the interior grid to the seabed lines [27]. The understanding of the mooring load distribution within an interconnected array is of utmost importance in the design of an interconnected WEC array as the dynamic loading is likely to be greater than that noticed in the aquaculture industry, due to the requirement of the WEC to move.

1.4 WEC Economics

It has been highlighted that high capital expenditure (CAPEX) and LCOE are slowing progression in the wave energy sector [28]. The LCOE is defined as the net present value of the unit-cost of electricity over the lifespan of the project. Wave energy extraction project costs are device specific and due to the lack of operational experience, there is limited data to validate cost models. Currently, the most optimistic predictions of LCOE for wave energy is between \$0.12/kWh and \$0.47/kWh, whilst wind and solar are currently between \$0.03/kWh and \$0.22/kWh [29]. It is therefore vital that costs are reduced and performance is improved to make wave energy more economically viable. As previously mentioned, multiple device WEC arrays benefit from economies of scale reducing the CAPEX and therefore the LCOE, however the mooring and installation costs will increase. Structural, mooring systems and installation costs have been identified as the main cost drivers [29], where they can comprise as much as 24% of the device costs [30]. Furthermore, the number of anchors required has implications for the vessel type required for deployment, which can have significant effect on the costs.

1.5 Mooring Design for WECs

Wave energy device performance is dependent upon the device characteristics and environmental conditions. The device characteristics are dependent upon the mooring system, which needs to be designed to survive the environmental conditions. It is therefore apparent that the mooring and device form a coupled system that needs to be designed concurrently. The mooring system is required to carry out the following important functions:

- Limit mean displacement of the floating structure on station in the wave direction within a standardised tolerances under normal operational and extreme conditions.
- Maximum mean displacements must not permit high loads on electrical umbilicals or allow a device to enter the radius of another when situated within an array.
- Where directionally dependant devices are used, the system must align the principal axis of the device with the oncoming wave crest.
- The system must be sufficiently compliant to minimize the forces on the

device and the anchor points where designed not to (i.e drag anchors).

- The mooring must be compliant enough to withstand tidal range differences without having a significant effect on the device performance or line loads.
- The system should require minimal maintenance.

These factors should all be considered within an iterative design process to optimize the mooring and device to maximize performance and survivability, whilst reducing cost as far as reasonable [31].

As devices move further offshore to utilize the greater resource described in Section 1.1 the mooring requirements change and often become more complex and expensive. These moorings are often substantial and interact strongly with the energy extraction method being utilized. Moorings can be sub-categorized into static or dynamic station-keeping systems. Where a mooring system directly connects to a body whose efficiency is dependent on its motion, a dynamic mooring system must provide sufficient freedom to the energy extraction modes whilst minimizing others. In the case where the body moves relative to a stationary platform, a static mooring can be used where the stiffness characteristics will not affect the extraction efficiency [32].

Economic considerations for wave energy installations suggest that arrays of devices in farms of densely packed clusters could improve power extraction whilst reducing outage risk, compared to isolated devices. As a result, the footprint of the mooring systems need to be minimized, whilst minimizing the vertical loads on the devices. The minimum length of chain required for a catenary system is proportional to the water depth. In order to prevent sinking the device, suitably light weight chains are required, resulting in very long chains to provide sufficient resorting forces to keep the device on station. As a result, semi-taut and taut mooring configurations have been suggested for densely packed arrays [33]. The addition of in-line clump weights and floats can be used as a suitable compromise to exploit the beneficial restoring force attributes of the catenary chain, whilst providing improved flexibility from using Nylon rope sections and the extra restoring forces from submerged floats [34]. The damping effects of mooring line design have been extensively researched at laboratory and full scale, with the damping being proportional to the enclosed area within the hysteresis loop of a load displacement plot (Eq. 1.2), where F_T is the line tension δ is the fairlead displacement as a function of time.

$$E = \int_{t}^{t+T_n} F_m \frac{d\delta}{dt} dt \tag{1.2}$$

Full scale experiments have been conducted in [33], comparing the mooring line damping of a pure chain catenary, a hybrid rope/chain catenary and an S-shape line with float and sinker sections (See Figure 1.12). The damping properties of each line were calculated using the integral in Eq. 1.2 with force displacement data, as shown in Figure 1.13.

Findings from the experiments highlighted a link between the pre-tension and the surge amplitude on the damping properties of the mooring systems. When the damping is scaled with respect to the pre-tension and water depth, the damping is linearly proportional to the surge amplitude. This linear trend showed that the S-shaped line provided lower damping with respect

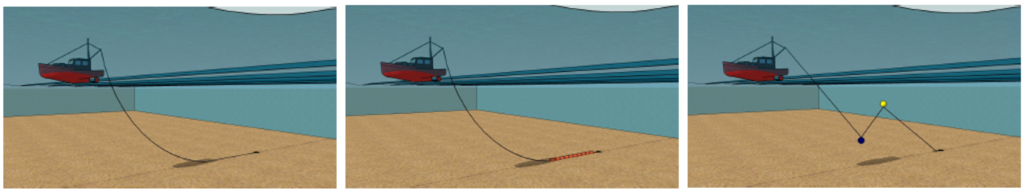

(a) *(b)* *(c)*

Figure 1.12: Three types of mooring configuration tested at full scale to assess the damping characteristics of each [33]

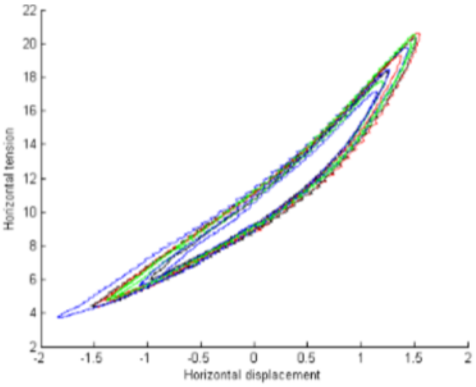

Figure 1.13: Mooring line force displacmeent plots with damping being proportional to the enclosed areas, as shown in Eq. 1.2 [33]

to the surge amplitude when compared with a pure chain catenary and the chain/rope hybrid line [33].

The dynamic characteristics of the mooring lines is incorporated within the numerical modelling part of this research. In order to represent the loading conditions experienced by the seabed and interconnecting lines, a time domain solver such as MoorDyn or OrcaFlex will be investigated. Furthermore, the literature suggests that not only could S shape seabed mooring configurations be utilized to minimize the spacing between devices within an array, they could offer performance benefits also.

1.6 Literature Knowledge Gaps

The literature has highlighted that the use of shared mooring systems poses a potential to reduce the capital costs of wave energy converter arrays, thus reducing the LCOE of a development and encouraging progression in the wave energy sector. A gap in the literature has been identified regarding the effects of the level of interconnectivity between devices within interconnected arrays and the implications on performance and line loading. The litterature review has highlighted that published data on the performance and response of physically tested interconnected arrays is limited. Although physical studies have been carried out [18] on interconnected arrays, there is no control configuration of a similar array individually moored with which to compare results. This is a vital step in isolating the effects of the interconnecting moorings from the array effects. Such information will provide valuable data for the validation of numerical tools from which optimal interconnected arrays can be developed.

1.7 Aims

- To establish the extent to which alternative interconnected moorings could affect power production and mooring line load and hence overall economic viability of a wave energy array.

1.8 Objectives

- Design and build an interconnecting mooring system to provide similar stiffness characteristics as the individually moored case.
- Experimentally test the effects on performance and survivability of the interlinking of devices within a wave energy array of floating OWCs.
- Establish the impact of hydrodynamic interactions amongst a small array on the average device response and power output.
- Quantify the impact of interconnected moorings on device response, power capture and energy yield relative to arrays with single moorings.
- Quantify the design loading of alternative interconnected mooring lines to inform assessment of capital cost.

1.9 WETFEET

This research project has been carried out in parallel with WETFEET, a Horizon 2020 EU funded programme designed to provide vital breakthroughs in the wave energy sector. Partners of the project include multidisciplinary teams from Instituto Supererio Technico (IST), WaveEC... Outcomes from the project highlighted the potential for the use of inter-connected mooring systems within compact arrays. This thesis builds upon those findings by investigating further some of the experimental results and their impact on the financial viability of interconnected concepts.

2

Background Theory and Principles

The key equations of linear wave theory and the fundamentals of wave energy extraction are presented. Typical wave energy device designs and mooring configurations are discussed to give the reader a baseline to contextualise the interconnected array experiments that form this research.

2.1 Wave Energy Technology

2.1.1 Physical Models - Single devices

Wave energy extraction is not a new concept. There have been many devices that utilize wave energy to power on-board systems such as lighting, pumps and isolated battery charging units. The most significant designs can be found in navigation buoys, where wave energy powers the marker lighting [35]. Early patents of wave energy extraction date back as far as 1799, when Girard and his son patented a design to mechanically capture wave energy to drive pumps, saws and other machinery [36]. Several early designs were developed from this point, with a notable device being patented in 1898 by Wright with his system, 'the wave motor'. Similar to the concept of Girard, the device consisted of a floating section secured at a distance from a fulcrum. The motion was then used to drive a hydraulic system to do useful work [1]. A second notable historical design came also from France, constructed by Bouchaux-Praceiques, utilizing a different energy extraction technique, using a pressure differential induced by incident waves. This was arguably the first OWC type converter to be constructed [1]. There has been little design convergence comparable to that seen in the wind sector, although many of the operating principles of today's devices can be related to the original designs of Girard and Wright.

The most common device types can be summarized as follows:

- **Point absorber:** These devices have a small geometry relative to the wavelength and come in many different forms. Due to their nature, wave directionality is often not important and they can operate on and below the sea surface. Electricity is generated from the relative motion of the floating section to a reference. Power take off can come in numerous forms including linear generators and turbines. There are many devices of this type being developed for commercial deployment, including the OPT Powerbuoy and the Seabased unit developed in connection with Uppsala University [37].

- **Attenuator:** These devices lie parallel to the oncoming wave field, extracting energy from linkages between bodies. The attenuator is perhaps the most well-known wave energy device in the UK due to the high media attention gained by the Pelamis device. This device consisted of hollow tubes joined together with two degrees of freedom (similar to a universal joint). The relative motions of the tubes were then used to drive a hydraulic power take-off system [38].
- **Flap/Hinge Type Converter**: These devices are orientated perpendicular to the wave front and oscillate in the direction of the wave propagation. Often these devices are bottom mounted, some fully and some partially submerged. The Aquamarine Oyster is an example of a flap type converter that had two full scale prototypes in the water at EMEC until 2015 [39].
- **Oscillating Water Column (OWC):** These devices use the oscillating motion of the water during wave crest passage as a piston to drive air through a turbine. These systems can be subdivided into onshore and offshore. Onshore devices are generally located within sea defence units and there are several full-scale commercial devices

operating, such as the Mutriku on the Northern Spanish coast. Accessibility is one of the benefits of a shore-based unit, which has allowed for progress to be made regarding turbine optimization [40]. However, as seen in Figure 1.1 there is a greater resource offshore, hence the development of offshore floating devices. Furthermore, the lack of moving parts or the need for a gear box (due to the availability of low head turbines) and ease of maintenance also make this an attractive technology to be deployed offshore. OWC technology was originally utilized in a whistling buoy as far back as the 19th century, with 34 operating devices in 1885. The next notable development came half a century later by Yoshio Masuda, a Japanese naval commander who designed and installed a navigation buoy with lighting being powered by an on-board Wells turbine. These designs have developed into energy extraction and grid connected units with varying success. Notable devices include the Ocean Energy Buoy which logged 20000h of sea trials at quarter scale [37] and the Oceanlinx MK3 one third scale grid-connected device [41].

- **Overtopping device:** These devices capture water as waves pass into an elevated storage area, before being returned to the sea through a low-head turbine. Large scale prototypes have been fabricated, grid connected and deployed in the sea, most notably WaveDragon [42].

- **Submerged Pressure Differential** These devices are completely submerged below the surface and utilize the pressure gradient generated by the passage of a wave crest. The systems often include a fixed base unit and a movable float section that moves in relation to the pressure gradient. This reciprocating motion is then utilized to drive power take off units. The Archimedes Wave Swing is one of the leading devices of this type with optimization work currently being investigated on full scale prototypes [43].

- **Terminator:** These devices have their principal axis perpendicular to the oncoming wave field, with a floating section that interacts with the wave front. A notable terminator device is the Salter's Duck, developed within the Wave Power Group at the University of Edinburgh [38].

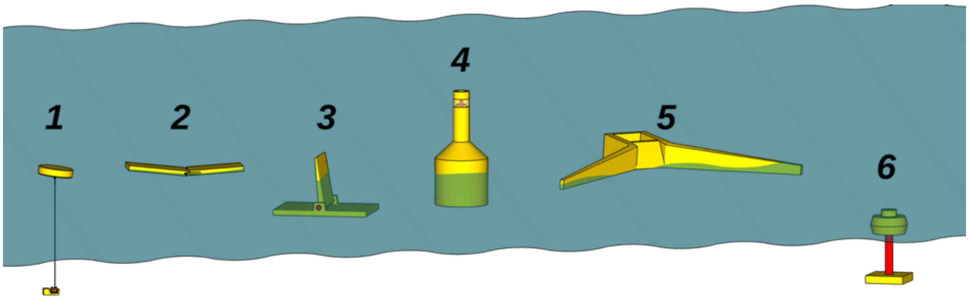

Figure 2.1: A selection of WEC designs. A point absorber (1). An attenuator (2). A flap type converter (3). An OWC (4). An overtopping device (5). A submerged pressure differential converter [3]

2.2 Mooring System Design - Single Device

The isolated device mooring design is a hybrid catenary line as shown in Figure 2.2. A previous taut mooring system design proved inaddequate to keep the device on station in other work [44]. Snatch loading was observed during testing [44] and so a section of chain was added to the design to provide a catenary restoring force as shown in Figure 2.2. The expected maximum loading on the devices was estimated from a 100-year return period wave, wind and current event.

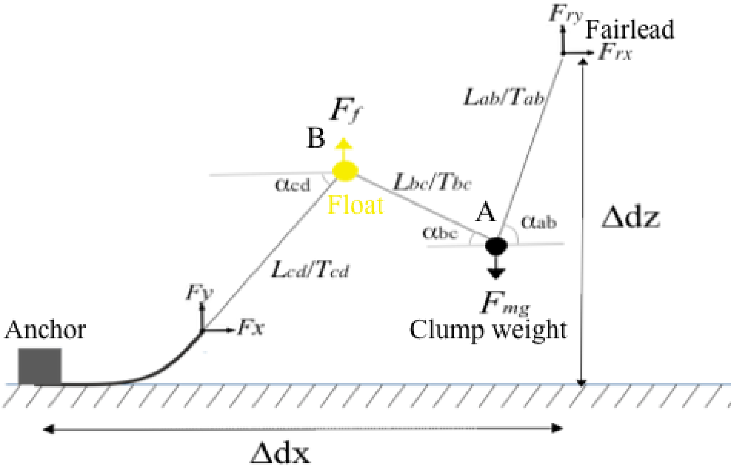

Figure 2.2: Static equilibrium diagram of the isolated device mooring system with a clump weight anchor at one end and the fairlead connection point at the other.

From the diagram shown in Figure 2.2 the following set of non-linear simultaneous equations can be set up from the geometric constraints and equilibrium of forces.

$$0 = T_{ab}sin(\alpha_{ab}) + T_{bc}sin(\alpha_{bc}) - F_{mg} \tag{2.1}$$

$$0 = F_f - T_{bc}sin(\alpha_{bc}) - T_{cd}sin(\alpha_{cd}) \tag{2.2}$$

$$0 = T_{ab}cos(\alpha_{ab}) - T_{bc}cos(\alpha_{bc}) \tag{2.3}$$

$$0 = T_{bc}cos(\alpha_{bc}) - T_{cd}cos(\alpha_{cd}) \tag{2.4}$$

$$\Delta dx = L_{ab}cos(\alpha_{ab}) + L_{bc}cos(\alpha_{bc}) + L_{cd}cos(\alpha_{cd}) + \left(L - \frac{T_{cd}sin(\alpha_{cd})}{w}\right) + \frac{T_{cd}cos(\alpha_{cd})}{w}sinh^{-1}(tan(\alpha cd)) \quad (2.5)$$

$$\Delta dz = L_{ab}sin(\alpha_{ab}) - L_{bc}sin(\alpha_{bc}) + L_{cd}sin(\alpha_{cd}) + \frac{T_{cd}cos(\alpha_{cd})}{w}\big(cosh(sinh^{-1}(tan(\alpha_{cd})) - 1\big) \quad (2.6)$$

All terms are defined in Figure 2.2. Equations 2.1 to 2.6 formed the constraints for an optimization to solve for the line lengths, clump and float masses. The optimization objective function was to maximize the surge restoring force for a maximum excursion of the fairlead of 0.375 m at model scale when fully loaded. This provided acceptable distances between devices in worst case scenarios, where devices surged and pitched towards one another. These quasi-static (Neglecting any dynamic effects) solutions are used to calculate an initial mooring design, which is subsequently tested in a time domain numerical model to assess the dynamic effects on the line.

2.3 Fundamentals of Wave Energy extraction and Linear Wave Thoery

2.3.1 Linear Wave Theory

To reduce the complexity of testing and to allow the use of frequency domain linear BEM codes, waves within a linear domain have been considered. The linear wave regime is considered applicable for waves of height to wavelength ratio of less than 1:50 [1]. Linear wave theory is derived from the continuity and Navier Stokes equations. The continuity equation is a mass conservation boundary condition, stating that any fluid density changes are proportional to mass flows into or out of a control volume. The Navier Stokes equation is a form of Newton's second law of motion. The following assumptions are accepted in the use of linear wave theory:

- The fluid inviscid.
- Incompressible and irrotational flow, thus assuming no shear stress at the sea-air interface.
- The wave amplitudes must be small relative to the wavelength and water depth.
- A linearized free surface.
- Gravity is the only force external acting on the fluid.
- The seabed is horizontal, impermeable, frictionless and stationary and does not add, remove or reflect any energy within the system.

Considering the assumptions above, the Navier Stokes equation is solved with a potential flow approach yielding the dispersion relation shown in Eq 2.7 that describes the relationship between the frequency and wavelength.

$$\omega^2 = gk \tanh(kh) \tag{2.7}$$

where ω is the angular wave frequency, $k = 2\pi/L_w$ is the wave number and h is the water depth. This allows for the derivation of the characteristic wavelength L_w as in Eq 2.8.

$$L_w = \frac{g}{2\pi f^2} \tanh \frac{2\pi h}{L} \tag{2.8}$$

where f is the incident wave frequency. The regular and irregular incident wave power per metre wave crest is defined as in Eq. 2.9 and Eq. 2.10 respectively.

$$P_{reg} = \frac{\rho g H^2 C_g}{8} \tag{2.9}$$

$$P_{irr} = \rho g \int S(f) C_g(f) df \tag{2.10}$$

where ρ is the density of water, g is the acceleration due to gravity, H is the average measured wave height measured in either the time or frequency domain (See Eq.2.12 and 2.14), C_g is the group celerity (the velocity of the energy transport - Eq. 2.11) and S is the spectral energy density which is typically obtained through a Fast Fourier Transform (FFT) of the measured incident wave time series.

$$C_g = \frac{1}{2}\left[1 + \frac{2kh}{\sinh\left(2kh\right)}\right] \tag{2.11}$$

In order to characterize and discretise sea states, the significant wave height and energy period of the spectrum is often used. The significant wave height is the average wave height of the highest third of waves over a given time. This is calculated in the time domain as shown in Eq. 2.12

$$H_s = \frac{1}{3^{-1}N_w} \sum_{n=1}^{3^{-1}N_w} H_n \tag{2.12}$$

where H_n represents the individual wave heights listed in descending order as n increases from 1 to N, or in the frequency domain, by calculating the 0^{th} moment ($n = 0$) of the spectrum as shown in Eq. 2.13 and 2.14.

$$m_n = \int_0^\infty f^n S\left(f\right)\,\mathrm{d}f \tag{2.13}$$

$$H_{mo} = 4\sqrt{m_0} \tag{2.14}$$

2.3.2 Fundamentals of Wave Energy Extraction

By definition, a good wave energy absorber is a good wave generator. Considering laws of the conservation of energy, in order to absorb energy from a seastate, the energy from the seastate must be reduced by the device. The power in a seastate is proportional to the energy, therefore according to Eq 2.9 and Eq 2.10 this involves reducing the wave height of the surrounding wave field. This is achieved through the destructive interference of a radiated wave field. For the case of a point absorber moving in heave, the radiated wave field is symmetric with an amplitude relative to the frequency dependent radiation damping coefficient. Figure 2.3 shows the implications of this symmetrical radiated wave field on the maximum power absorption possible by a point absorber moving in one degree of freedom.

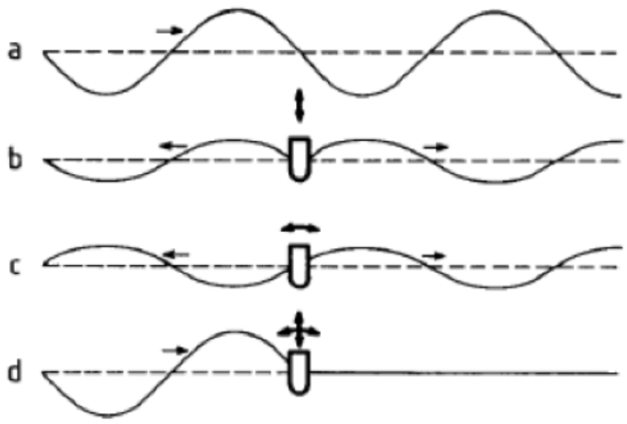

Figure 2.3: Two dimensional wave field interference patterns from an ideal point absorber.[45]

It can be seen from Figure 2.3b that a body with only heave motion can ideally only extract 50% of the available wave power due to the symmetrical radiated wave field. Extending this logic to three dimensions it has been shown that the interference patterns of a heaving point absorber causes a power antenna/focussing effect on the wave field, resulting in the theoretical power absorbtion limit being related to incident wavelength as in Eq. 2.15 [45] [46].

$$P_{lim} = P_{reg} \frac{L_w}{2\pi} \tag{2.15}$$

It can be seen from Eq. 2.15 that as the wavelength can be many times that of the device width, the available power to a heaving point absorber can be greater than that simply related to the device width.

Extending this fundamental limit of the power available to a heaving axisymmetric float within a linear array [1] finds the maximum power available ($\hat{P}_{lim}$) to be:

$$\hat{P}_{lim} = P_{reg} \frac{l \cos(\theta)}{2} \tag{2.16}$$

where l is the array spacing and θ is the angle between the linear array and the wave front. Thus, the maximum power output from the array is achieved when the wave fronts are aligned with the array (i.e $\theta = 0$) If one combines Eq. 2.15 with Eq. 2.16, the relationship between the maximum available power limit and the array spacing is highlighted.

$$l = \frac{L_w}{\pi \cos(\theta)} \tag{2.17}$$

It can be seen from Eq. 2.17 that the optimum array spacing is also a function of the incident wavelength and in situations where $l > L_w/\pi \cos(\theta)$, the devices are essentially independent and limited by Eq. 2.15.

2.4 Oscillating Water Column: Working Principles

To test the effects of interconnected mooring systems on array performance and line tensions, a suitable WEC was required. A floating oscillating water column (OWC), namely the Instituto Superior Técnico (IST) Sparbuoy, was chosen.

The floating OWC utilizes the pressure differential caused by the reciprocating motion of water within a cylinder to drive air through a turbine. Only a few designs have reached full scale prototype status with the first generation of devices being fixed to the shoreline or the near-shore seabed. The main benefits of these shore-based devices include the lack of complex mooring requirements, less expensive cable infrastructure as well as ease of maintenance. As discussed in Section 1.1, despite the nearshore wave resource being lower that that found offshore, if the location is selected carefully some of this reduction can be reclaimed from local diffraction and refraction effects [47]. This is highlighted by the Pico plant site location being in an area of shoreline gullies that have a natural energy concentrating characteristic [48].

The power take off unit (PTO) usually consists of either a self-rectifying impulse turbine, or a Wells turbine, designed by Alan A. Wells in 1976 for OWC applications [49]. Mechanical shaft rotation is generated through pressure differences over airofoiled turbine blades for the Wells turbine, and through flow deflection for the Impulse turbine [50]. The self-rectifying nature of these turbines allows unidirectional rotation of the rotor with an oscillating flow. Technological advances in turbine designs have led to the contra-rotating Wells turbine, providing higher torques, found in the LIMPET system, Islay, UK, which results in higher efficiencies[49].

The characteristic design of floating OWCs can be tailored to exploit cavity resonance of the tube and point absorbing characteristics described in Section 2.3.2 to maximize the power extraction. The OWC cavity and the float will have their own respective natural frequencies (Eq 2.18 and Eq 2.19 respectively) at which they will resonate [1].

$$f_c = \frac{1}{2\pi}\sqrt{\frac{g}{L_1 + L_1^{'}}} \tag{2.18}$$

$$f_z = \frac{1}{2\pi}\sqrt{\frac{\rho g A_{wp}}{m + m_w}} \tag{2.19}$$

where f_c is the natural frequency of the tube cavity/water column, f_z is the natural frequency of the float, L_1 and $L_1^{'}$ are the draught and effective length respectively (a term to represent the added mass of the water column), m and m_w are the mass and added mass of the float and A_{wp} is the water plane area of the float. Eq. 2.18 and Eq. 2.19 are derived from the natural frequency of an undamped spring mass damper system, where the $\rho g A_{wp}$ term is representative of the stiffness component. This approximation is only valid providing the cylinder is straight-sided.

It can be seen from Eq 2.18 and Eq 2.19 that the float natural frequency can be controlled by varying the mass and water plane area, whilst the cavity resonance can be controlled by varying the draught. This resonant frequency is usually designed to occur at the most probable or highest energy sea state at a certain location[1].

2.5 Numerical Modelling

2.5.1 Numerical Models - Single devices

Until the 1970s, WEC designs were largely based on intuition and empirical research, lacking in any numerical backing. Later in that decade, numerical methods for modelling WEC responses in the frequency and time domain were developed. With ever-increasing computational power available, the type of numerical models have evolved since these first codes. Beginning with linear boundary element method (BEM) models based on linear potential flow theory, fully non-linear BEM codes and computational fluid dynamics (CFD) models became more commonly used for wave energy converter problems. Whilst the linear methods make assumptions to improve computational time, for certain cases this is sufficient, however thresholds exist where these assumptions become too great to give useful results and one has to move towards more computationally demanding non-linear or CFD methods [51].

Once validated, these numerical models provide developers the ability to explore design alterations within the relatively inexpensive numerical domain, rather than having to continually test these changes in a physical laboratory.

Numerical modelling has played a crucial part in the development of WEC developments and improving the understanding of the device hydrodynamic interaction. For example numerical modelling was used in [52] to optimize the geometry of the Sparbuoy floating OWC device to match the resonant frequency of the device to the most probable conditions of a particular test site. The Sparbuoy was modelled as a two-body system (namely the body and the water column), coupled through a linear PTO. The parametric study optimized the geometry variables shown in Figure 2.4a, using a Constrained Optimization By Linear Approximation (COBYLA) algorithm, iteratively calling the linear potential flow theory BEM code WAMIT to optimize the device power output for a scatter matrix. Examples of the meshes can be seen in Figure 2.4b.

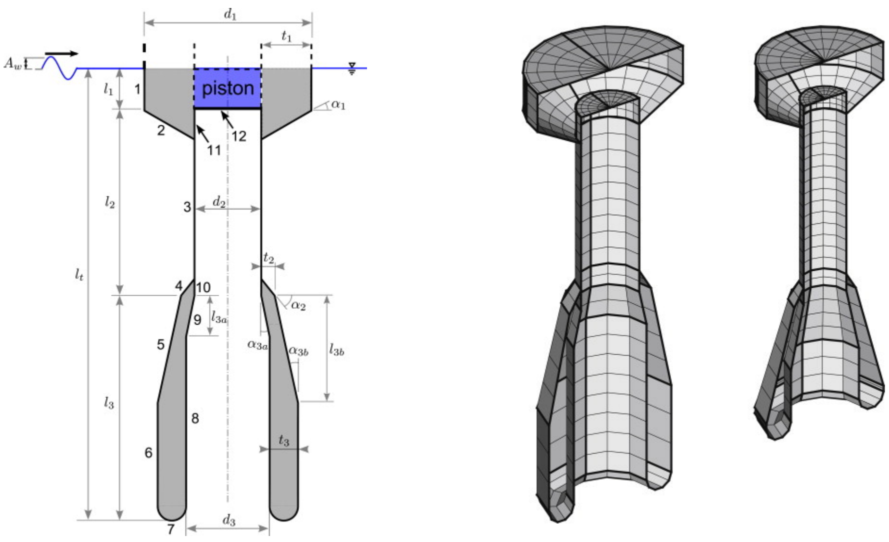

(a)

(b)

Figure 2.4: The geometric variables for the optimization (a) and example meshes of the geometries solved in WAMIT (b) [53].

Different device types have been investigated for a given deployment site as shown in [54] to indicate the most efficient system. Metrics such as the annual energy absorbed per unit mass and the annual absorbed energy per unit area of sea-space were used to indicate comparators of device costs and environmental impact.

Moored floating devices require modelling with an iterative design approach due to the mooring configurations. As described in [55], the mooring system and device need to be designed together as the mooring configuration can significantly alter the dynamic response of a WEC. Commercial codes are available to couple the hydrodynamics of a device with mooring system dynamics, such as OrcaFlex. More recently, open source codes have become available, such as MoorDyn. Full and model scale model validation including moorings have been carried out in [56] on the South West Mooring

Test Facility buoy (SWMTF). Good agreement was shown between numerical and physical models, however at full scale variations became evident due to uncertainty in the exact anchor position.

2.5.2 Numerical Model Fundamentals

The following section describes the models used and the underlying equations that are solved. See Figure 2.5 for a diagrammatic input/output flow chart as described below.

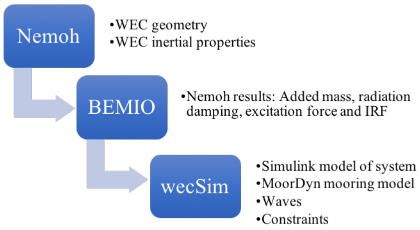

Figure 2.5: The process flow for the numerical model with the associated inputs and outputs.

2.5.3 Nemoh

Nemoh is an open source frequency domain boundary element method (BEM) code used to calculate the hydrodynamic coefficients for floating bodies developed at Ecole Centrale de Nantes. The model is potential flow theory based and fully linear, therefore assuming [57]:

- Inviscid fluid.
- Incompressible and irrotational flow.
- The velocity is expressed in terms of a velocity potential.

- Small steepness and small motion about a mean position.
- Linearized free surface.

The input file required is a mesh file and a simulation parameter file. For this study the outputs required from Nemoh are the first order frequency dependant hydrodynamic coefficients, namely, the added masses, radiation damping, excitation force and the impulse response function.

To improve the run time of the Nemoh simulations, an Amazon EC2 Linux virtual machine was spun up with an Intel Xeon 3.3 GHz processor. As Nemoh was written without parallel processing in mind, multi-threading multiple cores is not possible. Therefore, the highest clock speed processor available was used. Latest versions of the Linux compiled executables cloned from a GIT repository.

To prepare the Nemoh outputs for time domain simulation the BEMIO toolbox was used to package the results in an .hdf5 file for use with wecSim.

2.5.4 MoorDyn

MoorDyn is an open source lumped mass mooring line model for simulating mooring dynamics for floating offshore structures in the time domain. The model accounts for hydrodynamic, buoyancy, damping, and line stiffness forces [58]. The C++ implementation was utilized with a MATLAB wrapper using an XCode compiler.

MoorDyn requires one input file to describe the mooring system and simulation parameters. The line materials and attachment mass, volumes and initial positions are described in the input file. Once the executable is called, the static equilibrium position of the lines and attachments is solved before the dynamics simulation is run.

2.5.5 wecSim

wecSim is an open source time domain simulation package used to model the interaction between incident waves and device motions using the radiation and diffraction method [59]. The incident wave field and therefore the forces acting on the device, is considered from the sum of the incident, radiated and diffracted wave field and thus the equation of motion in the time domain is described in Eq. 2.20 [60].

$$m\ddot{X} = F_e(t) + F_{rad}(t) + F_{PTO}(t) + F_B(t) + F_m(t) + F_v(t) \tag{2.20}$$

where F_e is the excitation forces, F_{rad} is the radiation forces, F_{PTO} is the PTO force, F_B is the buoyant restoring forces, F_m is the mooring forces and F_v is the damping force vector.

F_e,F_{rad} and F_B are all calculated in the frequency domain by Nemoh. For this study the PTO forces will be considered as an additional linear term as shown in Eq. 2.20.

To include the effect of past radiation forces and fluid memory in the simulation the radiation term is calculated using the Cummins method, as shown in Eq 2.21 [60].

$$F_{rad}(t) = -A_{\infty}\ddot{X} - \int_0^t K_r(t-\tau)\dot{X}d\tau \tag{2.21}$$

where K_r is the radiation impulse response function as calculated by Nemoh and A_∞ in the added mass at infinite frequency. The convolution integral in Eq 2.21 is solved using a state space approximation.

The inputs to wecSIM are the frequency domain hydrodynamic coefficients in a packaged .hdf5 file, a simulink model describing the mechanical connections of the device to the seabed, the MoorDyn input file and a simulation input file. The simulation input file describes the simulation parameters such as the time step, wave, body and solver characteristics.

The heave response amplitude operator (RAO) is then computed using the linear equations of motion:

$$RAO_{33} = \frac{Fe_{33}}{-(m + m_{33} + M_{PTO})\omega^2 + i\omega(B_{33} + B_{PTO}) + C_{33}} \tag{2.22}$$

The variables in blue were calculated using the BEM code. The specific mesh characteristics and calibration parameters of the RAO are discussed further in the following chapter.

3

Design, Build and Validation of a Sparbuoy Device

The working principles of oscillating water column type devices is first covered, before the methodology used to design a 1:40 scale model of the Sparbuoy device is described. The methodology for verifying the models is presented with the results, followed by a description of the mooring configuration designs. A detailed description of the methodology and results of the orifice plate calibration used to represent a turbine at model scale is given. The chapter concludes with the set up and calibration of the numerical model used to simulate the motion response of the Sparbuoy.

3.1 Model Design

Full-scale drawings for an optimized device geometry and mass distribution in salt water were adopted from [61]. In order to recreate the model at 1:40 scale with the same draught, the mass was amended to accommodate the freshwater in COAST Laboratory at the University of Plymouth. Froude scaling (Table 3.1) was used to scale down the device characteristics and inertial properties to set the similarity relations between model and prototype scales. Froude scaling neglects any viscous effects acting on the body; a generally accepted assumption in most hydraulic and coastal engineering applications [62]. Due to the multiple fluids within the boundary of the device, namely water and the air within the water column, the significance of the aerodynamic and thermodynamic effects could be more substantial than for a generic WEC at full scale [47]. For the purposes of this experiment one can neglect these scaling issues, as a comparison of the effects due to the mooring interconnections is being made, not the model effects.

Figure 3.1 shows the device and naming conventions throughout this thesis and for dimensioned part drawings please see Appendix 9. The device

Table 3.1: Table showing the Froude similitude factors for commonly used parameters of physical hydrodynamics testing, where λ is the scaling factor.

Length	Area	Volume	Time	Frequency	Velocity
λ	λ^2	λ^3	$\lambda^{0.5}$	$\lambda^{-0.5}$	$\lambda^{0.5}$
Acceleration	Mass	Force	Energy	Power	
λ^0	λ^3	λ^3	λ^4	$\lambda^{3.5}$	

at full scale would be fabricated from 15 mm steel plate. At 1:40 scale this would result in a wall thickness of 0.375 mm, an unachievably thin section, considering the ballast of circa 12 kg hanging from one end. Various materials were investigated for use in the build, including fabricated aluminium and various plastics. It was found that with a fabricated aluminium shell, the sheet thickness had to be at least 2 mm to be welded with accuracy and to prevent warping in the OWC tube. This made it impossible to locate the centre of gravity in the correct position. Thus, it was agreed that the thinnest 'off the shelf' acrylic tube section (3 mm) would suffice, with the outer diameter being the geometrically scaled parameter. The extra thickness in the OWC tube wall provided a higher relative displaced volume than the true geometric scaled model causing a larger buoyant force ,thus altering the natural frequency of model (Eq. 2.19).

The resultant additional buoyancy force due to the OWC tube wall thickness would reduce the draught of the device in still water, altering the hydrodynamic properties and therefore the performance characteristics. To compensate for the larger wall thickness and the freshwater used in the testing basin, the ratio of the volumes (V) are subtracted from the fluid density ratio. This ensures the correct draught at full model scale in freshwater (See Eq. 3.1, where subscript m and p are model and prototype scale respectively and $\left(\frac{L_p}{L_m}\right)^3$ is the Froude scale factor for mass.

$$\left(\frac{\rho_m}{\rho_p}\frac{V_{thick}}{V_{thin}}\right) M_{\rho 1025} \left(\frac{L_p}{L_m}\right)^{-3} = M_{\rho 1000} \tag{3.1}$$

This was checked by measuring the unmoored draught shown in Figure 3.2

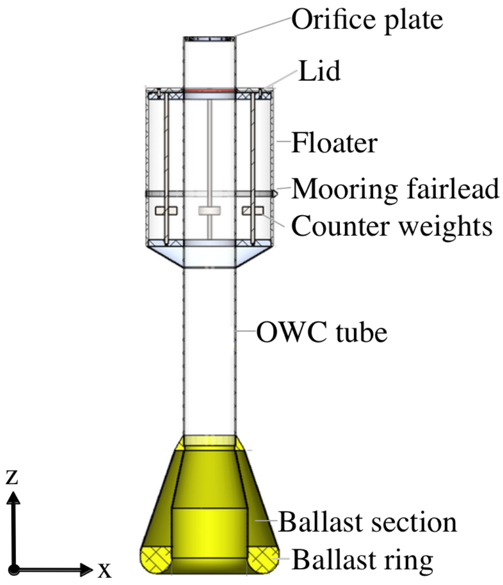

Figure 3.1: A labelled CAD model of the Sparbuoy device.

to be within 2% of the nominal still water level (SWL) shown on the scaled drawings in Appendix 9.

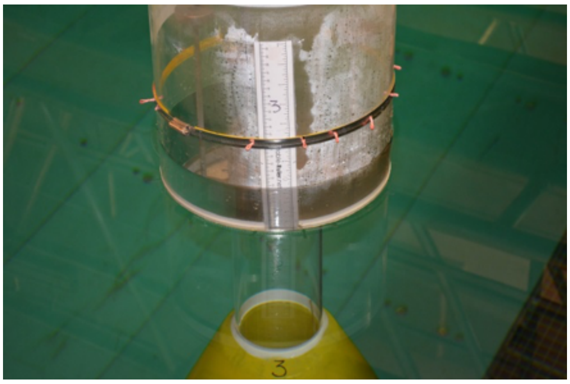

Figure 3.2: The measured unmoored draught of the Sparbuoy of 892 mm.

3.2 Model Build

An initial model (designated TM0) was fabricated in the University of Plymouth's workshop in order to determine suitable manufacturing processes to build the full array. Off the shelf, pre-cut, standard diameter acrylic tubing was used for the floater and OWC tube. The remaining acrylic components, namely the lid, orifice plate and the PTO ring (See Appendix 9) were laser cut oversized before being finished on a lathe.

The ballast ring was milled on a 3-axis CNC mill from a 330×330×70 mm solid aluminium block. The top side was machined first in order to leave a flat face from which the work could be held when machining the radius (Figure 3.3).

The counter weights and sheet aluminium parts for the ballast section were waterjet cut and deburred by hand. The ballast section was welded to form a water tight compartment that was bonded to the OWC tube using marine grade SikaFlex (291i). The lid and floater sections were bolted together with M5 stainless steel bolts and sealed with a custom fit silicon O-ring. The

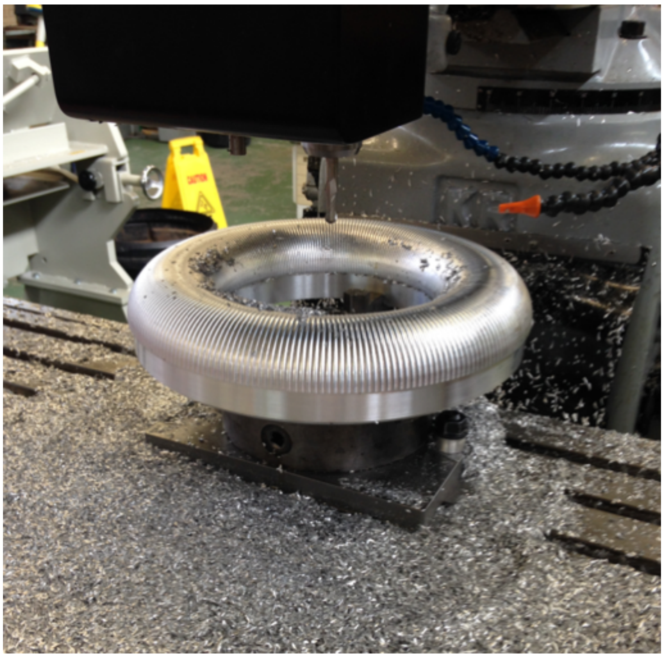

Figure 3.3: Milling of the ballast ring on a 3-axis machine for the initial TM0 model.

orifice plate was bolted to an internal acrylic ring bonded within the OWC cylinder with Tensol 12. A large jubilee clip was fixed around the floater section, with ultra high molecular weight polyethylene rope (Dyneema) loops providing mooring fairlead connection points (Figure 3.4c). Finally all potential leak paths were sealed with silicon grease.

The devices to be tested within the array configurations were named TMX, where X is a place holder for the device numeber (ie. 1-5). Considering machining capabilities, it was agreed that the most time efficient method was to turn the bottom section on a CNC lathe and laser cut the sheet aluminium for the cone sections. All other build methods remained the same between $TM0$ and the TMX devices.

Full engineering drawings of each component can be found in Appendix 9.

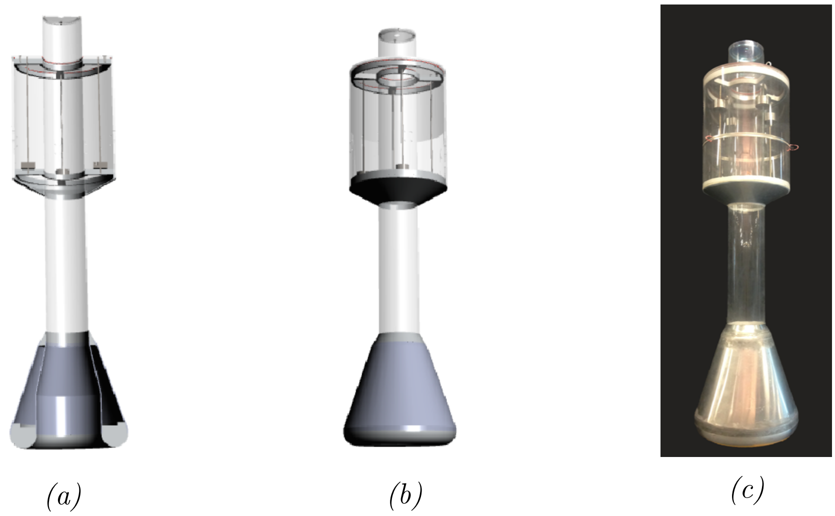
(a) (b) (c)

Figure 3.4: A section (a) and full view (b) of the Sparbuoy CAD model and a photograph of the assembled TM0 model built at the University of Plymouth (c).

3.3 Model Verification

3.3.1 Centre of Gravity

Key to matching the inertial and stability characteristics of the scaled model to the full-scale device, is the location of the centre of gravity (CoG). It is assumed for the following calculations that the Sparbuoy is axisymmetric in the xy plane, and has non-symmetric properties only along the z axis (See Figure 3.1). Figure 3.5 shows the set up used to determine the location of the centre of gravity, with F_1 and F_2 being the line tensions measured by in line load cells, separated by distance ΔZ_R=740 mm.

The length of the support lines was adjusted to assure the device was level and the lines were square to the device for the entirety of their length. Owing to the set-up being in static equilibrium, moments about point P can be taken to locate the centre of gravity, as shown in Eq. 3.3. The counter

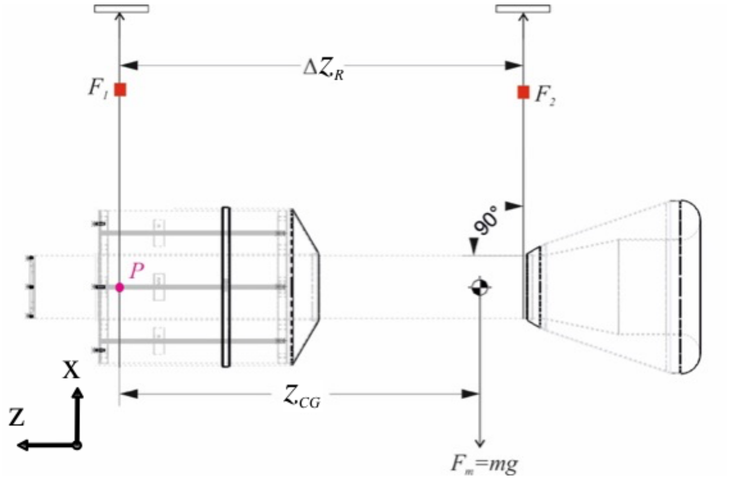

Figure 3.5: The rig used to locate the centre of gravity through considering an equilibrium of forces.

Table 3.2: Device masses and positions of the centres of mass, measured from the top of the orifice plate and unmoored draughts.

Device	**Mass [Kg]**	**Diff [%]**	**CoG [mm]**	**Diff [%]**	**Draught [mm]**
CAD	18.88	0	857.3	0	NA
TM1	18.74	1	867.7	< 1	890
TM2	18.75	1	862.8	< 1	890
TM3	18.93	0	859.1	0	890
TM4	19.02	-1	859.9	0	890
TM5	18.77	1	862.6	< 1	890

weights were mounted on threaded bar and the positions were adjusted to fine tune the centre of gravity of the devices.

$$\sum M = 0 \tag{3.2}$$

$$Z_{CG} = \frac{\Delta X_R F_2}{F_m} \tag{3.3}$$

In accordance with Froude scaling laws the nominal position of the centre of gravity was matched to the full scale device with a scale factor of λ (See Table 3.1). Allowable tolerances on the position of the model centre of gravity were set at ±5% [63].

The mass of the devices was measured during the CoG tests from the summation of the load in F_1 and F_2, dividing throughout by the acceleration due to gravity to convert to units of mass (kg). Importantly, it can be seen from Table 3.2 that the measured device masses were within 1.5% of each other in the worst case. This is further validated by the measuring the device draughts. These were measured with a flexible rule affixed to the device while the device sat unmoored in the water, as shown in Figure 3.2. A tolerance on this measurement was deemed to be ±2 mm due to water movement and surface tension effects. The positions of the centre of gravity are shown in Table 3.2 to be within 1% of one another, which was considered within the afore mentioned tolerance.

All tests were randomly repeated five times to minimize method errors.

3.3.2 Inertial Properties

To verify the inertial properties of the device, the methodology set out in [57] was used. The units of the mass moments of inertia are kg m^2, therefore the Froude scaling factor used is $\lambda^3\lambda^2 = \lambda^5$. The device was suspended like a pendulum and an initial displacement in the plane of interest was induced through pulling the device using a pulley system aligned with the reference plane (See Figure 3.6).

The device was released, allowing oscillatory motion about the pivot point. The spatial position of the device was tracked using Qualisys and

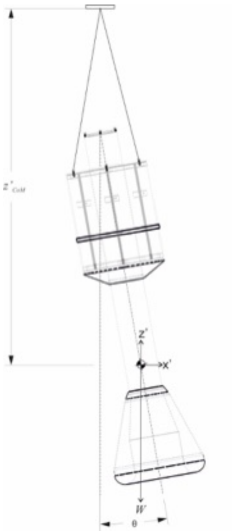

Figure 3.6: Inertial property rig set up with static global reference plane.

the time history was recorded to a local computer. The natural period (T_N) of the swing was then determined as the average period between oscillations from the time histories.

The natural frequencies of swing oscillation were measured to be within 2% of each other, as shown in Table 3.3. Devices were randomly selected and swing tests were repeated, so to remove any systematic errors, with all natural frequency measurements being within less than 1% of one another.

Assuming small angle approximations, Eq. 3.4 was then used to calculate the radius of gyration about the pivot point and subsequently, the mass moment of inertia of the system [64]. W_n is the weight of the device, T_N is the average oscillation period and Z_{CG} is the distance from the pivot to the centre of gravity. Due to the dynamics of rotation being affected by the added inertia of the device, a tolerance of ±20% was deemed appropriate.

Table 3.3: The period of oscillation T_N measured from swing tests and the calculated I_{yy}/I_{xx} moment of inertia for all devices with the associated percentage difference from the specification.

Device	T_N	I_{yy}	**Diff [%]**
CAD	NA	3.83	0
TM1	2.962	3.40	-10
TM2	2.960	3.40	-10
TM3	2.965	3.92	2
TM4	2.965	3.69	-4
TM5	2.965	3.69	-4

$$I_{yy} = \left(\frac{T_N}{2\pi}\right)^2 W_n Z_{CG} - \frac{W_n}{g} Z_{CG}^2 \tag{3.4}$$

It can be seen from Table 3.3 that the measured I_{yy}/I_{xx} moment of inertia is within 11% of the specification and a maximum difference of 12% between the five devices. As the experiments compared different mooring configurations, it was important that devices were similar to one another in order to highlight only the mooring effects, rather than due to model differences. For the purposes of comparing interconnected mooring systems, the devices were deemed adequately similar.

3.4 PTO Validation

An orifice plate was used to apply damping to the water column similar to that expected from a Wells turbine. A 19 mm orifice with a square edge profile was used, as shown in Appendix 9. This design was adopted and scaled down from larger scale experiments [18].

In order to determine the power absorbed by the device, the pressure in the OWC and flow rate across the orifice were required. Ideally both parameters would be measured in all devices. However, when testing arrays of devices that can move extensively, the high number of sensors and wiring becomes challenging. An alternative method for measuring the power absorbed is to calibrate the orifice plate, so that only the pressure measurements are required. It is published [65] where an orifice plate restricts flow through a cylindrical pipe, the pressure has a quadratic relationship with the flow rate. If this quadratic coefficient is known, it is possible to infer a flow rate from a known pressure, or vice versa.

The methodology adopted for calibration of the orifice plates follows [66] and [67]. Although these papers have the same testing set up, [66] assumes incompressible flow and symmetric conditions for inhalation and exhalation (i.e the discharge coefficients are the same for both directions of flow). [67] includes the air compressibility and the asymmetry in the flow conditions between inhalation and exhalation. Both models were investigated to select the most appropriate method for the final analysis, with results being shown in the following section.

3.4.1 Calibration Rig Build and Methodology

A piston assembly was fabricated in the University's mechanical workshop. The cylinder was a bored steel cylinder with an identical internal diameter to that of the 1:40 OWC chamber. The piston head was turned from plate aluminium and rubber piston rings were used to create an air tight seal. The head was coupled to a linear actuator and the assembly was mounted and squared on a frame (Figure 3.7). The orifice to be calibrated was bolted into place at the end of the cylinder and a pressure transducer was fitted to measure the cylinder pressure at a sampling rate of 128 Hz. The position of the piston face was measured with a laser sensor, projected onto the outer face of the piston head and bolted into place next to the actuator. To determine the calibration coefficients for each orifice plate, a number of varying piston stroke amplitudes and frequencies were tested.

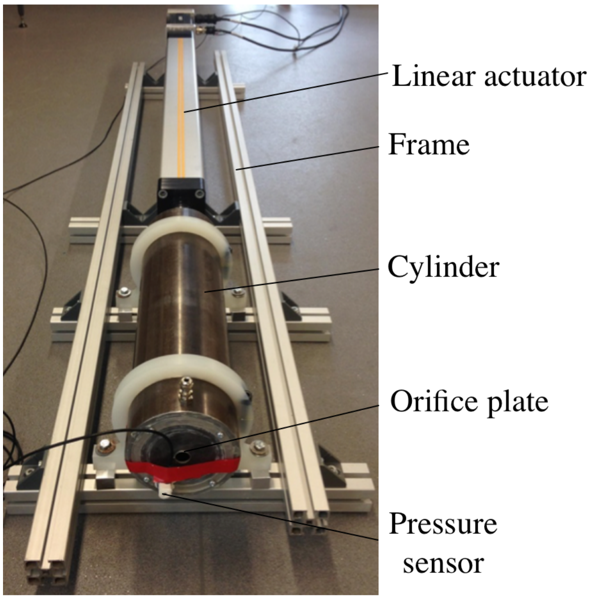

Figure 3.7: The piston rig used to calibrate the discharge coefficients for each orifice plate.

The instantaneous volume of air within the cylinder was calculated from the position of the piston head over time. The differential of this value with respect to time was then considered as the volumetric flow rate Q. For the incompressible case, the discharge coefficient was then calculated from Eq. 3.5.

$$Q_I = AC_D\sqrt{\frac{2\Delta p}{\rho_a}} \tag{3.5}$$

where A is the cross-sectional area of the orifice, Δp is the pressure difference between the chamber and the atmosphere (assumed to be 101.3 kPa), ρ_a is the density of air and Q_I is the predicted flow rate through the orifice, assuming incompressible air in the cylinder.

It can be seen from Eq.3.5 that a linear relationship exists between $Q_I^2/2$ and Δp. Let c represent this relationship such that $\frac{Q_I^2}{2} = c\Delta p$. From this the discharge coefficient, C_D, can be shown to be $C_D = \frac{\sqrt{c\rho_a}}{A}$.

As in [67], the compressibility of the air within the cylinder can be included in the analysis by assuming the air to be isentropic and the cylinder pressure to be much smaller than atmospheric pressure. This leads to exhalation and inhalation volumetric flow rate expressions shown in Eq. 3.6 and 3.7 respectively.

$$Q_c = -\frac{dV}{dt} - \frac{V}{\gamma p_0 + p}\frac{dp}{dt} \tag{3.6}$$

$$Q_c = -\left(1 + \frac{p}{\gamma p_0}\right)\frac{dV}{dt} - \frac{V}{\gamma p_0}\frac{dp}{dt} \tag{3.7}$$

where p is the cylinder pressure, p_0 is atmospheric pressure, V is the cylinder volume, γ is the specific heat ratio of air (taken to be 1.4) and Q_c is the predicted flow rate through the orifice including the effects of air compressibility. For the compressible model, the PTO was calibrated with the coefficients from a second order polynomial fit $k1$ and $k2$ from the measured pressures and flow rates. For exhalation ($p \geq 0$):

$$p = k_1 Q_c + k_2 Q_c^2 \tag{3.8}$$

Thus, the flow rate is solved as:

$$Q_c = \frac{-k_1 + \sqrt{k_1^2 + 4k_2 p}}{2k_2} \tag{3.9}$$

Similarly, for inhalation ($p < 0$) the pressure is related to the flow rate by:

$$p = k_1 Q_c - k_2 Q_c^2 \tag{3.10}$$

Solving for the flow rate:

$$Q_c = \frac{k_1 - \sqrt{k_1^2 - 4k_2 p}}{2k_2} \tag{3.11}$$

Substituting Eq 3.9 and 3.11 into Eq 3.6 and 3.7 respectively yields two differential equations (Eq.3.12 and 3.13) that are solved for the instantaneous chamber volumes for any measured pressures. The solution is then differentiated with respect to time to yield the volumetric flow rate.

$$\frac{dV}{dt} + \frac{V}{\gamma p_0 + p}\frac{dp}{dt} + \frac{-k_1 + \sqrt{k_1^2 + 4k_2 p}}{2k_2} = 0 \tag{3.12}$$

$$\left(1 + \frac{p}{\gamma p_0}\right)\frac{dV}{dt} + \frac{V}{\gamma p_0}\frac{dp}{dt} + \frac{k_1 - \sqrt{k_1^2 - 4k_2 p}}{2k_2} = 0 \tag{3.13}$$

Table 3.4: Summary table of discharge coefficients calculated for varying piston frequency and amplitude for orifice plate TM3 and TM2.

Device	Amplitude [mm]	Frequency [Hz]	C_D
TM2	50	0.2	0.70
TM2	50	0.2	0.69
TM2	50	0.2	0.66
TM2	50	0.6	0.68
TM2	50	0.7	0.68
TM2	50	0.8	0.68
TM2	50	0.9	0.68
TM2	50	1.0	0.68
TM2	25	1.0	0.67
TM2	25	0.2	0.67
TM3	50	1.0	0.68
TM3	50	1.0	0.68
TM3	50	1.0	0.68

3.4.2 Calibration Results

Incompressible Model - Calibration Coefficient

To assess the sensitivity of the discharge coefficient, a number of piston stroke amplitudes and frequencies were tested as shown in Table 3.4.

Table 3.4 shows piston frequency and amplitude had little effect on the discharge coefficient above $f = 0.2$ Hz, where the discharge coefficient was still within 3% of the average 1 Hz coefficient. Repeatability of the discharge coefficient measurement appears to be reasonably good with values differing by circa 0.2% from the mean.

Upon inspection of the flow rates in Figure 3.8a, hysteresis in the measured output can be seen. This was not incorporated in the incompressible

Table 3.5: Summary table of quadratic coefficients calculated for varying frequency and amplitude for orifice plate TM3 and TM2.

Test case			Exhalation		Inhalation	
Device	Amplitude [mm]	Frequency [Hz]	k_2	k_1	k_2	k_1
TM2	50	0.2	0.70			
TM3	50	0.6	-1.93E+07	5.00E+03	2.12E+07	2.00E+03
TM3	50	0.7	-2.03E+07	3.00E+03	2.41E+07	-3.00E+03
TM3	50	0.8	-2.06E+07	3.00E+03	2.71E+07	-1.00E+04
TM3	50	0.9	-2.12E+07	1.00E+03	2.71E+07	-1.10E+04
TM3	50	1.0	-2.24E+07	-1.00E+03	2.10E+07	3.00E+03
TM2	25	1.0	-2.21E+07	0.00E+00	2.85E+07	-8.00E+03
TM2	25	1.0	-2.48E+07	-2.00E+03	2.65E+07	-7.00E+03
TM3	25	1.0	-2.21E+07	0.00E+00	2.85E+07	-8.00E+03

analytical model as shown by the deviation of the measured flow rate from the red line. This hysteresis is due to air compressibility within the chamber.

Compressible Model - Calibration Coefficient

To assess the effect of piston stroke amplitude and frequency on the compressible model, the damping coefficients k_1 and k_2 are compared for each test performed, as shown in Table 3.5. It can be seen that the frequency and amplitude of the piston stroke had a greater effect on the damping coefficients of the compressible model than the variation noticed for the incompressible model. This suggests that the compressible model is more sensitive to conditions within the chamber.

Flow Rate Model Comparisons

To compare the performance of the compressible and incompressible models, the flow rates for the piston rig tests were predicted from measured pressures, with the results being shown in Figure 3.8. It can be seen from Figure 3.8a that the incompressible model captures the hysteresis loop, particularly well for the exhalation phase of the piston stroke. For the inhalation phase, the compressible model appears to over predict the losses due to the compressibility of the air, indicated by the larger enclosed area of the hysteresis loop. As expected, the incompressible model neglects the hysteresis losses and predicts a midpoint flow rate.

Pressures during OWC tank testing were much lower than that experienced in the piston calibration tests described in Figure 3.8a. It can be seen from Figure 3.8b, the incompressible model does not perform so well at predicting the measured flow rates of a lower pressure system. It was also shown in Tables 3.4 and 3.5 that the discharge coefficient associated with the incompressible model is much more stable with regard to piston stroke and frequency, compared with the quadratic coefficients associated with the compressible model. Therefore, to reduce the computational demand in calculating the flow rates and improve the stability of the results, the simplified incompressible flow model was adopted for forthcoming analysis.

It can be seen from Figure 3.8a that although assumptions of symmetrical flow conditions for inhalation and exhalation have been accepted, this is not strictly true. However, as this thesis is a comparative study between mooring systems, the relative performance will not be affected.

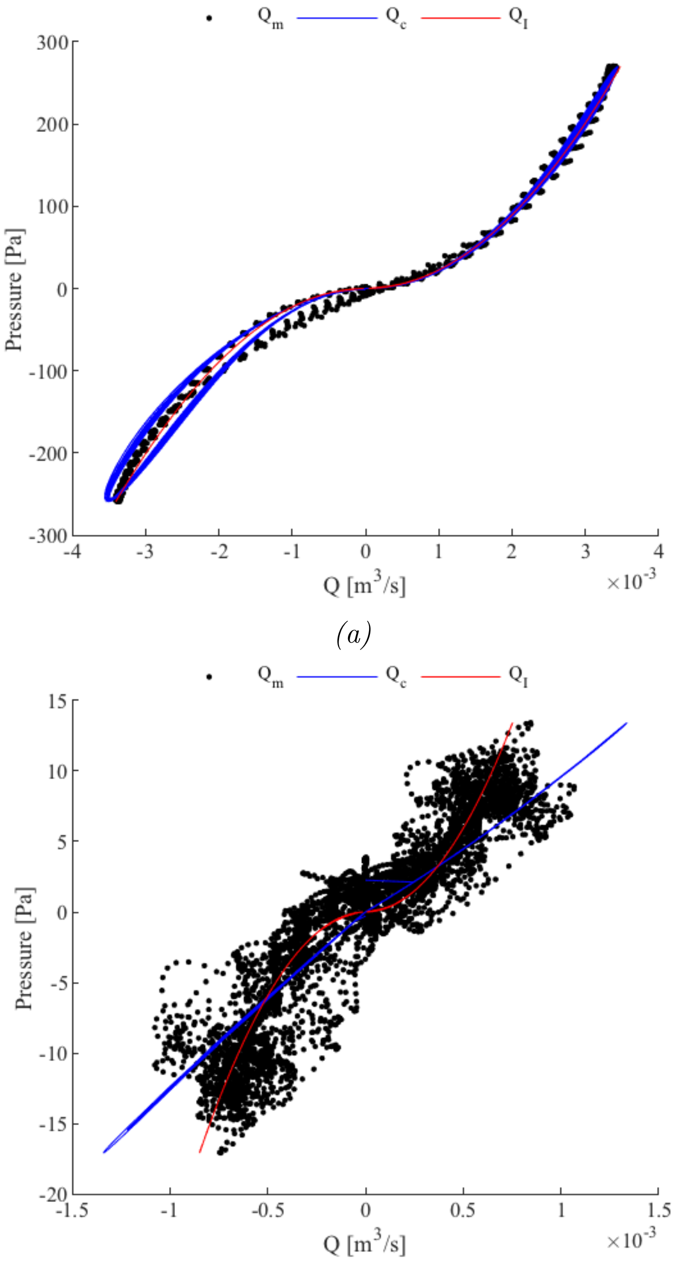

(a)

(b)

Figure 3.8: Pressure vs flow rate plots for calibration tests for $f = 1.0$ Hz (a) and $f = 0.2$ Hz (b) with measured data shown with black dots (Q_m), the incompressible model (Q_I) in red and the compressible model (Q_c) in blue.

3.5 Mooring Design - Interconnected Array

The optimized mooring line configuration for a single device is summarized in Table 3.6 under configuration A. The interconnected array moorings were designed to provide similar stiffness in surge to that of the individually moored case. The line lengths, clump and float masses were calculated using a similar optimization code to that described in Section 2.2. Table 3.6 describes the seabed mooring line properties used for the arrays and Table 3.7 shows the interlinking mooring line properties, where subscript s and d refer to the square and diagonal interconnecting lines. From this point forward, horizontal (aligned with the basin x axis) and vertical (aligned with the basin y axis) interconnecting lines will collectively be referred to as square interconnections. Diagonal interconnecting lines (45 degrees to the basin x and y axis) will be collectively referred to as diagonal lines and mooring connections to the seabed will be refereed to as seabed lines.

Table 3.6: Seabed mooring line components for the array configurations, where positions are relative to the fairlead.

Configuration	**A**	**B**	**C**	**D**
Chain diameter [mm]	4	6	6	6
Chain [m]	1.155	1.930	2.679	3.399
L_{ad} **[m]**	5.012	4.627	4.308	3.589
Clump mass [kg]	1.807	0.310	0.796	0.533
Clump mass density [kg/m^3]	5600	5600	5600	5600
Clump position from fairlead [m]	1.289	2.379	1.811	2.127
Float mass [kg]	0.001	0.005	0.007	0.009
Float density [kg/m^3]	150	150	150	150
Float position from fairlead [m]	1.74 1.78 1.82 1.85 1.89 1.93	2.95 3.00 3.05 3.10 3.15 3.20	2.35 2.40 2.45 2.50 2.55 2.60	2.43 2.48 2.53 2.58 2.63 2.68

Table 3.7: Mooring line components for the interconnecting lines of the interconnected array configurations, where positions are relative to the fairlead and subscripts s and d refer to square and diagonal interconnections respectively.

Configuration	$L_s[m]$	$L_d[m]$	$M_s[kg]$	$M_d[kg]$
B	3.789	2.628	0.163	0.389
C	3.791	2.633	0.169	0.384
D	NA	2.668	NA	0.797

3.6 Numerical Model Set up

In order to investigate further the results found in the physical tests a numerical model of the system was created. Numerical modelling is an important part of WEC design, allowing for inexpensive testing of system parameters without the need to use a physical laboratory. For this case, numerical modelling of the OWC system will allow for an extension of the data set measured in the physical tests, by modelling the device in an open ocean scenario. This gives an intuitive sense as to the implications regarding the differences to be expected in an offshore deployment compared to measurements made in the laboratory.

There are commercial codes available to model floating WECs, however, for this research, open source codes have been used. For many institutions and developers working on advancing towards commercial scale wave energy conversion, financial constraints often slow progress. Meshmagick and Bemio are command line utilities used to organize the results from a frequency domain model such as Nemoh, to that required for time domain modelling in wecSim and MoorDyn. With Meshmagick, Nemoh, Bemio and wecSim being available under an Apache V.2, and MoorDyn under a GNU public V.3 license, the numerical model has been made at no cost to the user. With support and a growing user community these codes will accelerate development in the wave energy sector.

A mesh of the full scale Sparbuoy was create using CAD software and converted to a Nemoh mesh format using Meshmagick. Meshmagick is a command line utility to convert file formats for hydrodynamic computation and was used to create the mesh input file. A mesh convergence study was carried out to minimize the number of panels from required for the computation whilst ensuring the solution converges. The final number of panels used in the model was 1760 with convergence of hydrodynamic coefficients to under 0.3%, as indicated in Figure 3.9. It is a known issue with Nemoh that modelling internal water columns and thin sections can be problematic, resulting in inaccurate hydrodynamic coefficients [57]. Figure 3.10 shows the mesh used to represent the Sparbuoy. Previous work on the numerical modelling of OWC type devices in Nemoh has shown that modelling the device with no water column is the best way to describe the system [57]. The extra mass of the internal water column is subtracted in post processing. In order to reduce computational requirements, symmetry about the xOz plane was assumed.

3.6.1 Numerical model calibration

Initially the PTO mass M_{PTO} and damping B_{PTO} in Eq. 2.22 was assumed to be zero. The magnitude of the linear damping coefficient was then iteratively increased, to represent the PTO damping on the system, until the frequency of the peak heave RAO matched the experimental unmoored heave decay test results. This methodology corresponds to that undertaken in [68].

It can be seen from 3.11 that the PTO exerts considerable damping on the device RAO, as calculated by Eq. 2.22 with approximately 17.79 Kg/s resulting in a similar natural frequency to that noticed in physical unmoored

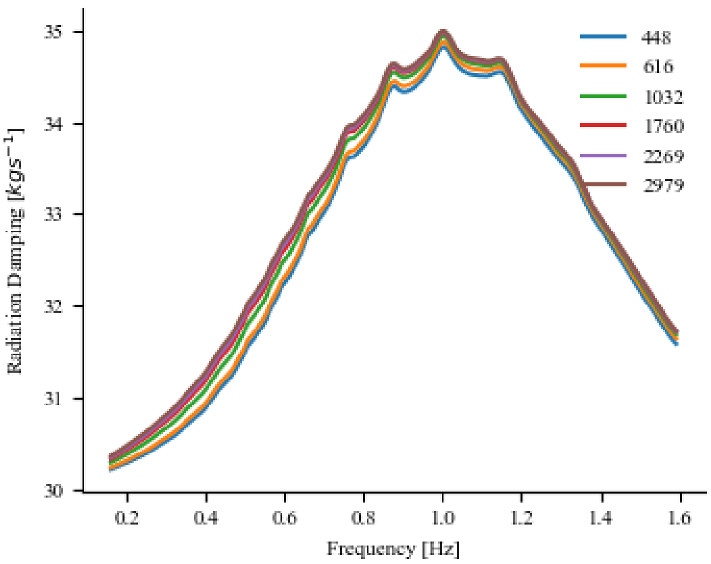

Figure 3.9: The mesh convergence carried out to minimize the panel numbers for the computation whilst ensuring that the solutions converge.

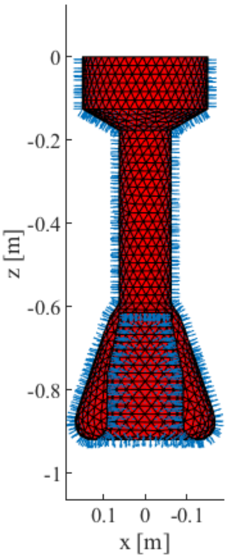

Figure 3.10: The mesh and normal vectors used to calculate the frequency domain hydrodynamic coefficients in Nemoh.

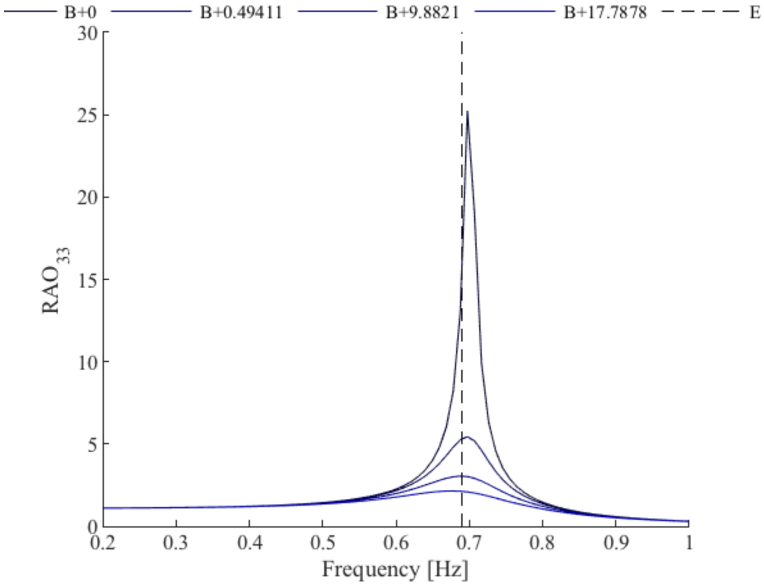

Figure 3.11: Heave motion RAO output from Nemoh with increasing linear damping coefficient and the measured unmoored device natural frequency.

decay tests. The effect of this linear damping coefficient in the time domain was then assessed by simulating a decay test and comparing the results to experimental data to assess the level to which this linear assumption can be accepted, as shown in Figure 3.12.

It can be seen from Figure 3.12 that the linear PTO damping coefficient is effective in predicting the heave displacement in the unmoored decay tests. The difference in the peaks is partially due to the discretisation of the Nemoh model that was calibrated in Figure 3.11 and partially due to experimental variation.

Table 3.8 shows the additional mooring line properties, combined with the properties summarized in Table 3.7 (Page 67) used for the MoorDyn

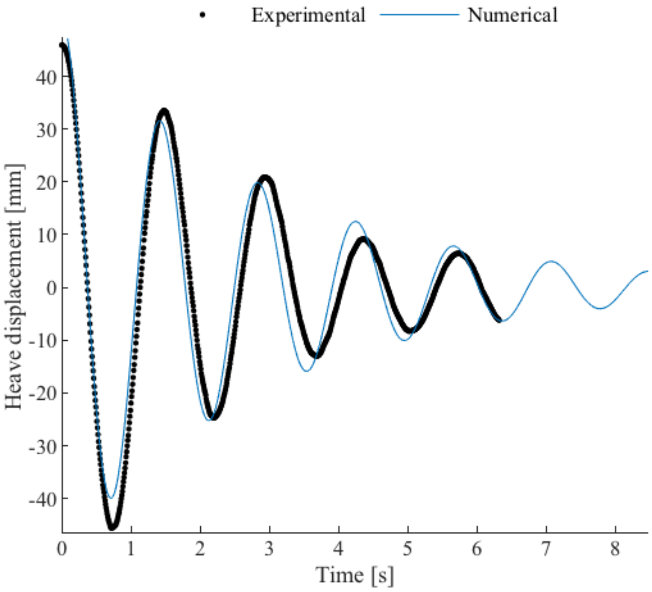

Figure 3.12: Unmoored heave decay test with a linear damping coefficient to represent the PTO damping in the numerical model.

simulation input file.

Table 3.8: The additional nominal mooring configuration parameters combined with parameters defined for configuration A in Table 3.7 used for the input file of MoorDyn. For line designation see Figure 2.2.

Property	**Value**	**Unit**
Chain mass density	0.31	Kg/m
Rope mass density	5.31	g/m
Rope diameter	2.5	mm
Rope L_{cd}	3.17	m
Rope L_{bc}	0.55	m
Rope L_{ab}	1.29	m

3.7 Mooring Line Sensitivity Analysis

It is important to quantify the effect small discrepancies in the mooring line construction have on the heave response of the device to differentiate between model and tank effects. This is because there were slight differences measured between the set ups of each experimental device and so it is important to understand the effect this could have on the results. The calibrated model from Section 3.6.1 was used for a sensitivity analysis of the mooring line construction. Three areas have been investigated as part of the sensitivity analysis:

1. The mass of the clump weight.
2. The mass of the float sections on the line.
3. The position of the clump weight on the mooring line.

All experimental mooring line lengths were measured with a tape measure and clump weight and floats were weighted using a set of scales. The furthest values from nominal were used to indicate maximum effects on the

Table 3.9: Mooring line lengths for the adjusted position of the clump weights as measured from the models used in experiments. For line designation see Figure 2.2.

Configuration	L_{ab} **[m]**	L_{bc} **[m]**
CP nominal	1.29	0.55
CP + 2.6%	1.32	0.51
CP - 2.6%	1.26	0.58

heave RAO of each variable described above. These were found to be 2.6% for the clump weight position and 0.4% for the clump weight and float mass. The regular waves simulated to validate the model (Figure 5.4) were then run again for each of the adjusted mooring conditions. The heave response amplitude of the device was simulated for each frequency tested and divided by the incident wave amplitude to obtain the RAO for each case.

The variations measured in the clump weight mass have very little effect on the device heave response, with a maximum difference of 0.4% at resonance. Similarly, for the variations measured for the float masses, the heave response appears unaltered. The measured float mass variations have a lesser effect on the device heave response than the clump weight masses.

The process was repeated altering the position of the clump weight on the top section of line (L_{ab}) as shown described in Table 3.9.

It can be seen from Figure 3.13 that the system heave response is sensitive to the position of the clump weights. By moving the clump 2.6% closer to

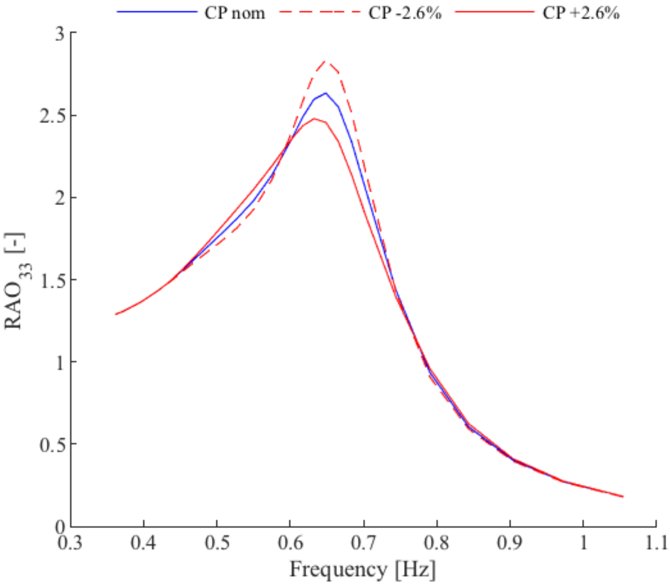

Figure 3.13: Heave RAO's for an isolated device with the position of the clump weight 2.6% further and closer to the fairlead connection point.

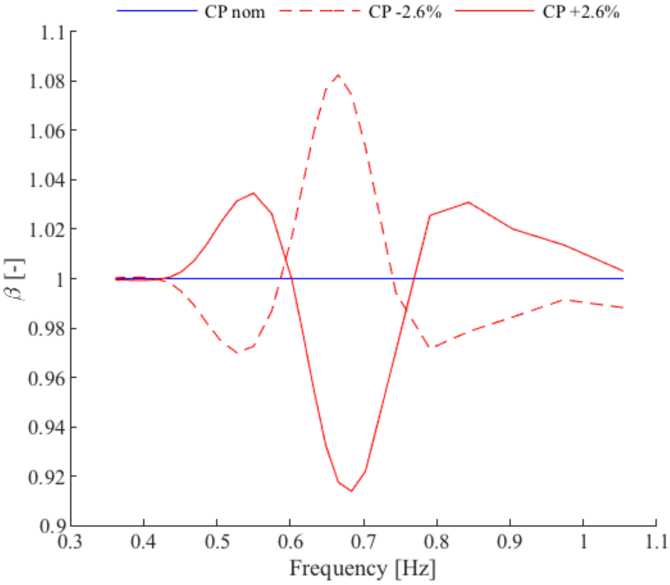

Figure 3.14: The ratio of Heave RAO's with ±2.6% variation of the clump position to the nominal RAO.

the fairlead connection point (CP -2.6%) the heave response is increased at resonance, which also appears to be at a slightly higher frequency than when the clump is positioned in the nominal location. The spectra can be compared by defining beta as the ratio of RAO responses as described in Eq. 3.14.

$$\beta = \frac{RAO_m}{RAO_{nom}} \tag{3.14}$$

From inspecting the β values in Figure 3.14, it can be seen that the maximum RAO magnitude difference due to variation in the clump weight position is circa 8% around resonance and a natural frequency shift of circa 2%.

3.8 Conclusion

To conclude this chapter, the fundamental operating principles of OWC technology were covered and a description of the build and validation procedures used to create a scaled physical and numerical model were described. The orifice calibration technique used to subsequently approximate the flow conditions of the model scale PTO was described and justification for using an incompressible flow regime was given. The next chapter will describe the experimental plan adopted to address the aims and objectives described in Sections 1.7 and 1.8.

4

Experimental Design and Data Analysis Methodology

A detailed description of the experimental plan used to address the aims and objectives set out in Section 1.8, namely the effect of device interconnectivity on the performance and survivability of a compact wave energy array is given. All analysis methodologies and data post processing is described and justified. To conclude the chapter, the level of measurement uncertainty and propagation of error has been quantified for all performance calculations that is described in the thesis.

It has been highlighted [69] that future wave energy developments will require large numbers of devices within array configurations to maximize the energy extraction potential per unit of capital and operational cost input. It has further been shown that a considerable portion of the deployment costs are associated with moorings and anchorage systems [70]. A possible solution to reduce these costs is interconnected arrays with shared anchors. The literature review indicates potential improvements in array efficiencies through these interconnections. Physical testing of such arrays, evaluating the effects on the performance and survivability, are vital to the progression of this solution.

Due to the early stages of these designs, numerical modelling alone would not alone be adequate for a concept to progress to large scale development. However, physical model testing can provide important data to calibrate and validate numerical models that can subsequently be used to investigate further configurations.

4.1 Array Architecture

The optimisation of the array spacing and layout is not the objective of this work. Therefore, providing the layout remains constant across all levels of connectivity, the spacing and layout is unimportant. However, a practical and full-scale deployable solution is required to make the study realistic. As was shown in [12] and [21], a staggered array of devices yields enhanced power absorption capacity compared to a linear array of devices, or the same number of isolated devices. As a result, three array layouts were investigated using a Pugh and Kesselring matrix (See Appendix 9) similar to that found in [71]. A 'five point dice' configuration was selected as the layout for the experimental programme due to the lower expected line tension and the ability to reduce the number of seabed anchors [28].

4.2 Experimental Set-up

4.2.1 Basin Description

Experiments were carried out in the University of Plymouth COAST laboratory Ocean Basin (Figure 4.1). The facility is a 35 × 15.5 m tank with a variable positioning floor allowing for up to 3 m of water depth. For the purposes of physical tests carried out at 1:40 scale, the water depth was set to 2.0 m, as shown in Figure 4.4. Wave generation is achieved through 24 hinged flap-type paddles controlled by an Edinburgh Designs Ltd control system. The system is capable of creating regular, irregular and directional sea states with wave heights of up to 0.9 m at 0.4 Hz. Waves are absorbed at the opposite end to the paddles via a convex beach profile and the paddles also minimize reflections through a force feedback system. The central floor allows for mooring and auxiliary connections on a 1 × 0.5 m grid of M12 threaded holes.

As with any physical basin test facility, reflections of incident waves must be considered as a potential constraint. Due to the nature of the basin shape, harmonics (of mode n) of the basin itself can be excited resulting in the formation of standing waves, as well as between devices within the array. Table 4.1 shows the harmonics of the basin width and the array spacing, where l_{xy} is the distance between outer devices and l_D is the diagonal distance between outer devices.

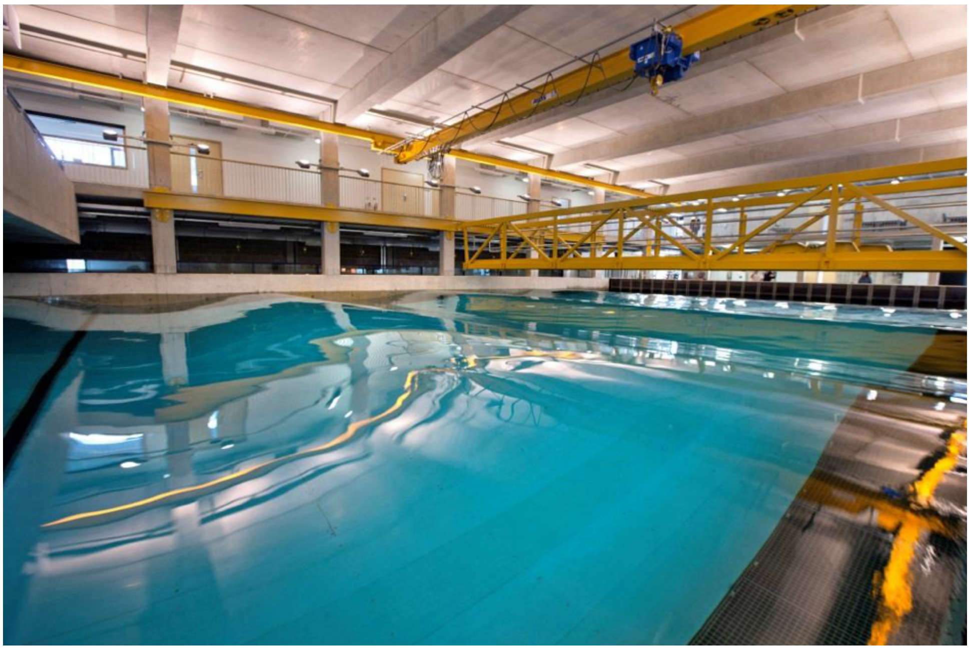

Figure 4.1: University of Plymouth COAST lab Ocean Basin.

Table 4.1: Harmonics of the basin width with the associated frequency based on linear wave theory.

n	**L [m]**	**f [Hz]**
2	15.5	0.26
3	10.4	0.36
4	7.8	0.43
5	6.2	0.49
6	5.2	0.55
7	4.4	0.59
8	3.9	0.63
9	3.4	0.67
10	3.1	0.71
11	2.8	0.74
12	2.6	0.78
13	2.4	0.81
l_xy	4.0	0.62
l_D	5.7	0.52

4.2.2 Mooring Layouts

To characterise the behaviour of the device, an isolated device was first tested in the centre of the basin. The anchor points of the isolated device were matched to that of the central device of the individually moored array case (Configuration A), as shown in Figure 4.2 (See appendix for the anchor coordinates of all configurations). The array effects on the device performance and behaviour could then be quantified by comparing the results from an array of individually moored devices to the isolated case. It was important to separate the array interactions and highlight the effects of the interconnecting lines. The level of interconnectivity and the number of seabed anchors can be seen to reduce through the configurations, representing a potential cost saving. This is however, only achievable if the mooring loads do not become excessively high resulting in the need for large expensive materials to cope with high stresses in the lines. Furthermore, the effect on performance must not be so detrimental to offset the anchorage cost savings. The position of the devices remained consistent across all configurations. The design of the seabed and interconnecting mooring lines was discussed in Chapter 3.

A naming convention to describe the arrays from this point forward will be adopted. The device names can be seen in Figure 4.2d. Subscripts I will be used to indicate an isolated device in the centre of the basin and subscripts $A - D$ will refer to the mooring configuration. Where a specific device across all configurations is being referred to, no subscript will be given. For example: $TM3_B$ is the central device with mooring configuration B and

$TM1$ refers to device $TM1$ in all mooring configurations.

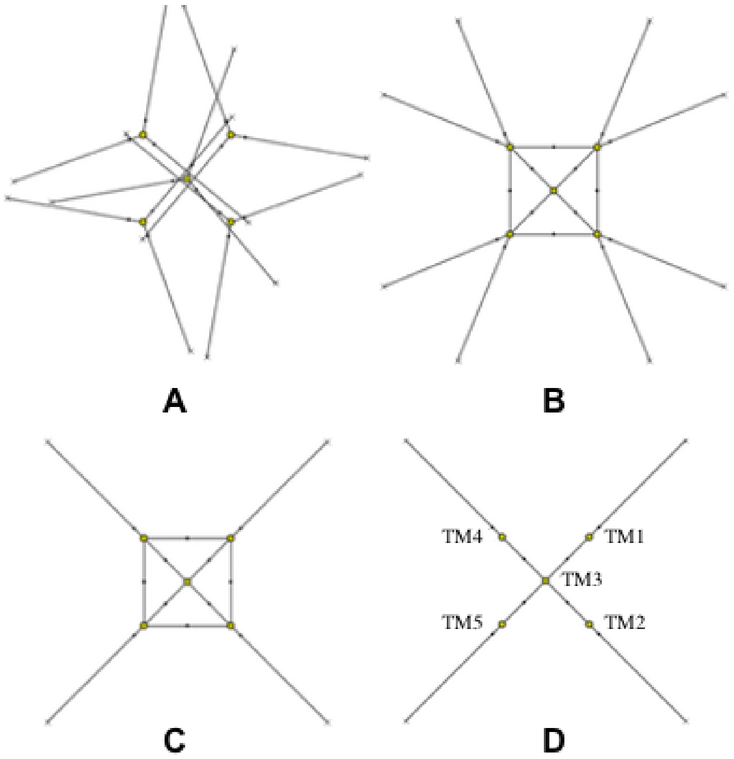

Figure 4.2: Array configurations to be tested with waves propagating from right to left.

4.3 Instrumentation

4.3.1 Wave Gauges

Resistive-type wave gauge (WG) were used to measure the surface elevations of the wave field around the basin. Gauges were calibrated to ensure linearity each morning before testing commenced. To calibrate, the gauges were positioned at three known heights and average voltage measurements were taken. A linear least squares fit model with an $R^2 > 0.99$ rendered the probe calibrated for the day.

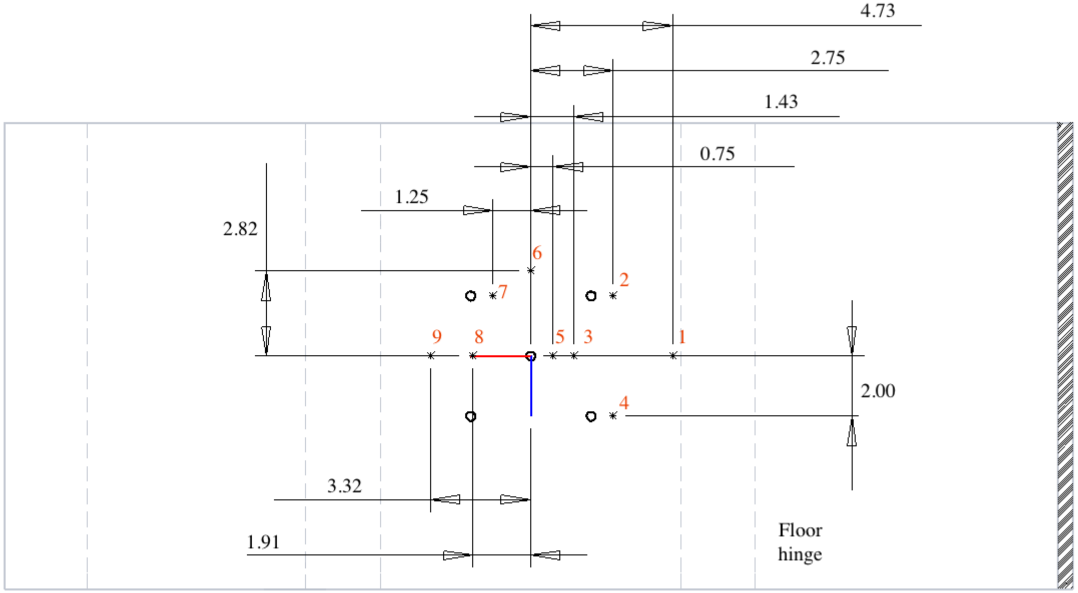

Figure 4.3: Wave gauge layout and numbering, with all measurements in metres.

4.3.2 Pressure Gauges

In this case, to calculate the device power output, the pressure and flow rate through the PTO were required. Initially, a heavy-duty industrial pressure sensor was attached to one of the devices which was manually pushed in the water to assess the maximum and minimum expected pressures in the OWC tube. This information was then used to select the Honeywell HSC analogue differential sensor with a working pressure of ±2.5 kPa and an accuracy of 0.25% of the full-scale output. The sensor was a lightweight board mounted device. A housing was 3D printed to hold the sensor in place with the input port entering the internal pressure ring (See Appendix 9). The sensors were pre-calibrated by the manufacturer and were supplied with the appropriate documentation. The analysis procedure for the power calculations are given in Section 4.5.5. The signal was acquired through a National Instruments data acquisition chassis (NIDAQ). As one chassis was used for both the line tension and pressure signals, the highest sampling frequency between the two had to be used for both sensors. In this case the load cell sampling frequency (1667 Hz) was used. A timing trigger from the wave paddles was used to initiate the data capture in order to align the beginning of all sensor outputs.

4.3.3 Motion Measurements

The Qualisys motion tracking system was used to measure the motion responses of the devices in the experiments. Reflective markers were fitted to the models on a small wand on the top of the orifice plate. In total five markers were fixed to each device in a unique layout in order to differentiate between each device. A global origin for the basin coordinate system was set up using a quadrangle in the centre of the basin. This origin defined the surge (x), sway (y) and heave (z) axis as well as the rotations about each respective axis as roll, pitch, and yaw. Each device was defined as a rigid body during calibration and the origin of the local co-ordinate system was translated to the centre of gravity of the device. All motions were then recorded relative to the global system (Figure 4.4) so that all motions (surge, sway, heave, roll, pitch and yaw) are in the same direction. Qualisys Track Manager was then used to track the markers for each wave run. The system comprised five infra-red cameras set up around the basin and a central laptop to run the acquisition software. A sampling frequency of 128 Hz was used to match that of the wave gauges and a timing trigger line from the wave paddles was used to initiate recording.

4.3.4 Load Cells

The line loads were estimated from preliminary predictions from a numerical model using OrcaFlex. Knowledge of expected line tensions from previous array tests [44] was also drawn upon to select an appropriate load cell. The LSB-210 Futek analogue submersible junior s-beam load cell was selected. This sensor has a range of ±445 N and a non-linearity of 0.2% and was deemed suitable for the proposed experimental plan. As with the pressure transducers, these load cells were pre-calibrated by the manufacturer and were provided with all the necessary certification. The signal was acquired at the minimum sampling frequency of 1667 Hz through a NIDAQ and recorded using a custom LabVIEW data acquisition program. The timing trigger from the wave paddles was also used to initiate the recording. A total of nine

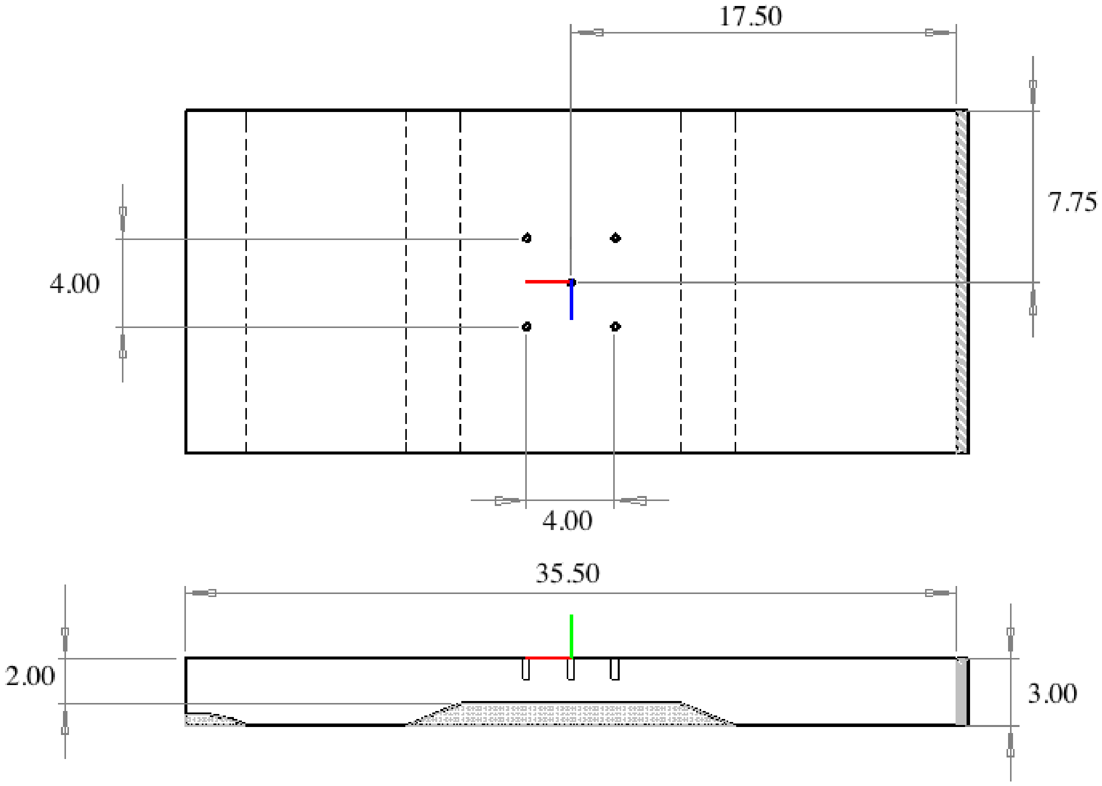

Figure 4.4: Global origin for the Qualisys system used to measure the local positions of each device where x,y,z are represented by the red, blue and green lines respectively. Waves propagate in a positive x direction i.e from right to left.

load cells were used and positions were chosen to maximize the information about each configuration (see Figure 4.5). As there were not enough load cells for every line within the array, a symmetry about *y=0* was assumed for Configuration C and D. A naming convention was adopted for example $TM3_{Ac}$, this relates to device $TM3$ in Configuration A and mooring line c. The mooring line labels were designated beginning a increasing anticlockwise from normal to the wave fronts.

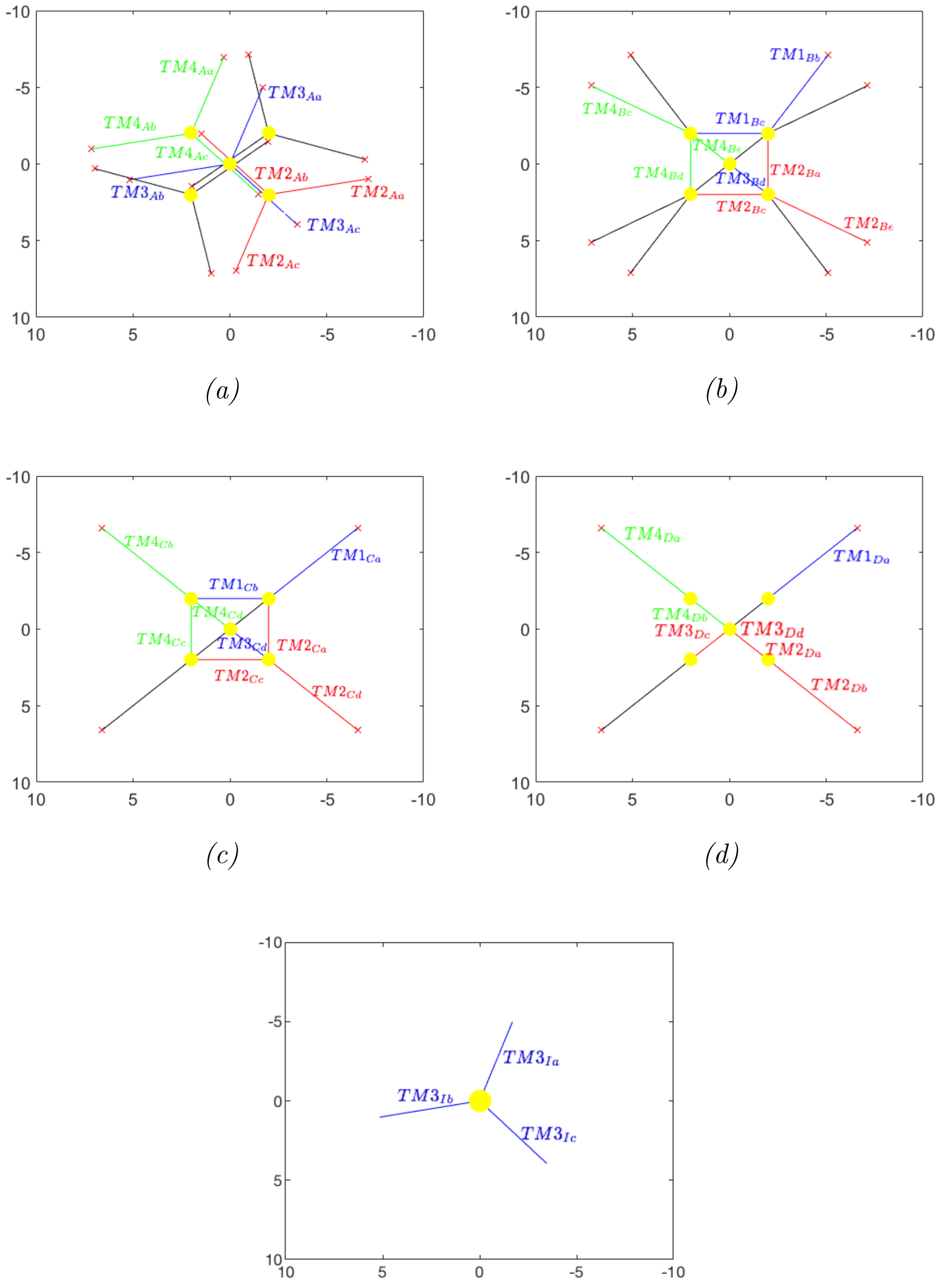

(a) *(b)*

(c) *(d)*

(e)

Figure 4.5: Load cell designation Configurations A-D (a)-(d) and an isolated device (e) and with colour-coding for visual aid. All load cells were positioned at the fairlead of their associated mooring line/device. Waves propagate in the positive x direction from right to left.

4.4 Experimental Programme

4.4.1 Waves Tested

In order to characterise the device behaviour and to quantify the effect of shared mooring systems, regular waves were tested at varying frequencies. Non-linear effects were limited by ensuring that the wave slope (H/L) was much less than Miche criterion. The full scale amplitude for regular wave tests was set at 1 m in order to reduce non-linear effects at the higher frequencies tested, whilst ensuring motions and chamber pressures were large enough to be measured with reasonable confidence. Incidentally, this amplitude is also very close to the most probable wave height at the proposed development site (Figure 4.6). The Sparbuoy has been designed for a deployment site off the coast of Leixões, Portugal. A scatter plot of the probability matrix (Figure 4.6) was provided by WavEC, with data generated from MAR3G 3^{rd} generation numerical model of a simulated ten year period, using ECMWF wind fields as the input. A sample of most sea states, summarized in Table 4.2, was selected for testing in order to confirm the findings of the regular wave characterisation and explore the effect on performance in operational conditions. The sea states tested cover circa 10% of the probability matrix. It was possible to cover a greater proportion of the operational conditions, however to achieve this, a lower significant wave height was required. This would result in OWC chamber pressures near the lower limit of the selected instrumentation and so was not considered. The two parameter Pierson-Moskowitz (PM) spectra were selected for the spectral shape as in previous studies at this location [44]. The energy period (T_e) from the probability matrix in Figure 4.6 was converted to a peak period (T_p) (required for the wave generation software) via the ratio $T_e/T_p = 0.858$ [72].

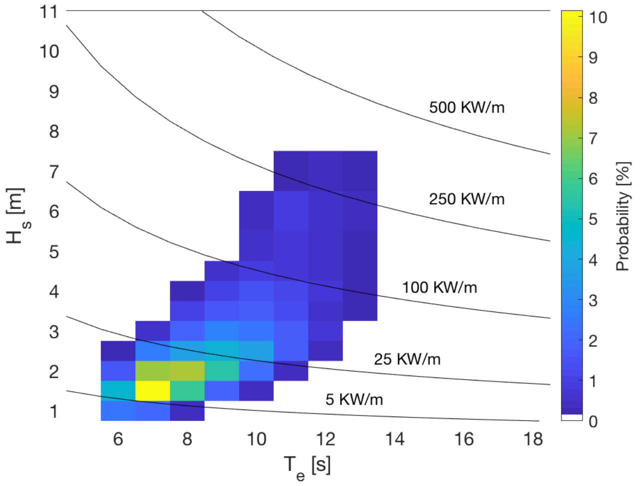

Figure 4.6: A probability matrix of sea conditions at the proposed deployment site collated from a numerical model simulation over a ten year period.

4.4.2 Wave Condition Calibration

The incident wave field within the empty tank was analysed to quantify the level to which the intended Pierson-Moskowitz spectrum could be recreated in the laboratory. Wave gauges were located in the tank on central positions of the devices in the array configuration, as well as the intended wave probe locations (See Figure 4.3). Surface elevation measurements were made with a sampling frequency of 128 Hz across 13 wave gauges. An initial spectrum of f_p =0.64 Hz (converted from T_e values as described in Section 4.4.1) and H_s =0.05625 m was run to determine the spectrum calibration coefficients, with the results shown in the top row of Figure 4.7. The gain calibration

Table 4.2: Table summarizing the amplitude and periods of the regular and irregular waves tested.

	Full Scale			Model Scale		
Reg/Irr	$A/H_s[m]$	$T_e[s]$	$T/T_p[s]$	$A/H_s[m]$	$T/T_p[s]$	$f/f_p[s]$
Reg	1	NA	6.30 -31.6	0.02500	0.1 —5	0.2 —1.0
Irr	2.25	6.50	7.59	0.05625	1.20	0.83
Irr	2.25	8.50	9.93	0.05625	1.57	0.64
Irr	2.25	10.50	12.21	0.05625	1.93	0.52
Irr	12.00	14.75	17.2	0.30000	2.72	0.37
Irr	13.00	15.79	18.4	0.32500	2.91	0.34
Irr	14.00	16.65	19.4	0.35000	3.06	0.33

coefficients was used to amplify or reduce the wave heights at each frequency component of the spectrum.

The gain correction GC was calculated as the ratio of the measured wave heights to the intended wave heights at each frequency (Eq. 4.1). The wave heights of each frequency component are proportional to the square root of the spectral energy density. The measured spectral energy density S_m was calculated using an FFT of the surfacce elevation and the intended spectrum S_i was calculated directly from the Pierson-Moskowitz spectrum.

$$GC = \frac{\sqrt{S_m}}{\sqrt{S_i}} \tag{4.1}$$

Spectral moments of the measured spectrum were then taken (Eq. 2.13), where the 0^{th} moment was used to approximate the significant wave height, as described in Chapter 2 (Pg. 27). If the significant wave height was not within 2% of the intended value, a gain correction was calculated and applied to the wave synthesizer file. The sea state was re-run, applying the new gain correction file, until the significant wave height was within 2% of the

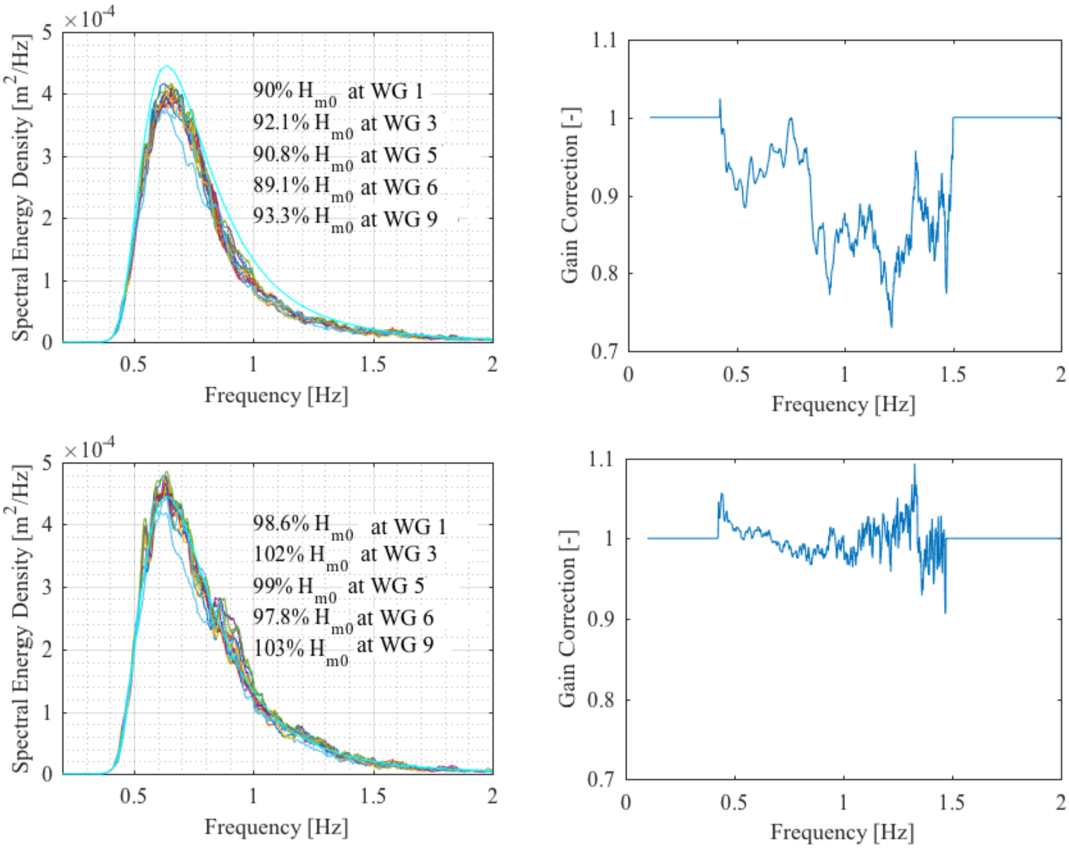

Figure 4.7: Sea state calibration spectra with associated gain corrections , where the bottom right plot satisfies the threshold for an acceptable level of accuracy for H_{m0}.

specification. As a result the magnitude of the gain correction reduced with every iteration of the process, as seen in Figure 4.7 where the second row shows the second iteration, where the reference wave gauge in the centre of the basin (wave gauge 7) ratio has improved from 91% to 99%.

4.5 Analysis Methodology

4.5.1 Data Post-Processing

Data post-processing was minimized to reduce the risk of systematic errors in results. In all cases a low pass fifth-order Butterworth filter was used to remove high frequency noise on signals. A cut-off frequency of 10 Hz was used. Where there were small sections of missing data, a linear interpolation was used to replace the loss. It has been stated wherever this was required.

The sampling frequency of the wave gauges and device motions was 128 Hz. The sampling rate of the load cells measuring the mooring line loads was 1667 Hz. Where calculations combine both incident wave or motion data and line load data, the motion or wave data is up-sampled to match the sampling frequency of the load cells.

4.5.2 Motion RAO

The motion response amplitude operator (RAO) was derived to show linearised general responses for the isolated device and for the arrays of devices. For regular incident waves, this was calculated by dividing the amplitude of motion response ($|X|$) by the amplitude of the measured incident wave ζ within a time window matching that of the incident wave calculations (Discussed in Section 4.5.4).

$$RAO_i(\omega) = \frac{|X_i(\omega)|}{\zeta} \tag{4.2}$$

where response amplitude is given by X with subscript $i = 1, 2, 3$ for translations surge, sway and heave respectively, thus resulting in a unitless RAO. For rotations, $i = 4, 5, 6$ (roll pitch and yaw respectively), with resultant units [deg/m]. The amplitude of response for each degree of freedom has been calculated using a zero-up-crossing method. The response peaks and troughs were found within the specified analysis window. The same approach was adopted for the wave surface elevation ζ, where the incident wave amplitude was measured from empty tank tests to ensure all configurations were compared to equal incident wave power.

For irregular cases the quotient of the root mean square (rms) of the displacements was used to represent the motion response operator (Eq 4.3).

$$\sigma_x^* = \frac{\sigma_x}{\sigma_w} \tag{4.3}$$

where subscripts x and w represent the degree of freedom of interest and the water surface elevation respectively.

4.5.3 Decay Tests

In order to determine the natural resonance characteristics of the Sparbuoy in each configuration, free decay tests were performed. The initial displacement was restricted to each degree of freedom by initiating the movement using a pulley system aligned with the axis of interest relative to the basin. The tests were repeated three times to quantify the repeatability and motions were measured to determine the natural frequency (f_z) and damping

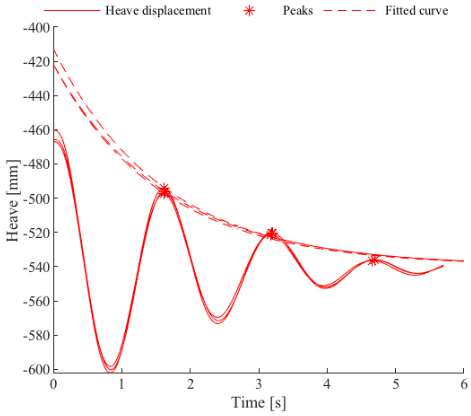

Figure 4.8: Three repeats of heave decay tests performed on $TM3_I$

.

characteristics (ξ_{tot}) of the system. The damping of the system is the total of the structural (ξ_0), radiation (ξ_w) and viscous (ξ_v) damping [21].

The damping and natural frequency calculations were made in the time domain as shown in Figure 4.8. The natural frequency was calculated as the reciprocal of the mean time between peaks. The total damping (ξ_{tot}) on the system was then determined from fitting an exponential curve of the form $y(t) = a\exp^{\xi_{tot}t}$ to the motion response, as seen in Figure 4.8. The exponent ξ_{tot} is linearly proportional to the damping coefficient of the system [21].

4.5.4 Incident Wave Power Per Metre Wave Crest

Regular (Eq 2.9) and irregular (Eq 2.10) wave power per metre wave crest was calculated in accordance with linear wave theory using Eq. 2.9 and Eq. 2.10 respectively. Windowing was used to isolate wave data between the 50th and 75th wave for regular wave cases, as shown in Figure 4.9a. This was deemed a section of stability, where reflections from the tank walls and radiation effects had stabilized in all cases. The zero-crossing analysis was performed on this window of data to estimate the incident wave power.

For irregular cases, a randomly phase shifted time series was generated from a theoretical Pierson-Moskowitz spectrum for ten minutes. The wave paddles required a ramp up and down stage to build the sea state. As shown in Figure 4.9b, these stages were neglected from the analysis.

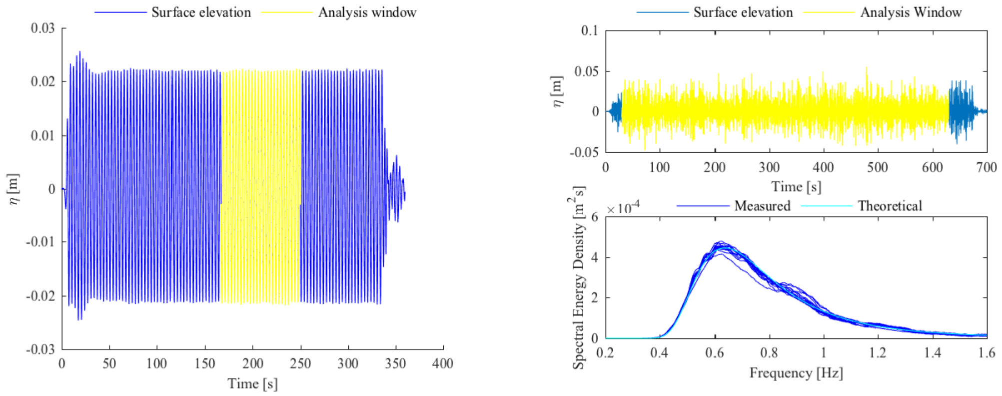

(a) *(b)*

Figure 4.9: The analysis window between the 50^{th} and 75^{th} wave for regular wave cases (a) and the ten-minute repeat time for the irregular cases, showing both the time and frequency domain surface elevations (b). The cyan line in the frequency domain is the theoretical Pierson-Moskowitz spectrum and the dark blue lines are the spectra measured at each wave gauge within the basin.

4.5.5 Device Power Output

The performance of the device was calculated from the OWC tube pressure measurements. Flow rates were calculated using the incompressible flow model (Eq 3.5) with a discharge coefficient of alternating sign depending on the sign of the pressure, as described in Section 3.4.

The generated power available to the turbine, P_{dev}, is the product of the volumetric flow rate and the pressure difference. The time averaged device power was then calculated across the time window matching the section of wave analysis and summed across the number of devices within the array. Limits of integration in Eq. 4.4, ti and tf are the time representing the beginning of the 50^{th} and the end of the 75^{th} wave respectively.

$$\overline{P}_{dev} = \frac{1}{dt}\int_{ti}^{tf} \Delta p_w Q_w dt \tag{4.4}$$

The average array power output of the array was then calculated by summing the average device power over the number of devices within the array N.

$$\overline{P}_{\text{array}} = \sum_{n=1}^{N} \overline{P}_{\text{dev},n} \tag{4.5}$$

4.5.6 Capture Width Ratio

To give comparative data between array configurations and other experimental work, the capture width ratio was calculated to represent the efficiency of the device normalised by the device characteristic width W, or in the case of an array, the sum of the characteristic device widths. The calculation remains consistent for both irregular and regular cases.

$$CWR = \frac{\overline{P}_{\text{array}}}{\overline{P}_{\text{reg/irr}} W N} \tag{4.6}$$

4.5.7 q Factor

To highlight array effects on the performance of the devices, the *q factor* was used for both isolated and array configurations. This is the ratio of the array power output to the single isolated device output, multiplied by the number of devices, as shown in Eq 4.7.

$$q_0 = \frac{\overline{P}_{\mathrm{array}}}{\overline{P}_{\mathrm{iso}} N} \tag{4.7}$$

This ratio was used at a device level, replacing $\overline{P}_{\mathrm{array}}$ with the power output from each device within the array, and dividing by a singular isolated device (i.e $N = 1$), as well as at an array level, by summing the device power outputs from the array. To isolate mooring configuration effects, the array effects were neglected by using Configuration A as the denominator as in Eq. 4.8. Again, this characteristic was calculated at both array and device level.

$$q_A = \frac{\overline{P}_{\mathrm{array}}}{\overline{P}_{\mathrm{A}} N} \tag{4.8}$$

4.5.8 Line Tension

For regular incident waves, the cyclic fatigue line load characteristics were summarized by a time-domain analysis in order to obtain information across all frequencies. A zero-crossing approach was adopted to obtain the average cyclic load after the pre-tension was subtracted ($|T_m - T_0|$). Similar to the motion RAO, the amplitude of line tension was divided by the measured amplitude of the incident waves, as shown in Eq. 4.9.

$$T_c = \frac{|T_m - T_0|}{\zeta} \tag{4.9}$$

For irregular cases, the root mean square of the cyclic tension time series (σ_T) was divided by the root mean square of the free surface elevation (σ_w), as shown in Eq. 4.10.

$$T_c = \frac{\sigma_T}{\sigma_w} \tag{4.10}$$

For survivability situations, the maximum load experienced by the mooring line is compared between configurations.

4.5.9 Uncertainty Analysis

Regular Waves

Wave field spatial and temporal variations are of high importance for array testing due to the large area over which measurements are to be taken. Assuming the measured H values across all the wave gauges to be normally distributed, the empirical rule tells us that 68% of the data should fall within one standard deviation of the sample mean ($\mu \pm \sigma$). It is common to give results with a 95% confidence interval, corresponding to approximately twice the standard deviation of the sample [73]. Ten repeats of a regular wave field ($A = 0.025$ m, $f = 0.63$ Hz) were performed to assess the repeatability of the input conditions. In order to use the assumptions of the empirical rule, one must first assess the level to which the data conforms to the normal distribution. The quantile-quantile (QQ) plot in Figure 4.10a shows the wave heights recorded over ten repeats at a single wave gauge to be normally distributed. The QQ plot in 4.10b also shows the distribution of wave heights spatially across the basin to be normally distributed. Thus, it was deemed sensible to approximate the error related to the wave height measurement, with a 95% confidence interval from a normal distribution. In order to assess the uncertainty on further calculations involving the wave heights, it is necessary to determine the largest source of error; spatial or temporal.

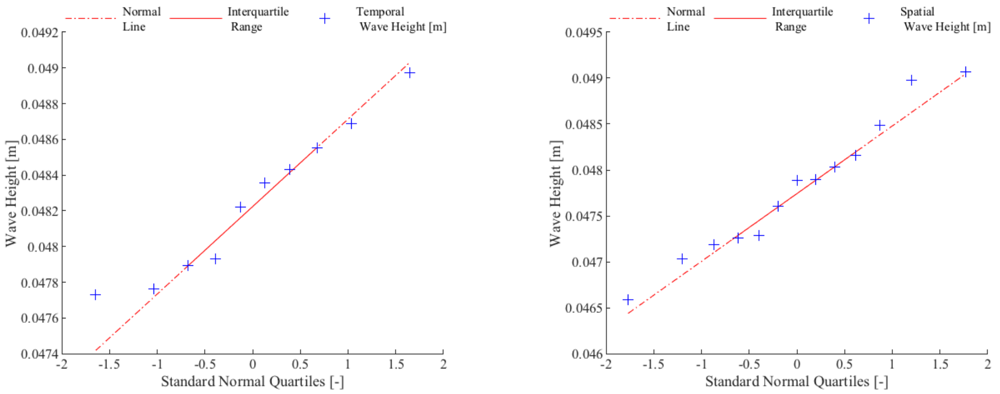

(a) *(b)*

Figure 4.10: QQ plots to assess the conformity of temporal and spatial variability of wave height to the normal distribution. Temporal data (a) is from ten repeats of a regular wave field ($A = 0.025$ m $f = 0.63$) Hz, and spatial data is one test run across 13 wave gauges.

The mean wave heights at each probe across the ten repeats are shown in Figure 4.10a, indicating the temporal variability. The error bars indicate the 95% confidence intervals, with gauge 3 showing the largest difference of circa ±2 mm.

Due to the large spatial area involved in array testing, an ideal situation would be a homogeneous wave field spatially across the area to be tested. In reality this is very difficult to achieve due to reflections and energy spreading in the laboratory environment. The spatial variation can be quantified for all test cases with the same method as the temporal variation. Mean values and standard deviations were calculated spatially over all wave gauges, covering an area of circa $40\,\mathrm{m}^2$. It has been shown in Figure 4.10b, that the spatial variation of measured wave height was normally distributed, so a 95% confidence interval may be used again as the limits for the measurement error.

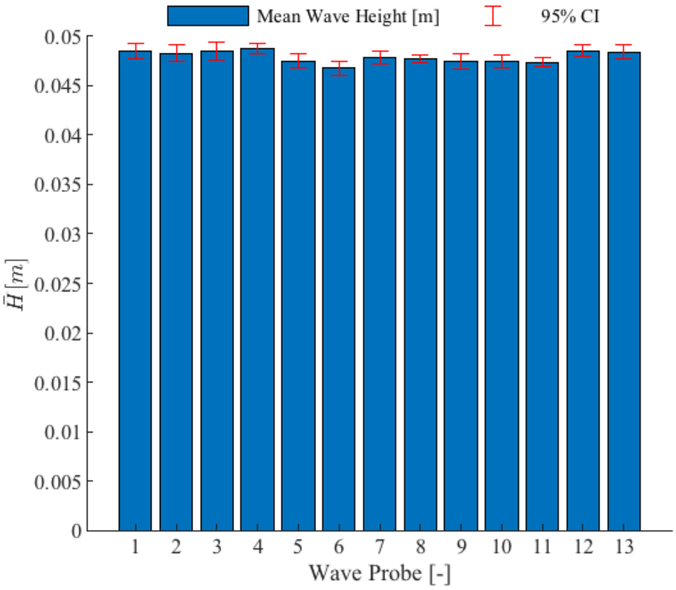

Figure 4.11: Temporal variation in regular wave heights measured across 13 wave probes for ten repeats of waves of $(A = 0.025, f = 0.63Hz)$.

It can be seen from Figure 4.12 that the 95% confidence interval for 0.45 Hz $< f <$ 0.8 Hz was below ± 5 mm due to spatial variations in the measured wave height. As found in other studies [74], higher variability was seen at lower frequencies. As the frequency range of interest, with regard to device and array performance, is is within the frequency range of 0.5 Hz to 0.8 Hz, this was deemed acceptable.

Spatial variations in wave height may be due to reflections from the tank side walls and beach profile opposite the paddles. Therefore, temporal variations in regular wave repeatability have a smaller magnitude (circa ±2 mm), as shown by the repeats at each probe in Figure 4.11. This is expected to be a maximum expected error as it was noted that at this frequency the basin appeared to be resonating and producing a cross wave. The implications of

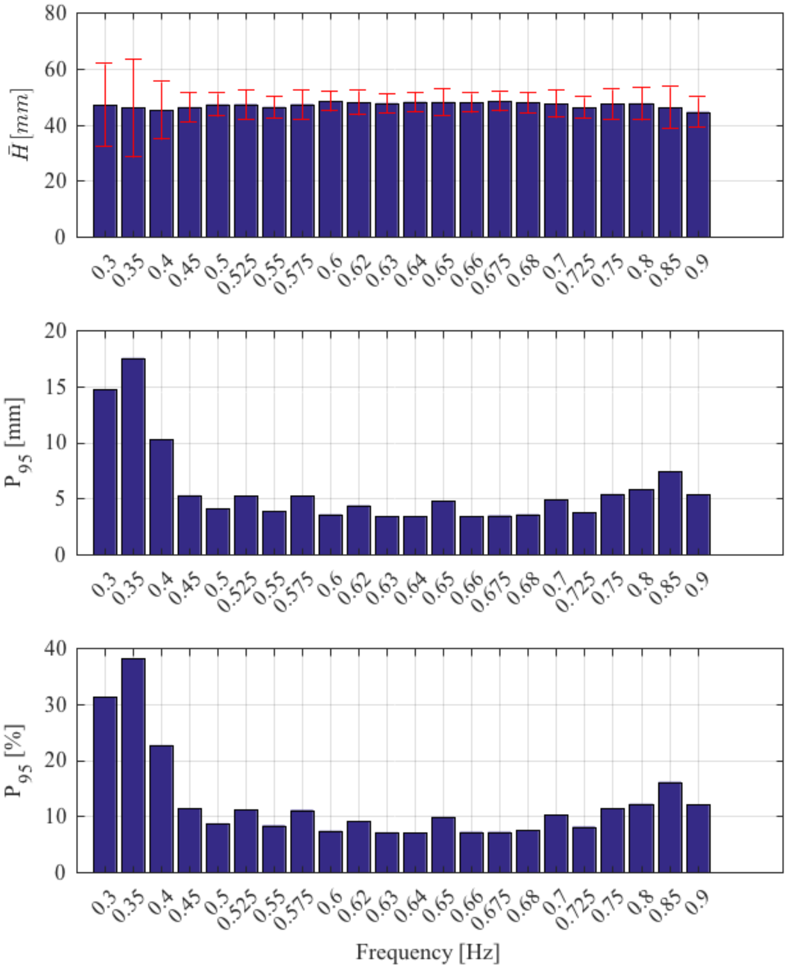

Figure 4.12: Spatial variation of measured wave height H during empty tank tests for regular waves of amplitude ($A = 0.025$ m, $f = 0.63$ Hz). Error bars indicate the 95% confidence interval either side of the spatial mean.

these errors will be discussed in Section 4.5.10.

A similar repeatability analysis was carried out for the frequency of regular waves. Results showed variations were orders of magnitude smaller than the wave height and so this was neglected from any further uncertainty analysis.

Irregular Waves

As was shown for the regular cases, the uncertainty from the spatial distribution of wave heights was considered for the irregular conditions. Each sea state was run in an empty tank with wave gauges measuring the surface elevations. The significant wave height (H_{m0}) was calculated from the measured spectrum at each gauge, using Eq. 2.13 and Eq 2.14.

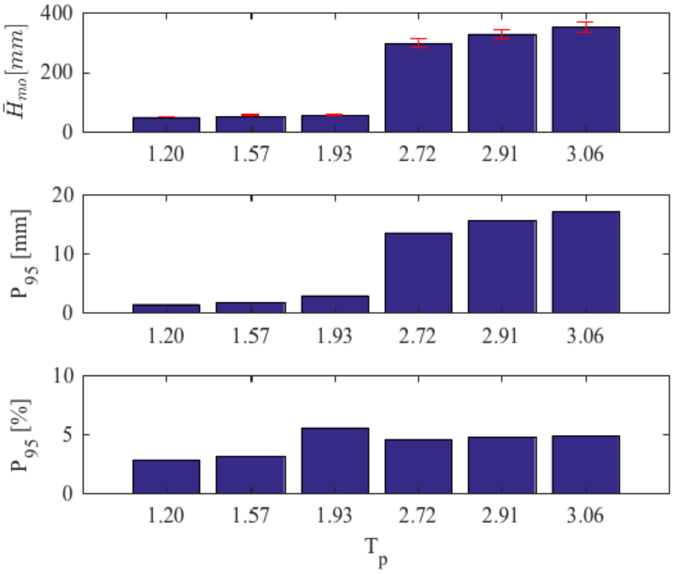

Figure 4.13: Spatial variation of measured significant wave height H_{m0} during empty tank tests for irregular waves in the operational and survivability cases to be tested. Error bars show the 95% confidence interval either side of the spatial mean.

It can be seen from the error bars in Figure 4.13 that the 95% confidence interval in the spatial variation of wave heights in irregular conditions is smaller than that seen in the regular conditions (Figure 4.12), with relative errors under 5%. Although the absolute errors for the survivability cases are relatively high compared to the operational states, relative to their respective means, they are similar in magnitude, as seen by the relative errors.

4.5.10 Propagation of Error

The uncertainty in each measurement must be propagated through to the incident wave power calculation (Eq. 2.9), the device power output (Eq. 4.5) and the capture width ratio (Eq. 4.6). Therefore, assuming the wave height to be the greatest source of uncertainty, the relative error associated with the incident wave power can be calculated as seen in Eq. 4.11, where the incident wave power is calculated as in Eq. 2.9.

$$\frac{\Delta P_{reg/irr}}{P_{reg/irr}} = \frac{\sqrt{\left(\frac{\delta P_{reg/reg}}{\delta H}\Delta H\right)^2}}{P_{reg/irr}} = \frac{2\Delta H}{H} \tag{4.11}$$

As one value of incident wave power is used in further calculations, the spatial variation determined in Section 4.5.9 will be considered as the tolerance on the wave height (ΔH) measurement for all array tests due to the large area covered in the basin. For singular device tests the spatial variation was less apparent due to the constraint of the device to a relatively small space. For this reason, the temporal uncertainty will be considered for single device tests. This value was frequency dependent, as seen in Figure 4.12. The mean wave power was calculated across all wave gauges during an empty tank test and the error was calculated with the appropriate ΔH from Section 4.5.9. For single device tests, wave power at the central location of the basin is calculated, with ΔH correlating to wave gauge five in Figure 4.11.

For irregular waves, the error of the calculated incident wave power has the same relationship with the uncertainty in the significant wave height, as seen in the regular case. The relative error of the incident wave power for irregular cases was equivalent to twice the relative uncertainty in the significant wave height as shown in Eq 4.11.

The measured mean wave power and associated spatial uncertainty for the regular cases is shown in Figure 4.14a, with the theoretical wave power indicated by the red line. The effect of the larger spatial uncertainties on $\overline{H}$ at low frequencies, shown in Figure 4.12, is noticed in the larger error at corresponding frequencies in Figure 4.14a. The theoretical wave power was achieved, considering the 95% confidence interval in nearly all regular cases.

The operational irregular cases have a different H_{m0} to that of the survivability cases. In order to compare all the irregular cases, the measured incident wave powers were normalised by the theoretical incident wave power (P^{*}_{Irr}), as shown in Figure 4.14b. Again, the measured incident wave power for the irregular cases can be considered equivalent to the theoretical incident wave power considering the measurement uncertainty.

The uncertainty in the device power output is related to the pressure measurements within the chamber. As a calibration certificate was provided with the sensors, the accuracy value from the data sheet of 0.25% full-scale output (FSO) is assumed to be the measurement uncertainty of the pressure. If the flow rate is considered as a function of the measured pressure, the full device power output is written as in Eq. 4.12

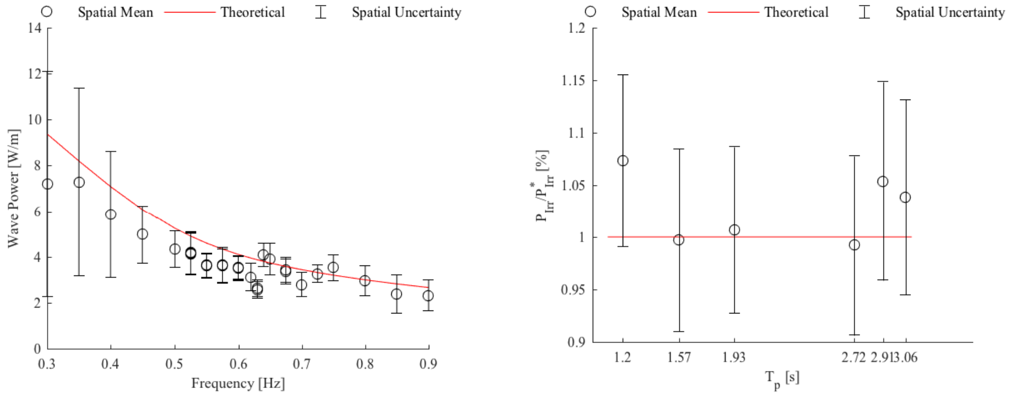

(a) *(b)*

Figure 4.14: Measured incident wave power with associated uncertainties for regular waves of constant amplitude (A = 0.025 m) (a) and measured irregular wave power with spatial uncertainty, normalized by the intended wave power (b).

$$P_{dev} = pAC_D\sqrt{\frac{2p}{\rho}} \tag{4.12}$$

Differentiating P_{dev} wrt to the pressure, p, yields

$$\frac{\delta P_{dev}}{\delta p} = \frac{1.5\sqrt{p}AC_D\sqrt{2}}{\sqrt{\rho}} \tag{4.13}$$

The relative error associated with the instantaneous device power was calculated by Eq. 4.11, by dividing through by the original function and multiplying by the pressure measurement uncertainty.

$$\frac{\Delta P_{dev}}{P_{dev}} = \frac{\sqrt{\left(\frac{\delta P_{dev}}{\delta p}\Delta p\right)^2}}{P_{dev}} = \frac{1.5\Delta p}{p} \tag{4.14}$$

In accordance with Eq.4.5, the instantaneous power is averaged over a time period, resulting in the addition of the individual uncertainties in quadrature.

$$\frac{\Delta\,\overline{P_{dev}}}{\overline{P_{dev}}} = \frac{\sqrt{\sum_{i=0}^{n} \Delta P_{devi}{}^2}}{\sum_{i=0}^{n} P_{devi}} \tag{4.15}$$

where subscript i refers to the instantaneous error of each power measurement and n is the total number of measurements. Finally the uncertainty on the capture width ratio, as calculated in Eq. 4.6, is:.

$$\frac{\Delta CWR}{CWR} = \frac{\sqrt{\left(\frac{\delta CWR}{\delta\,\overline{P_{dev}}}\Delta\overline{P_{dev}}\right)^2 + \left(\frac{\delta CWR}{\delta\,P_{reg/irr}}\Delta P_{reg/irr}\right)^2 + \left(\frac{\delta CWR}{\delta\,W}\Delta W\right)^2}}{CWR} \tag{4.16}$$

$$\frac{\Delta CWR}{CWR} = \sqrt{\left(\frac{\Delta\,\overline{P_{dev}}}{\overline{P_{dev}}}\right)^2 + \left(\frac{\Delta P_{reg/irr}}{P_{reg/irr}}\right)^2 + \left(\frac{\Delta W}{W}\right)^2} \tag{4.17}$$

where ΔW is the uncertainty in the device width measurement, which can assumed to be ±2 mm. The uncertainty in the incident wave power ($\Delta P_{reg/irr}$) and the average device power output ($\Delta\overline{P_{dev}}$) are calculated in Eq. 4.11 and 4.15 respectively. The relative uncertainties on the capture width ratio in each of the variables is summarized in Table 4.3.

Table 4.3 shows the relative error of each variable contributing to the capture width ratio(device power, temporal and spatial incident wave power and the width of the device) calculated at each regular incident wave frequency. It can be seen that the contribution to the overall error associated with the capture width ratio due to device power and device width measurement error

Table 4.3: A breakdown of the variable contributions to the capture width ratio error from the device power, spatial wave power variation, temporal wave power variation and the device width measurements.

		Spatial	**Temporal**	
Frequency [Hz]	$\frac{\Delta \overline{P_{dev}}}{\overline{P_{dev}}}$ [%]	$\frac{\Delta P_{reg}}{P_{reg}}$[%]	$\frac{\Delta P_{reg}}{P_{reg}}$[%]	$\frac{\Delta W}{W}$ [%]
0.30	65.29	69.21	3.97	0.67
0.35	5.93	99.09	4.88	0.67
0.40	14.49	42.36	3.57	0.67
0.45	2.45	23.46	3.71	0.67
0.50	0.25	18.29	3.76	0.67
0.55	0.12	25.13	4.06	0.67
0.60	0.11	14.85	3.66	0.67
0.65	0.12	18.66	3.65	0.67
0.70	0.17	19.60	3.74	0.67
0.75	0.32	22.07	3.84	0.67
0.80	0.91	26.45	4.03	0.67
0.85	2.10	38.43	4.39	0.67
0.90	4.49	24.98	3.71	0.67

is significantly smaller than the incident wave power. At very low frequencies, the device power does contribute significantly, however this is due to the low pressure measurements/power outputs of the devices at these frequencies where performance is of little interest. For this reason, they have been neglected from the error propagation. Thus, in further analysis, the overall error associated with the array capture width ratios is simply related to the error of the incident wave power, caused by spatial variations in wave height at each frequency, as shown in Eq. 4.18. As a singular device is constrained to a single location within the basin, the error associated with isolated device capture width ratios is simply related to the error associated with temporal variation in the incident wave height.

$$\frac{\Delta CWR}{CWR} = \frac{\Delta P_{reg/irr}}{P_{reg/irr}} \tag{4.18}$$

4.6 Conclusion

This chapter has covered the experimental plan adopted to address the aims and objectives set out in Section 1.7 and 1.8. The origins of the environmental conditions tested, the physical layout, measurement methods and calibrations have been critically discussed and the levels of uncertainty quantified. The results characterizing the single device and the hydrodynamic array interactions will next be discussed.

5

Characterization of Isolated WEC and Individually Moored Array Effects

The motion and performance for the isolated device are characterised, in regular and irregular waves. Numerical model results for the isolated device and an analysis of effect of the basin walls on the device response are presented. The array effects are investigated by comparing the responses of $TM3_I$ *with* $TM3_A$ *to indicate a baseline from which the interconnected arrays can be compared. Results showed that hydrodynamic interactions accounted for a maximum of a 10% increase in performance.*

5.1 Decay Tests

To determine the natural resonant characteristics of a single device, decay tests were performed on $TM3_I$ moored in still water. As described in Section 4.5.3, the motions were initiated through a pulley system. The time series of the decay tests are shown in Figure 5.1 with the mean natural frequencies and damping characteristics (ξ_{tot}) shown in Table 5.1. The standard deviations indicate the variation in test repeats. The tests shown in Figure 5.1 and Table 5.1 showed an acceptably small difference between repeats. As expected, the surge and sway natural frequencies and damping characteristics are very similar.

The heave natural frequency falls within the simple approximations in Eq 5.1 [75] for a un-moored floating body.

$$f_z = \frac{1}{2\pi}\sqrt{\frac{\rho g A_{wp}}{m + m_w}} = 0.63 - 0.88[Hz] \tag{5.1}$$

where A_{wp} is the water plane area, m is the device mass and m_w is the added mass, assumed to be within $2m$ and 0 respectively.

These natural frequencies and damping characteristics stand as a baseline from which the array configurations can be compared.

Table 5.1: Mean natural frequencies and associated standard deviations of repeated decay test results for $TM3_I$.

	Natural Frequency [Hz]		ξ_{tot} $[s^{-1}]$	
Degree of Freedom	**Mean**	**SD**	**Mean**	**SD**
Surge	0.0632	0.0006	-0.0210	0.0017
Sway	0.0618	0.0002	-0.0192	0.0017
Heave	0.6514	0.0029	-0.6202	0.0067
Roll	0.1752	0.0104	-0.0228	0.0324
Pitch	0.1794	0.0010	-0.0245	0.0011
Yaw	0.2942	0.0072	-0.0894	0.0305

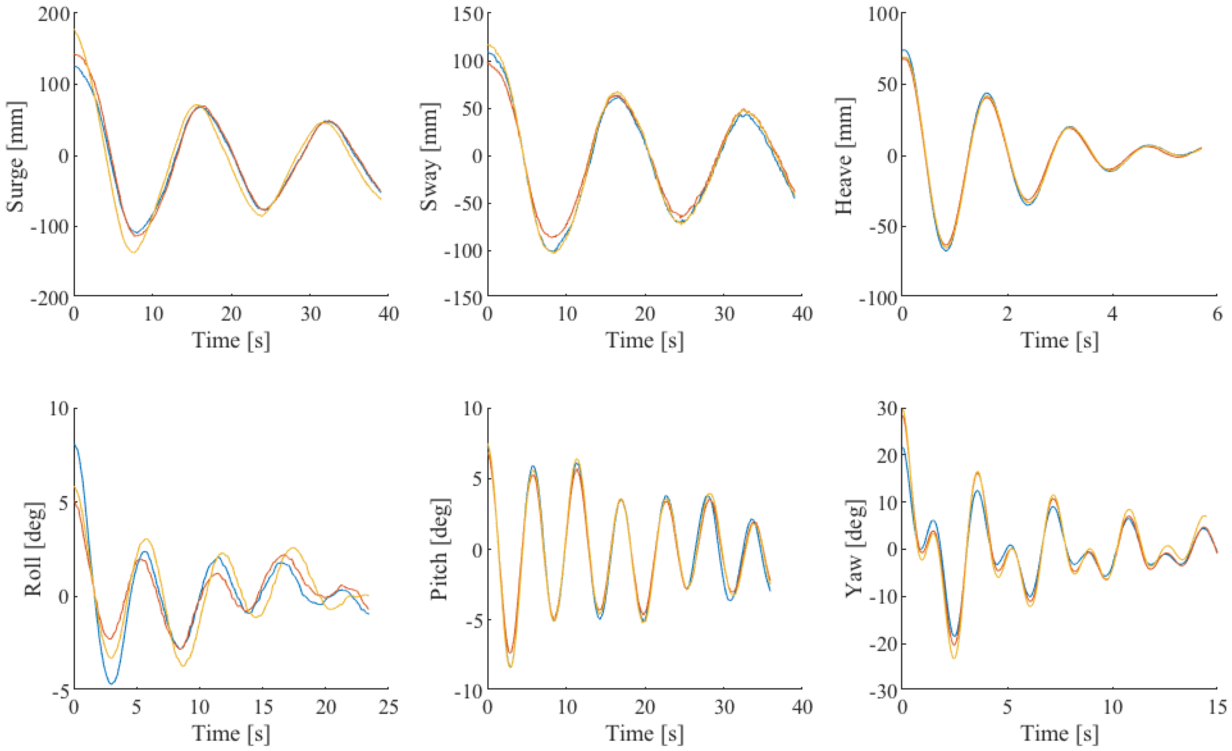

Figure 5.1: Three repeats of decay tests performed on $TM3_I$ for all degrees of freedom.

Table 5.2: Mean heave and associated standard deviations of decay test results for $TM3_I$, $TM3_A$ and $TM2_A$.

	Natural Frequency [Hz]		ξ_{tot} $[s^{-1}]$	
Device	**Heave**	**SD**	**Heave**	**SD**
$TM3_I$	0.6514	0.0029	-0.6202	0.0067
$TM3_A$	0.6353	0.0042	-0.5782	0.0093
$TM2_A$	0.6185	0.0129	-0.4872	0.0068

To highlight the array effects on the device resonant characteristics, heave and surge decay tests were performed on the central device and a corner device, $TM3_A$ and $TM2_A$ respectively. To investigate the effects of the interconnected moorings, heave and surge decay tests were performed on the same devices within the interconnected arrays.

Although Table 5.2 shows differences in the natural frequency and damping characteristics between $TM3_I$, $TM3_A$ and $TM2_A$, they were considered negligible compared to the repeatability indicated by the standard deviations between repeats. Furthermore, $TM2_A$ also shows a very similar natural frequency to that of $TM3_I$ and $TM3_A$.

The surge decay test results for the isolated and individually moored cases are shown in Table 5.3. Differences in natural frequency between $TM3_A$ and $TM2_A$ are noticed due to the differing mooring orientation of each relative to the basin x-axis. Similar to the results for heave, the array effects on the resonant characteristics of the device appear to be negligible.

Table 5.3: Mean surge and associated standard deviations of decay test results for $TM3_I$, $TM3_A$ and $TM2_A$.

	Natural Frequency [Hz]		ξ_{tot} $[s^{-1}]$	
Device	**Surge**	**SD**	**Surge**	**SD**
$TM3_I$	0.0632	0.0006	-0.0210	0.0017
$TM3_A$	0.0607	0.0005	-0.0192	0.0003
$TM2_A$	0.0633	0.0003	-0.0188	0.0037

5.2 Motion

5.2.1 Regular Wave Responses

It is first important to understand the motion responses of the isolated device due to excitation from regular incident waves. The results form an understanding of how the device moves, which can later be linked to performance and mooring line loading characteristics.

The array effects are indicated by comparing $TM3_I$ and $TM3_A$ motion responses. As previously discussed, the performance of the devices is closely related to the heave response of the device. Therefore, the heave response for the isolated device is presented in Figure 5.2 and the remaining degrees of freedom are presented in Appendix 9, Figure 9.1.

The **surge** response is very similar when comparing the two cases indicating negligible array effects.

The **sway** response shows an increased sway response of $TM3_A$ compared to $TM3_I$ due to array effects at incident wave frequencies above 0.5 Hz. However the magnitude is much lower than the other translational responses.

As shown in Figure 5.2, the **heave** response, shows little difference between the cases apart from at f = 0.63 Hz where $TM3_A$ shows a sharp reduction in heave response. This frequency relates to the eighth harmonic of the width of the basin width (Table 4.1), where resonance effects are likely to be contaminating the results. This effect will be further discussed after the remaining motion responses. Interestingly, both devices appear to show a resonant peak at $f = 0.525$ Hz, a lower frequency than the decay test results indicate. Previous studies of floating OWC type WECS, show similar results with a double peaked heave response [76][77], suggesting that the OWC cavity resonance induces a heave response in the system. The natural frequency of the water column can be estimated with the simple analytical approximation in Eq. 5.2 (obtained by reducing the effective length to zero in Eq. 2.18) [75] and is found to be in close proximity to this peak in the RAOs.

$$f_c = \frac{1}{2\pi}\sqrt{\frac{g}{L_1}} = \frac{1}{2\pi}\sqrt{\frac{9.81}{0.9}} = 0.53[Hz] \tag{5.2}$$

where L_1 is the device draught. Previous numerical studies, accounting for the effective length, also show a similar OWC natural frequency of 0.56 Hz [61].

Array effects are apparent in the **roll** response comparing $TM3_I$ to $TM3_A$ seen in Figure 9.1d, however the magnitude of the response is significantly lower than the other rotations. The array effects in **pitch** are similar to that of heave with a maximum increase in pitch of 17% at $f = 0.8$ Hz. Similar trends of array effects are noticed in the **yaw** response with destructive effects caused by the array between $f = 0.5 - 0.6$ Hz and constructive array effects at higher frequencies.

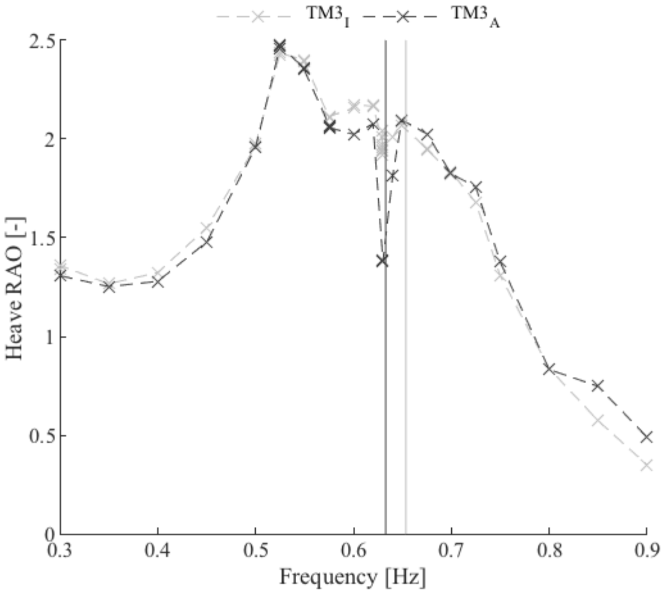

Figure 5.2: Heave motion response amplitude operators for device $TM3_I$ and $TM3_A$, highlighting the array effects. Vertical black and grey lines indicate the natural frequencies calculated from decay tests from Configuration A and an isolated device respectively.

To further investigate the drop in heave response at $f = 0.63$ Hz, wave gauge measurements by the centrally aligned wave gauges are displayed in Figure 5.3. When $TM3_I$ is present the surface elevation at wave gauge one (WG1) appears to show a gradual decrease in wave height compared to the empty basin results. Conversely, the surface elevation at WG3 appears to gradually increase with respect to time compared to the empty basin case. The cross wave gains energy as the tests runs and grows in amplitude. Depending on where the wave gauge is placed, depends on whether a destructive or constructive interference occurs. In the case of WG1 it appears a destructive interference is taking place, reducing the measured wave height as the cross wave increases in amplitude. Conversely, constructive interference is seen at WG3, where the wave height increases over time compared to the empty basin results. At WG5 there is a slight decrease of incident wave height over time, indicating that the wave gauge is close to a node of the standing wave. As the incident and the cross wave have the same frequency, the resultant profile still resembles a typical sine wave. Another indication of the presence of a cross wave at $f = 0.63$ Hz is realized at the end of time series in Figure 5.3, where a larger amplitude wave is noticed compared to the empty basin case. It is likely that this is the cross wave due to the presence of the basin walls, although with no directional information this cannot be confirmed. However, if the device is located in an area of destructive interference between the incident and cross wave, this gives an explanation for the decrease in heave noticed at this particular frequency.

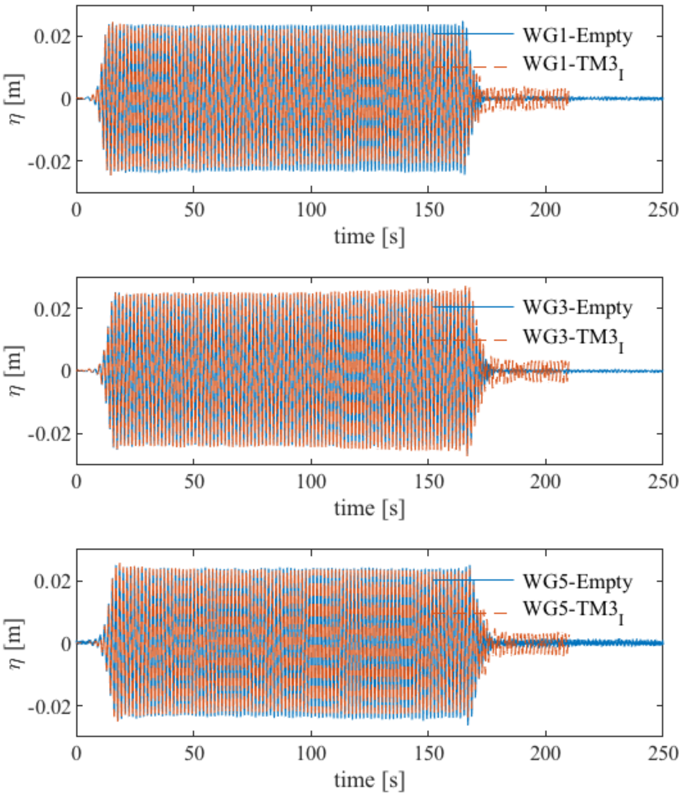

Figure 5.3: $TM3_I$ and empty tank surface elevation time series of regular waves of $f = 0.63$ Hz for three wave gauges located along the centre of the basin. For wave gauge numbering and layout see Figure 4.3

5.2.2 Numerical Simulation

The moored system heave RAO was computed by running time domain simulations of regular waves and analysing the results in the same way as the experimental results, as described in Section 4.5.3. A zero-crossing analysis was carried out on the device heave response to ascertain the response amplitude. This was divided by the incident wave amplitude to obtain the RAO at each frequency, as in Eq 4.2. The results in Figure 5.4 show reasonable agreement between the numerical and experimental data, with the experimental data showing a lower response between $f = 0.6$ to 0.7 Hz and a higher response at $f = 0.5$ to 0.55 Hz. The higher experimental response at lower incident wave frequencies is due to resonance of the water column, which is not included in the numerical model. The over prediction of the numerical model between $f = 0.6$ to 0.7 Hz is due to the decoupled nature of the model where only heave is considered, as well as viscous effects neglected by the numerical model. To assess the effect of this over predicted peak, irregular cases run during the experimental campaign were simulated and compared, as shown in Figure 5.5. The numerical model can be seen to perform reasonably well, but over estimates responses in the peaks and troughs slightly. The ratio of measured to predicted root mean squares shows the numerical model to over predict the heave displacement, for the operational case $f_p = 0.64$ Hz $H_s = 0.05625$ m, by 5.6%. These errors would be expected to be reduced when more degrees of freedom are modelled.

5.2.3 Numerical Simulation with Walls

To assess the effects of the tank walls on the experimental motion responses of the device, walls were added to the simulation. The regular wave simulations described above were repeated with the basin walls present and the results were inspected for sharp decreases in device heave response around an incident wave frequency of $f = 0.63$ Hz, as was observed in the experimental data. The multiple body interactions were calculated in Nemoh. The walls were modelled as two dimensional panels in order to ensure no diffractional effects from the wall thickness are included, as shown in Figure 5.6. The walls were translated to match the position of the tanks walls during exper-

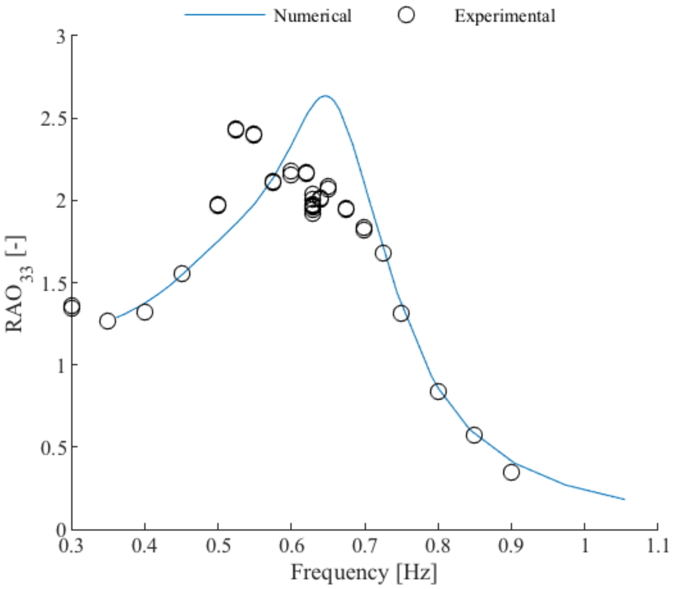

Figure 5.4: A Moored device with a linear damping coefficient PTO heave RAO for regular waves of incident wave height 0.025 m at model scale.

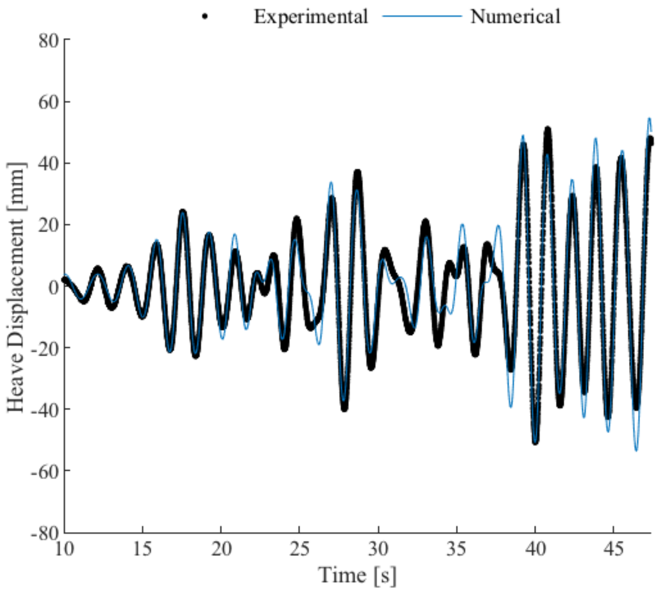

Figure 5.5: The heave displacement time series from the numerical model and physical experiments for an irregular model scale sea state of $H_s = 0.05625m$ and $f_p = 0.64$ Hz.

imentation. To reduce computational expense, the walls were modelled as non-hydrodynamic bodies and a fixed constraint was used to fix the walls to the seabed in the time domain model. The same linear damping coefficient was applied to the device as determined in Section 3.6.1. The nominal mooring configuration was added to the simulation and a sweep of regular wave cases was run.

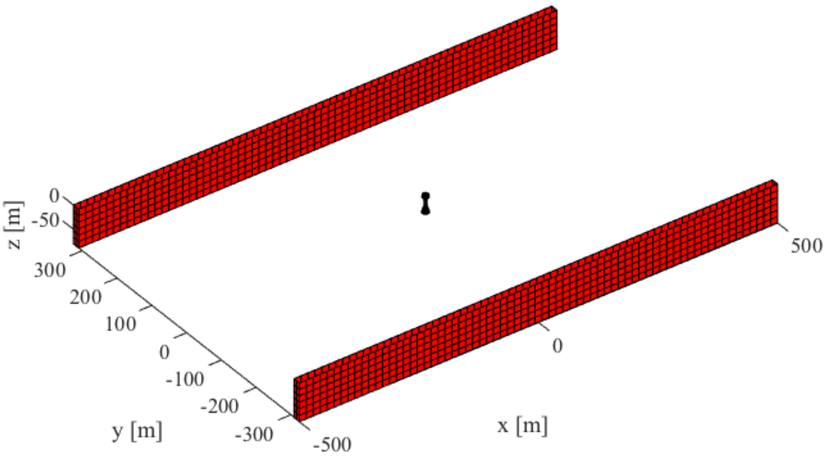

Figure 5.6: The mesh used to model a single device with tank walls

It can be seen from Figure 5.7 that the walls cause difference in the heave response of the device at $f = 0.63$ Hz. This is exactly the behaviour that was measured in the physical experiments. This supports the postulation that the walls are causing the measured drop in heave response during experi-

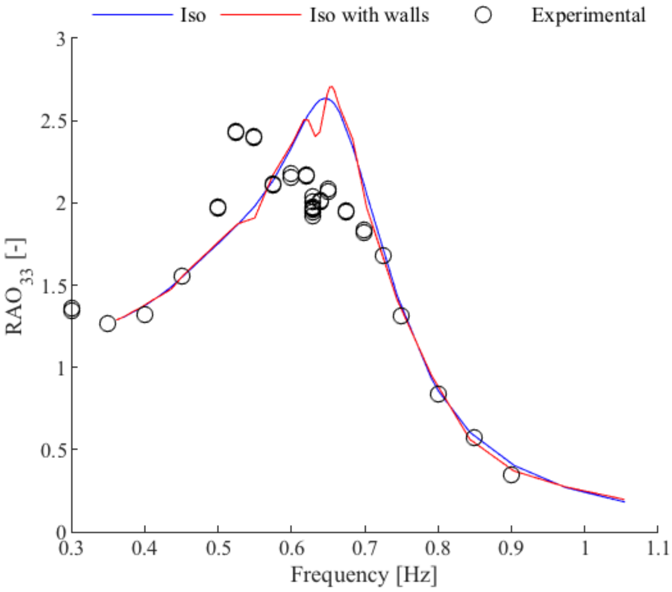

Figure 5.7: Heave RAO's for a single device with and without walls and experimental data for comparison

mentation, and the associated drop in performance at this frequency. This indicates that a full scale open ocean deployment of the arrays may not experience the measured performance drop noticed during experimentation and therefore the annual energy extraction calculated in Section 6.4 is under predicted. Alterations to the device heave response with walls present can also be seen at $f = 0.55$ and $f = 0.43$ Hz in Figure 5.7. These frequencies relate to the fourth and sixth harmonics of the width of the basin. The decrease in heave is greatest at $f = 0.63$ Hz due to resonance of the device radiating waves laterally in the basin to the greatest extent at this harmonic.

Considering the diameter of the devices, the wave length corresponding to $f = 0.63$ Hz is very close to the 4 m lateral array spacing of the devices. This increases the radiated energy laterally in the basin, meaning the constructive/destructive interference (depended on the device position) exacerbates the effect of the cross wave on the device motion response.

This finding also confirms why a peak in the heave experimental data of Figure 5.7 does not match that of the decay test results shown in Section 5.1. The decay tests results are not affected by the walls as the radiated waves do not have sufficient time or energy to cause significant changes to the natural frequency. However, when regular wave tests of greater amplitude and duration were run, the tank effects become noticeable and mask the peak in the heave RAO.

To ensure that the decrease in heave response is not also linked to array effects, multiple devices were also modelled and analysed.

5.2.4 Numerical Simulation of Array Effects

To assess the effects of multiple devices within the array, the interaction needs to be understood. The array effects have been modelled using Nemoh with a multibody input file, as shown in Figure 5.8. The computational demands of Nemoh are quadratically related to the number of panels in the mesh file. Unfortunately, one can only state one line of symmetry for any given system. As there are multiple bodies translated to different locations, this symmetry assumption cannot be utilized. Thus, the mesh shown in Figure 3.10 was mirrored and translated to the correct spatial position. As a result, for a single device, doubling the number of panels results in four times greater calculation time with Nemoh. When modelling three devices, the computation time is 25 times greater than a single device assuming symmetry. It is for this reason that only three devices of the array were modelled, with the assumption that any lateral interaction between devices would still be apparent with fewer devices.

MoorDyn, currently does not cater for multiple sets of moorings, so the array analysis considers unmoored conditions and is purely to investigate if sharp changes in heave motion response, with changes in frequency exist due the presence of other devices in close proximity.

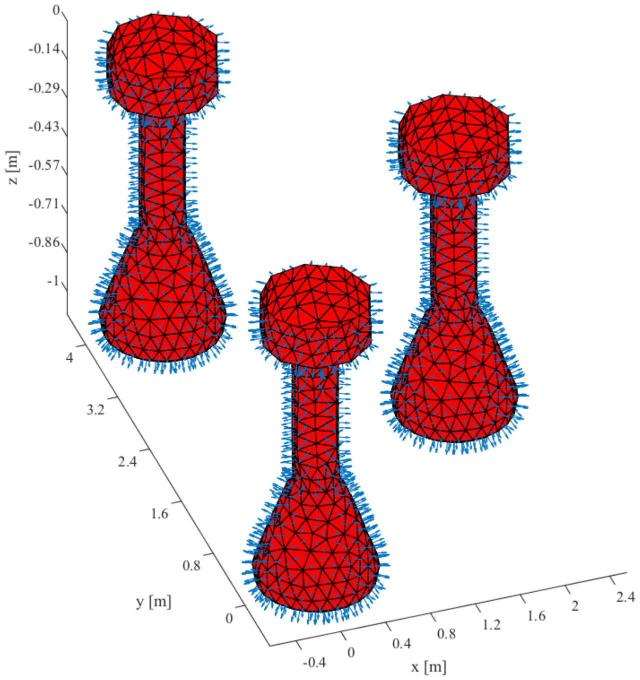

Figure 5.8: The mesh used to model an array of three devices with four metre spacing between the front most devices and a central device two metres behind.

It can be seen from Figure 5.9 that there is a 17% difference in the heave response of the front devices compared with the central device, as noticed in the moored experimental results.

Importantly, the presence of the other devices within the array does not appear to be causing any sharp irregularities in the devices response as no-

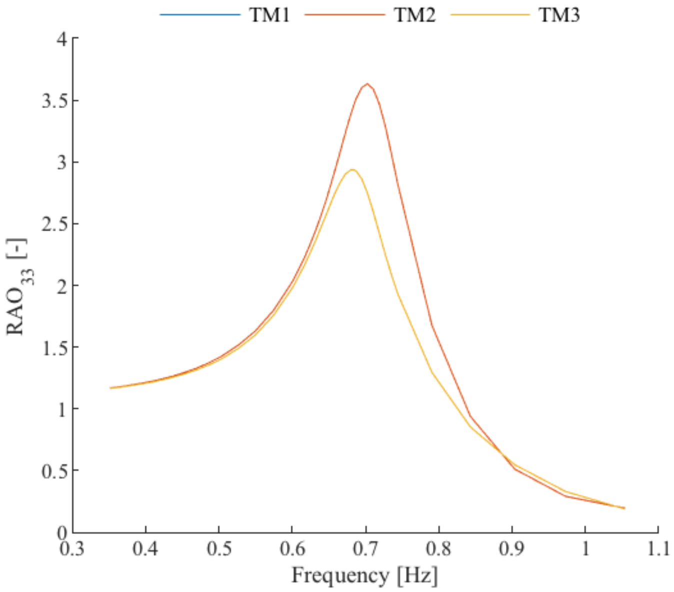

Figure 5.9: Heave RAO's for an array of three devices. Due to array symmetry $TM1$ and $TM2$ show identical heave responses and overlay one another.

ticed in numerical and experiential data in Figure 5.7 in the presence of the tank walls. Thus, as postulated from physical tests, it appears that the walls cause the decrease in heave, power and line loading response at circa 0.63 Hz, rather than array interactions. This confirms that the unexpected results noticed in experimentation are not due to array effects or the mooring interconnections and may not be apparent in an open ocean scenario.

5.3 Performance

It is important to differentiate between hydrodynamic interaction effects and the effects purely due to the interconnecting mooring systems. Thus, the following section compares $TM3_I$ and $TM3_A$ to give a baseline to which the interconnected arrays can be compared.

5.3.1 Regular Wave Responses

To assess the array effects, $TM3_I$ and $TM3_A$ capture width ratios are compared in Figure 5.10a, with the uncertainty as calculated in Section 4.5.9. Similar performance characteristics can be seen between the two devices, indicating small array effects with respect to performance. At low frequencies, the performance is identical until the array begins to cause destructive interference at around $f = 0.5$ Hz. The array causes the performance of $TM3_A$ to drop by approximately 20% compared to the isolated case until $f = 0.63$ Hz. The peak performance for $TM3_I$ appears to be around $f = 0.6$ Hz, slightly lower than the natural heave frequency from the decay tests. Likewise, the peak performance for $TM3_A$ is around $f = 0.65$ Hz, close to that of the associated heave decay tests, where a 10% performance increase is noticed. A slight peak is seen around $f = 0.525$ Hz for both $TM3_I$ and $TM3_A$, corresponding to peaks in the heave response in Figure 5.10 (a) and related to the OWC cavity natural frequency. Considering the maximum point absorber limits described in Section 2.3.2, the peak performance of both $TM3_I$ and $TM3_A$, relates to a total energy conversion efficiency of circa 42%.

Figure 5.10b compares the total power extracted by Configuration A and five times the isolated device. The measurement uncertainty in the capture width ratio of Configuration A is due to the spatial variations in the wave height discussed in Section 4.5.9. Considering the level of measurement uncertainty it is very difficult to differentiate between the two and quantify the array effects due to the relatively large spatial variation in wave height during array testing.

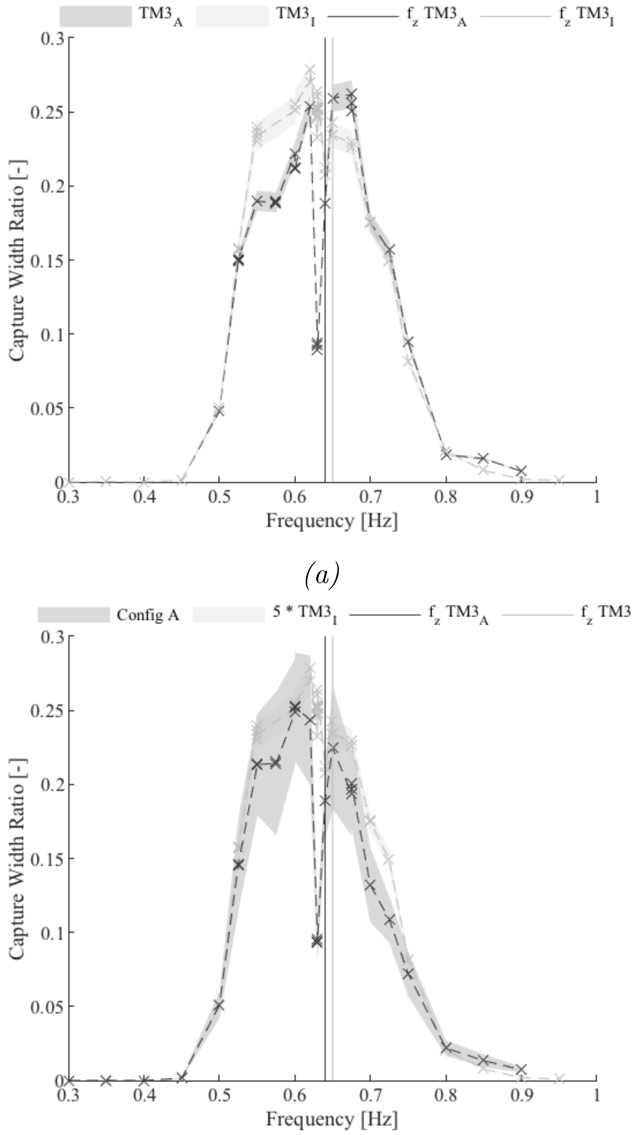

(a)

(b)

Figure 5.10: Capture width ratios for $TM3_A$ and $TM3_I$ (a). Capture width ratios of Configuration A and five times power output from $TM3_I$ (b). Both with an incident wave amplitude of 0.025 m. The shaded areas indicate the level of uncertainty as calculated in Section 4.5.9 and the vertical lines indicate the heave natural frequencies of the $TM3_A$ and $TM3_I$.

5.4 Conclusion

Decay tests and regular wave RAO results have shown negligible differences due to hydrodynamic array interaction. However, with the aid of the numerical model, a sharp decrease in the array configuration has been attributed to a standing wave in the basin. This suggests that in an open ocean scenario, one would not expect to see such decreases in heave response or performance. A maximum performance improvement of 10% due to array effects was measured as the baseline from which the interconnected arrays can be compared.

6

WECs in Interconnected Arrays

The motion and performance responses of the interconnected arrays in regular and irregular waves is presented and compared to the hydrodynamic array effects discussed in the Chapter 5. Implications of these performance alterations is explored through the prediction of energy extraction subjected to the conditions at Leixões, Portugal. Results show a natural frequency shift of the devices, resulting in a 211% increase in peak performance and a 75% increase in annual energy yield at the deployment site.

6.1 Decay Tests

Table 6.1 shows that interconnecting the devices shifts the natural heave frequency towards slightly higher frequencies for both $TM3$ and $TM2$ devices. Between the interconnected cases, there does not appear to be a great difference in the natural frequencies, suggesting the level of connectivity will not make a significant difference to device heave resonance. As a result, one would expect to see different heave behaviour between the individually moored and the interconnected cases due to the different mooring configuration when exposed to regular waves. Additionally, one would expect to see little difference in the heave responses of the interconnected cases as the damping properties and natural frequencies appear to be so similar. As discussed in Section 2.4, the heave response of the device is closely linked to the performance. Thus, one would expect similar resonant performance characteristics of the interconnected arrays, as discussed in Section 2.4.

Due to the complex device interaction, it was difficult to deduce any helpful information regarding the surge resonant characteristics for the interconnected array cases. The results were highly dependant on initial conditions and therefore yielded poor repeatability. As a result, surge decay test results for the interconnected array configurations are not included.

Table 6.1: Mean heave and associated standard deviations of decay test results for array configurations

	Natural Frequency [Hz]		ξ_{tot} $[s^{-1}]$	
Device	**Heave**	**SD**	**Heave**	**SD**
$TM3_A$	0.6353	0.0042	-0.5782	0.0093
$TM2_A$	0.6185	0.0129	-0.4872	0.0068
$TM3_B$	0.6767	0.0010	-0.4542	0.0064
$TM2_B$	0.6731	0.0010	-0.4508	0.0012
$TM3_C$	0.6790	0.0000	-0.4476	0.0022
$TM2_C$	0.6857	0.0028	-0.4413	0.0040
$TM3_D$	0.6797	0.0021	-0.4525	0.0027
$TM2_D$	0.6749	0.0052	-0.4482	0.0033

6.2 Motion

6.2.1 Regular Wave Responses

The effects of the interconnecting moorings is next analysed by comparing the motion responses of the array configurations and will later be used to explain performance and line tension characteristics. The motion responses have been separated into outer ($TM1$, $TM2$, $TM4$, $TM5$) and inner devices ($TM3$). The mean motion of the outer devices will be collectively referred to as TMO with a subscript when referring to a particular mooring configuration. Due to the large area being covered by the motion tracking system, accurate measurements of all devices were not possible. As a result, for this analysis $TM1$ has been excluded from the average. As stated in Section 4.5, motion response amplitudes were obtained from 50-75 response cycles.

Figure 6.1 compares the key motion response of $TM3$ and TMO with the different array configurations. The motion responses of all degrees of freedom can be found in Appendix 9, Figure 9.2 and 9.3. The **surge** response (Figure 6.1a) of $TM3$ in all configurations appears to be similar except for a large peak in Configuration D at incident wave frequency $f = 0.525$ Hz. This is not seen in the outer devices to such an extent (Figure 6.1d), suggesting that the configuration with square inter-connections has a different response frequency.

Investigating the $TM3_D$ surge response time series at this $f = 0.525$ Hz in both the time and frequency domain, shows an underlying low-frequency response at close to $f = 0.2$ Hz. This frequency is very close to the isolated device pitch natural frequency and the incident wave frequency is close to the third harmonic, suggesting a strong coupling effect between the pitch and surge response. This seems intuitive as the fairlead connections are at a distance from the centre of mass, resulting in a turning moment on the device. This is supported by a large peak noticed at the same frequency in the pitch response of both Figure 9.2e and 9.3e. The slope of the surge responses indicates a frequency-dependence, but there is no global resonance peak within the frequencies tested. This is concurrent with the findings of the surge decay tests (Table 5.3) where a peak would be expected below $f = 0.3$ Hz.

Large peaks around $f = 0.5$ Hz in the **pitch** and **roll** motion response of both the inner and outer devices are very clear in Configuration C and D. The $TM3$ roll response is significantly smaller than that of TMO. Similar to the yaw response, the four point fairlead system of the central device increased the reactive force to roll motions. Interestingly, by removing a seabed line and moving to the single line from the outer devices (Configuration B to C), the central device behaves very differently. The single point bottom line on TMO_C and TMO_D allows all devices to pitch and roll significantly more than TMO_B at this particular frequency.

The **sway** responses for all cases were considerably smaller than the other translations for the inner and outer devices in all configurations. At higher incident wave frequencies, TMO_D showed a larger response than the other configurations, whilst at low frequencies the $TM3_B$ and $TM3_C$ showed a significant increase compared to the other configurations. $TM3$ in all configurations shows a low response in sway compared to TMO. At the lower test frequencies, $TM3_B$ and $TM3_C$ appeared to show a higher response compared to $TM3_A$. A peak is noticed in $TM3_D$ at $f = 0.525$ Hz, related to the pitch and roll resonance discussed above. Interestingly, across the central frequency space tested, the sway response of the interconnected $TM3$ appears very similar to that of $TM3_A$, even though it is moored with a four-point fairlead system.

A clear increase in **heave** is seen in Figure 9.2 and Figure 9.3 for all the interconnected cases at higher incident wave frequencies for both $TM3$ and $TM2$. The decrease in heave response around $f = 0.63$ Hz is noticed for both the individually moored and interconnected arrays, suggesting it is likely to be due to excitation of array width (4 m) and basin harmonics, as indicated in Table 4.1, rather than a mooring effect. The third harmonic of the distance between the outer devices and the basin walls (5.75 m) is $f = 0.62$ Hz, indicating a further source for the build up of standing waves close to the frequency where the decrease in heave is noticed.

As explained above, this is why the natural frequency from the decay tests does not appear to be on a resonant peak in the RAOs. To further support this theory, the numerical model of this configuration created by Harnois et al [78] and the model created in Section 3.6, that neglected the effects of the walls, does not show this behaviour in any of the simulations and the natural frequency matched that found in the experimental decay tests. Peaks in all configurations are again noticed at $f = 0.525$ Hz relating to the OWC cavity resonance inducing a heave response of the device. At lower incident wave frequencies, the interconnected cases of $TM3$ and TMO appear to heave less than $TM3_A$. A clear heave resonance shift towards $f = 0.7$ Hz can be seen in Figure 9.2c and 9.3c for the interconnected configurations and can be attributed to the interconnecting moorings. This resonance aligns with the decay test results, however tank effects may be masking a true peak at a lower frequency. This resonance shift is also supported by the numerical model [78].

The **yaw** response is very different between $TM3$ and TMO. By removing the square interlinking lines from TMO_C and increasing the pretension in the diagonal interlinking lines, a frequency shift in the $TM3_D$ response is induced, moving the yaw peak to higher frequencies. The magnitude of the $TM3_D$ yaw response (Figure 9.2f) is much smaller than that of TMO_D (Figure 9.3f) due to the constraint from the four-point fairlead system. TMO in the interconnected cases appear to behave very similarly with a peak yaw response around $f = 0.5$ Hz.

To further investigate the coupling between the pitch and surge responses, the time series of $TM3$ and $TM2$ was analysed in the frequency domain as shown in Figure 6.2 and Figure 6.3 respectively. The plots show the incident wave frequency on the x-axis, the Discrete Fourier Transform (DFT) frequency on the y-axis and the component amplitude on the colour axis. For visualisation purposes, a linear interpolation has been made between test frequencies. It can be seen for both $TM3_A$ (Figure 6.2) and $TM2_A$ (Figure 6.3), the response is linearly related to the incident wave frequency. In Configuration B, for both the inner and outer device, there is a response at the wave driving frequency, but there is also an underlying low-frequency drift response in surge. This low frequency response is due to resonance of the mooring system. It is not seen in the pitch or heave response for either $TM3_B$ or $TM2_B$. The response of $TM3_C$ and $TM2_C$ show both the linear surge response and the low-frequency drift, as well as a slight peak at circa $f = 0.2$ Hz on the DFT frequency axis. This response was also noticed in the pitch response. This effect is magnified when the square interconnections are removed in Configuration D. This analysis further supports the postulation that the large spikes in the the surge and pitch RAOs, noticed in Figure 6.1, are due to strong coupling effects due to the position of the fairleads with respect to the centre of gravity of the device.

The motion responses discussed in this section will be referred to with regard to device/array performance and the line tension characteristics.

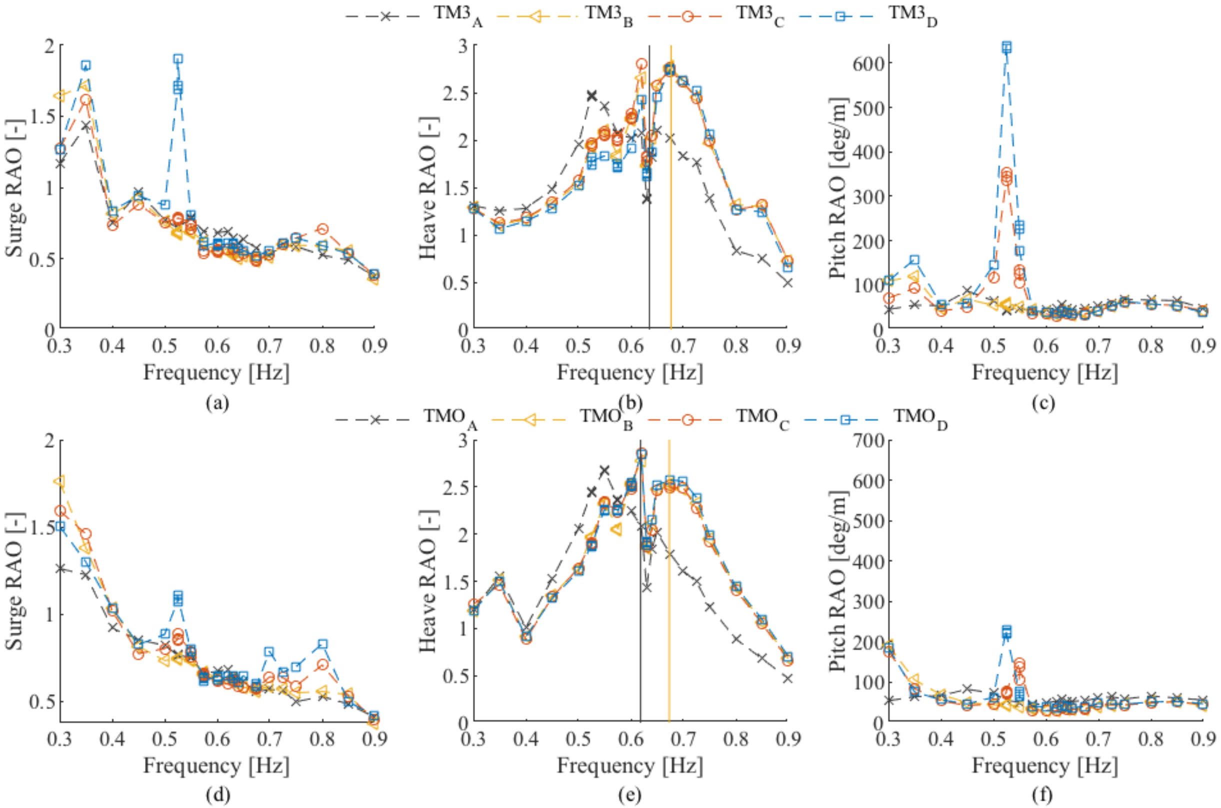

Figure 6.1: Motion response amplitude operators for the inner device ($TM3$ - top row) and the average outer device (TMO - bottom row) of the arrays in all configurations. Motions are surge, sway, heave, roll, pitch and yaw, (a)-(f) respectively. Vertical black and orange lines indicate the natural frequencies calculated from decay tests from $TM3_A$ and $TM3_B$ in the top row and $TM2_A$ and $TM2_B$ in the bottom row respectively.

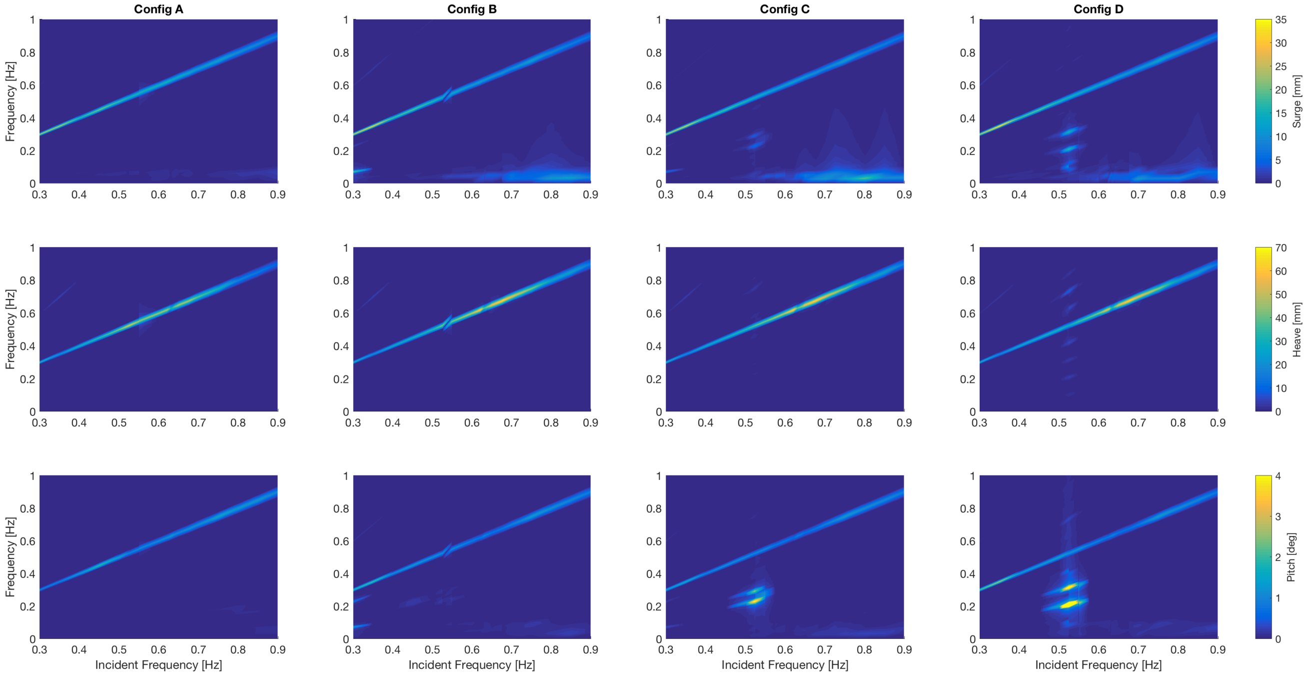

Figure 6.2: The frequency-domain response of the central device $TM3$ for regular waves of varying incident wave frequency and constant amplitude ($A = 0.025$ m).

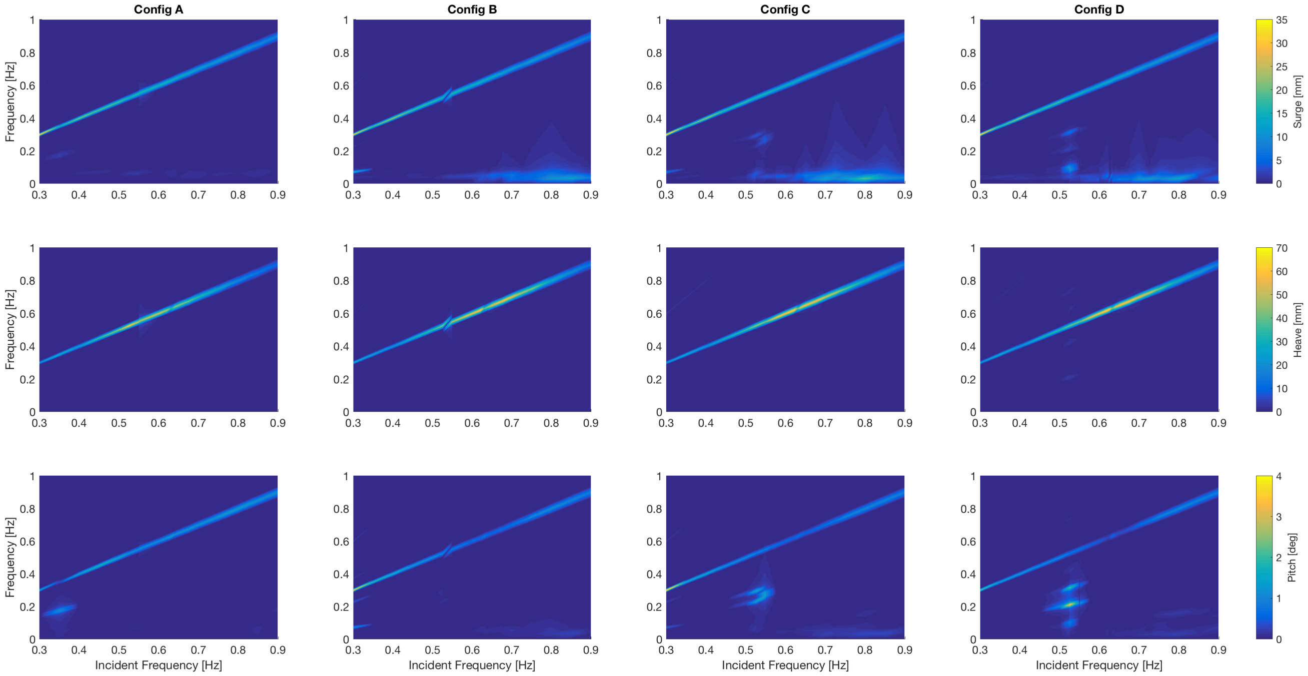

Figure 6.3: The frequency-domain response of the outer device $TM2$ for regular waves of varying incident wave frequency and constant amplitude ($A = 0.025$ m).

6.2.2 Irregular Wave Responses

The motion characteristics of the arrays in operational sea states have been summarized to later link to the performance and line loading responses, as well as indicate behaviour in realistic conditions.

The average heave motion responses of the outer devices (TMO) and $TM3$ of each of the configurations in irregular sea states are shown in Figure 6.4. Results from the remaining degrees of freedom are presented in Appendix 9 Figure 9.4.

Array and hydrodynamic interaction effects are noticed by comparing the heave motion response of $TM3_I$ (dashed grey line) and $TM3_A$ (dashed black line) in Figure 6.4. It appears that the array effects are negligible at the peak frequencies tested, however it is difficult to draw any quantitative conclusions as only two conditions were tested for the isolated device. Importantly, the array effects appear to be smaller than the differences in motion response alterations due to the interconnecting mooring systems. The largest array effect of 3% is seen in Figure 6.4, whilst the mooring configuration enhances the heave response by up to 20%.

In all degrees of freedom, the difference between $TM3$ and TMO shown in Figure 9.4 appeared to increase for each configuration as the number of interconnections reduced. As might be expected, this suggests that an individually moored array behaves more homogeneously than an interconnected case, where the magnitude of the motion in question varies spatially across the array. This may result in spatial differences in the performance and line loading characteristics within the interconnected arrays.

There is a noticeable difference between the interconnected and individually moored cases with regard to the **surge** response. The interconnections significantly reduced the constraint in surge in all the irregular cases tested. This effect was not observed in the regular wave responses, indicating non-linearity in the surge response for differing incident wave amplitudes.

A clear difference between the interconnected and individually moored cases can be seen in the **heave** response shown in Figure 6.4. By comparing the difference between the central and corner devices for each configuration, an indication of the spatial variation in motion response is given. The spatial differences in the heave response increases as the level of interconnectivity reduces, indicating that one might expect the spatial distribution of the power to be related to the level of interconnectivity. The interconnected cases seem to all have a similar heave response that is greater than the individually moored case in all the irregular cases tested.

Between the interconnected cases, Configurations B and C seem to behave very similarly in all degrees of freedom with comparable averages and similar spatial variations. This suggests that moving from two bottom mooring lines to a single one did not significantly affect the motions of arrays in operational sea states.

Although similarities between the regular and irregular wave RAOs can be noticed, it is difficult to make direct comparisons due to the small number of sea states tested. The motion characteristics in operational irregular waves described above will later be linked to the performance and line loading.

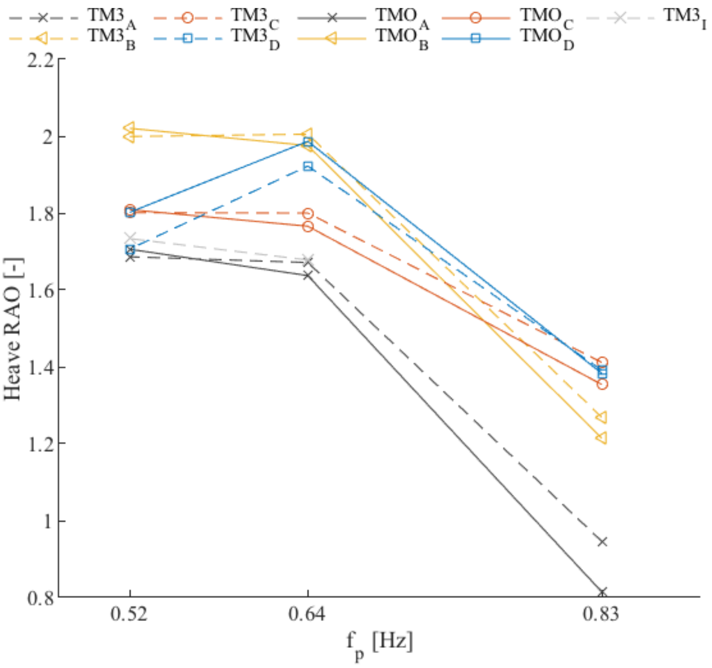

Figure 6.4: Array *rms* heave motion responses for irregular cases with dashed lines for $TM3$ and solid lines for the average of the outer devices.

6.3 Performance

It is important to quantify the performance of the array configurations to assess if the potential cost savings associated with the reduction in anchor requirements will be affected by alterations to energy extraction potential. The array performance relative to Configuration A is next analysed to assess the performance implications of the interconnected mooring systems, neglecting the hydrodynamic interactions.

6.3.1 Regular Wave Responses

Figure 6.5a and Figure 6.5b show the capture width ratio of the central device and the entire array for each mooring configuration plotted against incident wave frequency respectively.

It has been previously shown from the motion responses in regular waves in Section 6.2.1, that the interlinking of devices results in a higher natural frequency of heave motion response compared to the individually moored case. The effect of this on the performance can be seen in the $TM3$ capture width ratio curve of the inter-connected arrays compared to $TM3_A$ in Figure 6.5a. Furthermore, the higher natural frequency seems to be beneficial to energy extraction. The peak heave motion responses shown in Figure 9.2c indicates a 10% increase due to the interconnection of devices. However, due to the higher frequency of the response in the interconnected cases, it resulted in a beneficial phase difference between the heave of the device and the water column, which resulted in a peak performance increase of 211%. Furthermore, the performance of $TM3$ within the interconnected arrays appeared very similar, no matter how the connections were made. The interconnected cases also appear to have a broader-banded spectrum compared $TM3_A$. This is highly beneficial to the energy extraction potential for the concept of interconnected arrays. There is a secondary peak in the interconnected spectra around $f = 0.55$ Hz. This is close to the natural frequency of the internal water column. Again, a peak in $TM3_A$ capture width ratio is noticed around $f = 0.65$ Hz corresponding well to the decay test results and a secondary peak is seen at the OWC natural frequency.

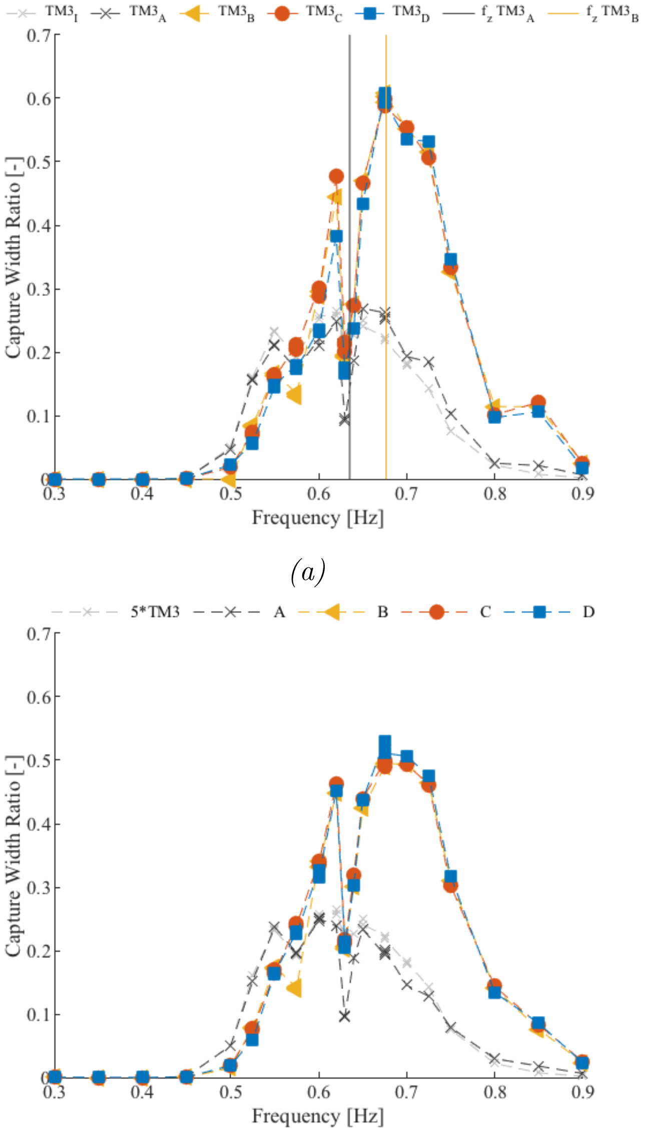

(a)

(b)

Figure 6.5: Capture width ratios for the central device ($TM3$) in all Configurations (a) and the capture width ratios for the total array in each Configuration (b). Vertical black and orange lines indicate the heave natural frequencies from decay tests of $TM3_A$ and $TM3_B$ respectively. Both with an incident wave amplitude of 0.025 m.

Basin resonance effects, excited by the array at $f = 0.63$ Hz becomes very pronounced for all the interconnected cases (Configurations B,C and D). This becomes more obvious because of the higher power outputs at this frequency.

The total array outputs (Figure 6.5b) show similar trends to the Figure 6.5a. Again, the impact of the shift in heave natural frequency as discussed in Section 6.2.1 is observed in the total array capture width ratio curves. The interconnected array cases all behave very similarly with regard to efficiency and extract more energy due to the phase difference resulting in a larger relative motion between the device and the water column at these higher frequencies. A small peak around $f = 0.55$ Hz is noticed for both the interconnected and the individually moored cases, relating to the water column natural frequency. The frequency shift correlates well with the heave responses shown in Figure 9.2c and Figure 9.3c. Figure 6.5b shows Configuration A can be seen to outperform the interconnected arrays at $f = 0.55$ Hz by circa 44%. The corresponding difference in heave response shown in Figure 9.2 and Figure 9.3 is around 25%, but due to the less favourable phase difference between the device and the water column, the larger increases in performance noticed at the higher frequencies are not realised.

The effect of the mooring configurations, neglecting the array affects, can be clearly seen in Figure 6.6, where the $q_A - factor$ has been calculated relative to Configuration A. Unlike the usual derivation of the interaction factor, $q_A - factor$ indicates the effect of the mooring system on the array performance neglecting the hydrodynamic interactions. It can be seen that performance enhancements for $TM3$ at higher frequencies due to the interconnecting moorings are much greater than the performance enhancements due to array effects compared to $TM3_A$. A similar effect is noticed in Figure 6.6b for the total array output. This result shows that the use of interconnecting mooring line architecture can be beneficial to energy extraction for an OWC type converter arrays.

In order to check the phase difference stated above, in accordance with forced oscillator theory it is assumed that the surface elevation of the internal water column is phase shifted by $\frac{\pi}{2}$ with respect to the internal OWC cylinder pressure. To test this linear assumption, the orifice calibration rig described in Section 3.4 was used, as both the internal pressure and the piston position is known. The DFT is calculated for both the pressure and the piston displacement, subtracting the phase angles from the peak responses, as shown in Figure 6.7.

Results from all calibration tests shown in Table 3.4, yield the phase differences between the pressure and the piston displacement to be within $\pm 0.5\%$ of the nominal $\frac{\pi}{2}$. Thus, it was deemed acceptable to use this approximation to investigate the phase angle difference between the estimated OWC chamber surface elevation and the body heave phase for the regular wave tests. The phase of $TM3$ heave and pressure was calculated using the DFT for all Configurations. The difference between the estimated water column phase and the heave displacement was then calculated by Eq. 6.1.

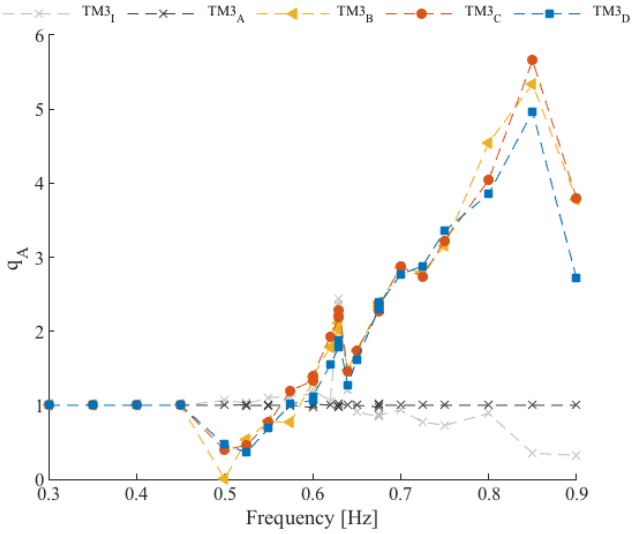

(a)

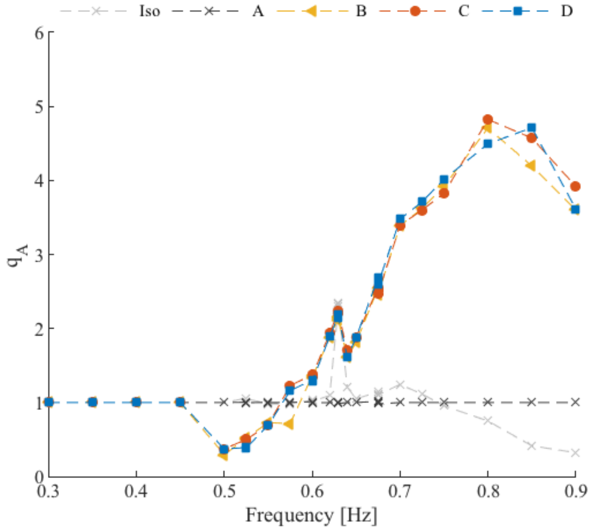

(b)

Figure 6.6: q_A for $TM3$(a) and for all devices (b) in all Configurations.

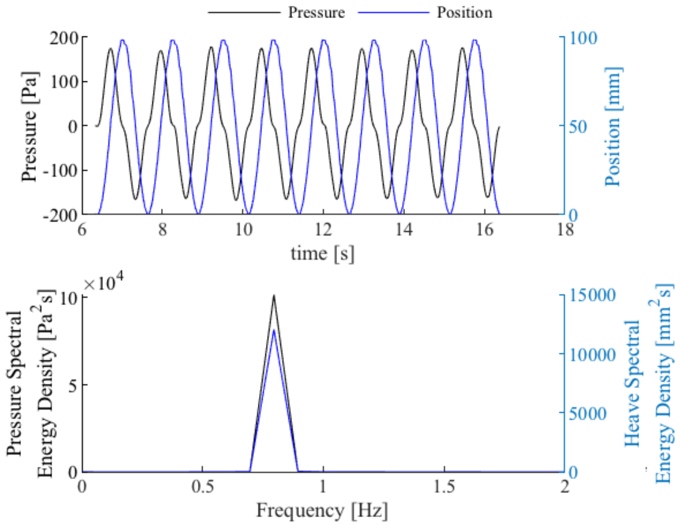

Figure 6.7: Phase relation between the position of the piston head and the internal chamber pressure in the time and frequency domain for a test at $f = 0.7$ Hz.

$$\delta\theta = \angle max(Z(f)) - \left(\angle max(P(f)) + \frac{\pi}{2}\right) \tag{6.1}$$

where $Z(f)$ is the frequency-dependent DFT of the time dependent heave displacement $z(t)$, and $P(f)$ is the frequency-dependent DFT of the time-dependent chamber pressure $p(t)$.

It can be seen from Figure 6.8 that at the higher frequencies tested, the phase difference between the water column and the device's heave response tends towards π, as also found by [79]. This is where the water column and the device heave is close to 180 degrees out of phase, thus in a beneficial state for energy extraction. The resultant air passing through the orifice will be the volume of air associated with device heave displacement *plus* the displacement of the water column. Conversely, at the lower frequencies tested, the heave of the device and the water column are nearly exactly in

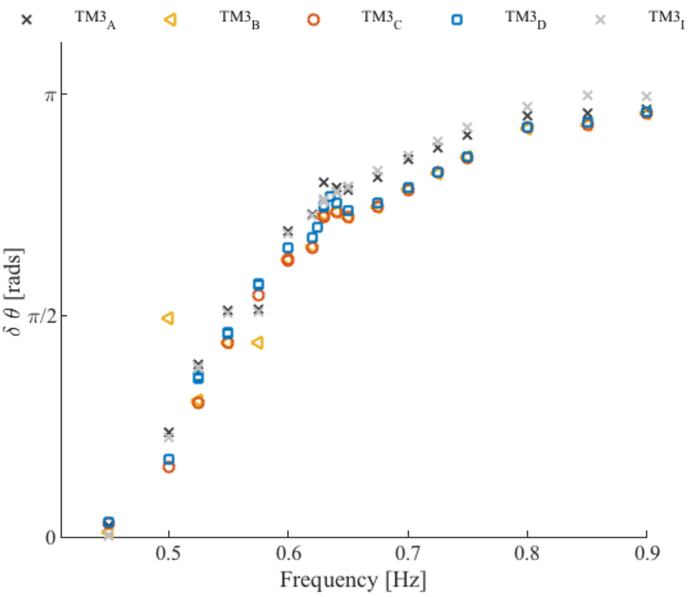

Figure 6.8: The phase difference between the predicted water column and the device heave motion for the central device in all Configurations, excited by regular waves.

phase with one another. As a result, the air being forced through the orifice is due to the heave of the device *minus* the height of the water column.

The uncertainty in the incident wave power can be incorporated into the result with the methodology described in Section 4.5.10, with results shown in Figure 6.9.

It can be seen from Figure 6.9 that considering the measurement uncertainty due to the spatial variation of the incident wave power, shows no discernible difference between the interconnected arrays. However, the difference between Configuration A and the interconnected cases, is still apparent, confirming the findings of the analysis above.

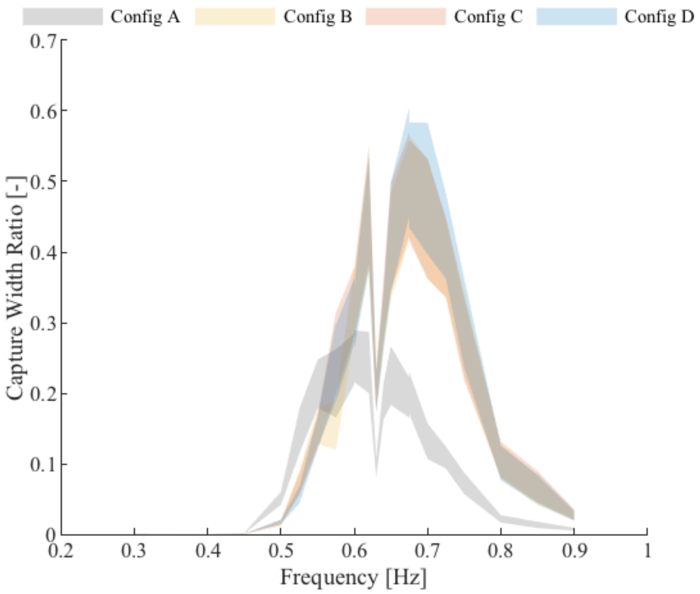

Figure 6.9: Capture width ratios of the array configurations with the shaded areas indicating the error on the measurement due to spatial wave field variations.

6.3.2 Irregular Wave Responses

The irregular wave test data was analysed to assess the performance in realistic operational sea conditions and to confirm the characteristics noticed in the regular wave tests.

By comparing Figure 6.10 to Figure 6.9, the general capture width ratios are seen to be lower for the irregular sea states than the regular cases. This is due to the sea states having a proportion of incident wave power that does not excite the devices at the extremities of the wave spectrum, as well as non-linear effects. The array effects seen between the $TM3_I$ and $TM3_A$ are minimal and show similar trends to those noticed in the heave motion response shown in Figure 6.4.

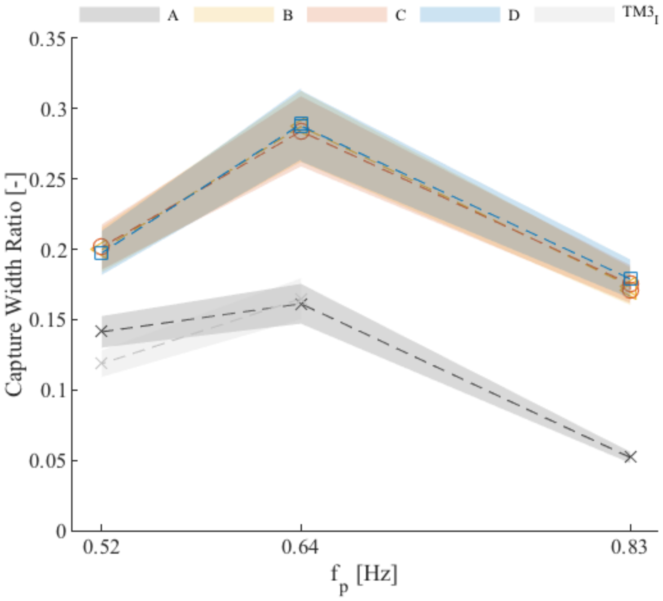

Figure 6.10: Capture width ratios against peak frequency for all Configurations in irregular sea states of constant $H_s = 0.05625$ m with shaded areas indicating uncertainty due to spatial variations in incident wave power.

It can be seen from Figure 6.10 that again, the interconnected cases outperform the individually-moored and isolated cases. The performance enhancement between the interconnected and individually-moored cases is less than that noticed in the regular wave tests, but greater than the difference due to array effects at each frequency tested. The performance enhancement due to the interconnections appears to diminish towards the lower frequencies tested. This would suggest that at some frequencies, outside of the tested frequency space, the performance of the interconnected cases could be less than an individually moored array, although this would need confirming through further numerical and physical studies of more irregular cases. Intuitively, based upon the regular capture width curves seen in Figure 6.5b, one would expect for this to be the case at lower frequencies. Again, considering the uncertainty due to the spatial variation in H_{m0}, one is unable to differentiate between the interconnected cases.

To investigate the array effects noticed in Figure 6.10 at $f_p = 0.52$ Hz between $TM3_I$ and $TM3_A$, the frequency spectrum of the pressure and heave motion response are shown in Figure 6.11. The effects of the array on the wave field close to the devices can be seen in Figure 6.11 (a). Diffraction and radiation from the devices and subsequent reflection from the tank walls in Configuration A appear to be altering the wave field at $f > 0.5$ Hz compared to the isolated case. A peak in the wave field is clear at $f = 0.65$ Hz. This links very closely to a peak in the pressure and the heave spectrum. As noticed in the regular waves cases, this frequency is closely linked to the width of the array, the basin and device resonant frequency. Therefore, this array effect is likely to be over-predicted by the experimental results.

Linearity of Response

In order to assess the linearity of the heave response, the regular RAOs from Figure 9.2 have been multiplied by the incident wave spectrum shown in Figure 6.11 (a). The results shown by the dashed lines in Figure 6.11(b) can be seen to over-predict the heave response. This indicates non-linear behaviour at different incident wave amplitudes. At $f < 0.55$ Hz, the measured heave response is greater than the linear RAO predicts, and at higher frequencies, the predicted response over-estimates the response. This information suggests that further experimentation in irregular sea states is required to fully

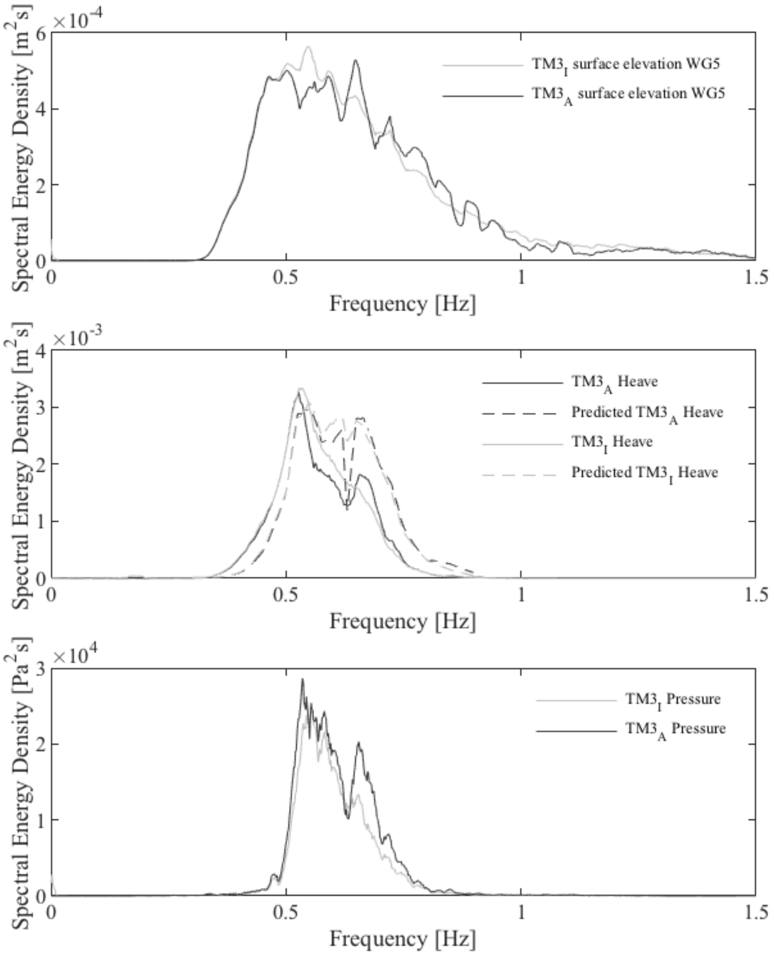

Figure 6.11: Frequency-domain plots of the incident wave field, device heave and pressure response from the central device of Configuration A and the isolated case for operational sea state with $f_p = 0.52$ Hz.

capture the array characteristics in operational sea states.

Power Distribution

To consider the spatial distribution of the energy extraction across the arrays, the power attenuation between the front and back of the array has been calculated for each configuration. As the device layout remains consistent across all configurations, the power attenuation will be a directly related to the mooring configuration only. The power loss between front to back of the array (α) has been calculated as in Eq. 6.2.

$$\alpha = 1 - \left(\frac{\overline{q_b}}{\overline{q_f}}\right) \tag{6.2}$$

where $\overline{q_b}$ is the average $q_0 factor$ of $TM4$ and $TM5$ and $\overline{q_f}$ is the average q-factor of $TM1$ and $TM2$.

It can be seen from Figure 6.12, that for the sea states tested, the attenuation of the interconnected Configurations is greater than the individually moored case in all cases. For Configuration D, the attenuation is nearly double that of the individually moored case, which is very similar to the reduction in motion homogeneity noticed in Figure 6.4. Interestingly, by moving to a single seabed line (Configuration B to C), the power attenuation is reduced. This indicates that although the interconnected arrays have enhanced energy extraction potential, the spatial distribution of the performance is more variable than that of an individually moored concept. This suggests that individual device tuning through optimizing damping/stiffness

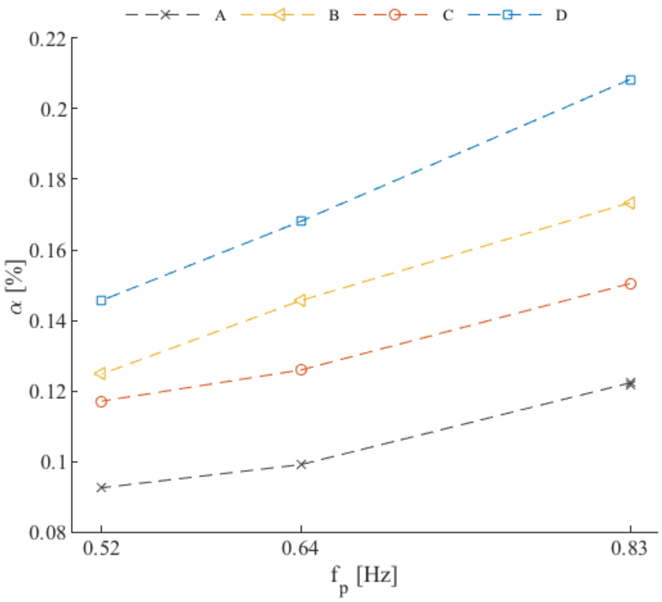

Figure 6.12: Power attenuation for each array configuration.

characteristics, is of greater importance in the design of an interconnected array than in an individually-moored case.

6.4 Operational Performance

This research has shown that interconnected mooring systems for compact wave energy converter arrays offer potential enhanced performance and mooring load characteristics. As expected, the mooring systems tested alter the resonance characteristics of the arrays. Previous work showed close links between the device heave response and the performance. It was shown in this chapter that although the magnitude of the peak heave response of the devices was similar, the frequency at which this motion took place had a significant implication on the energy absorbed. The phase difference between the water column and the body heave was shown to be beneficial for energy extraction towards the higher frequencies tested. In order to realize the effect of this frequency shift on the array annual yield for the proposed deployment site of Leixões, Portugal, a linearised prediction was made utilizing experimental data.

6.4.1 Methodology

In order to compare the configurations with regard to the site of Leixões, the occurence matrix (Figure 4.6) and the regular capture width curves (Figure 6.5b) are used to predict the annual energy extraction at Leixões of each configuration using the methodology set out in [80]. The assumption of linearity in this method is further discussed in the Section 6.4.3. From this point onward, any values of base S or C are frequency dependent variables, otherwise values are scalar constants and subscripts n and m refer to each H_s and T_p of each sea state of the occurrence matrix described in Figure 4.6.

The incident wave energy available to the array associated with each sea state of the occurrence matrix is calculated from the Pierson-Moskowitz spectrum as shown in Eq. 6.3.

$$E_{n,m} = 8760 \rho g W J_{n,m} \int_{0}^{\infty} S_{n,m}(f) C_g df \tag{6.3}$$

where $E_{n,m}$ is the total energy of the sea state, $S_{n,m}$ is the frequency dependent spectral energy density, W is the total width of the devices within the array (5*12 m device diameters), $J_{n,m}$ is the occurrence matrix and C_g is the wave group celerity.

The total energy available to the array per annum is therefore the sum of the energy available across all possible sea states as shown in Eq 6.4.

$$E_{net} = \sum_{n} \sum_{m} E_{n,m} \tag{6.4}$$

The frequency dependant incident wave power per meter wave crest (S_p) is defined as in Eq. 6.5.

$$S_{pn,m}(f) = \rho g S_{n,m}(f) C_g(f) df \tag{6.5}$$

The power output from the arrays was then calculated by multiplying Eq. 6.5 by the capture widths and integrating with respect to frequency, as shown in Eq 6.6. The experimentally measured array average capture width ratio curves from Section 6.3 were first multiplied by the total width of the devices within the array and scaled to full scale by multiplying the frequency axis by the Froude scaling factor of $40^{-0.5}$. In order to match the frequency discretisation of the capture width curves to that of the incident wave power spectrum, a linear interpolation between the experimental data points of the capture width curves was made. Eq. 6.6 was calculated for all possible sea states within the occurrence matrix, for all four array configurations.

$$P_{Ai,m} = \rho g \int_{0}^{\infty} S_{n,m} C_g CW_A df \tag{6.6}$$

Where $P_{Ai,m}$ is the scalar average power output with the subscript indicating the configuration and sea state, CW_A is the associated capture width curve. Although theoretically Eq. 6.6 is an infinite sum, practically this is calculated between the frequency bounds of the experimental data ($f = 0.3$—0.9 Hz).

The array power matrix was then multiplied by the occurrence matrix and the total hours per annum to calculate the total extracted energy yield for each seas state (E_{AExt}) for each configuration, as shown in Eq. 6.7.

$$E_{Aextn,m} = 8760 P_{An,m} J_{n,m} \tag{6.7}$$

The total efficiency (ε) of each array configuration is then the ratio of extracted energy (E_{out}) to the available incident energy (E_{in}).

$$\varepsilon = \frac{E_{out}}{E_{in}} = \frac{\sum_n \sum_m E_{Aextn,m}}{E_{net}} \tag{6.8}$$

6.4.2 Method Validation

In order to check the assumptions stated in Section 6.4.1, the method is used to predict array power outputs in the operational sea states tested in the basin to make a direct comparison of predicted to measured values. It can be seen from Table 6.2 that the linear approximation method makes a reasonable prediction of the power outputs, especially for the interconnected cases. Configuration A shows the most divergence, with the model over predicting the case of f_p =0.83 Hz by circa 12% and under predicting the $f_p = 0.64$ Hz and $f_p = 0.52$ Hz by 5-8%. The source of this error is likely due to non-linear behaviour of the system to varying incident wave amplitude, as well as effects of the linear interpolation utilized between test cases.

Table 6.2: Ratio of predicted to measured power outputs for experimentally tested irregular wave conditions.

$\frac{P_p}{P_e}$	**Config A**	**Config B**	**Config C**	**Config D**
$f_p = 0.83$ Hz	1.12	0.98	0.99	0.99
$f_p = 0.64$ Hz	0.92	0.97	1.02	1.00
$f_p = 0.52$ Hz	0.95	0.99	1.03	1.04

6.4.3 Results

An annual yield was estimated for each configuration using the capture width curves derived from regular wave tests. By assessing the energy present in each sea state of the probability matrix, the total annual resource shows an available energy across the five device diameters of circa 15 GWh, assuming sea states to conform to a long crested Pierson-Moskowitz spectrum.

A clear difference can be seen from Figure 6.13 between the individually moored and the interconnected cases. The interconnected cases extract much more energy over all, particularly in the lower period sea states, as expected due to the higher peaks seen in the regular capture width ratios. The configurations achieve overall extraction efficiencies (ε) of 9%, 9 %, 16 %, 16 % and 16%, for five isolated devices and from Configuration A to D respectively. These relatively low efficiencies are believed to be due to the broad banded nature of the resource. Furthermore, as was shown by the numerical model in Section 5.2.3, the decrease in heave and associated capture width ratio at $f = 0.63$ Hz would not be realized in an open ocean situation. As a result, one would expect these efficiencies to be slightly higher in an open ocean scenario, although as the water column is not included in the numerical model, accurate performance predictions cannot be drawn. To give perspective to the potential efficiency gains through interconnected compact arrays; according to Ofgem, the average UK household consumes 3300 KWh of electrical energy per year [81]. Thus, the individually moored configuration has the potential to power around 400 homes every year of service. By connecting the devices together in any of the interconnected configurations tested the number of homes increases to circa 700. Therefore, there is potential that, not only can developpers make cost reductions through a reduction in the number of anchors required, but can also extract significantly more energy, further reducing the LCOE. It must be noted here that in scaling up these results, one must accept that the scale effects are non-trivial [82] and while laboratory scale trends might be expected to reflect full scale situations well, specific power predictions should be treated with caution.

Despite the errors discussed in Section 6.4.2, a 75% increase in energy extraction through interconnection is greater than the errors related to the linear assumptions and so the predictions can be seen as indicative of the true potential interconnected arrays have on performance enhancement.

The overall performance enhancement of the interconnected arrays tested is not sensitive to the level of interconnectivity, however the attenuation of power output across the array was shown in experimental results to be linked. These alterations to the array characteristics indicate the importance of designing these systems specifically as interconnected arrays, rather than retro-fitting interconnecting lines to existing devices. Furthermore, due to the increased spatial variation in device power, the importance for individual device tuning is greater for interconnected arrays. The increases in

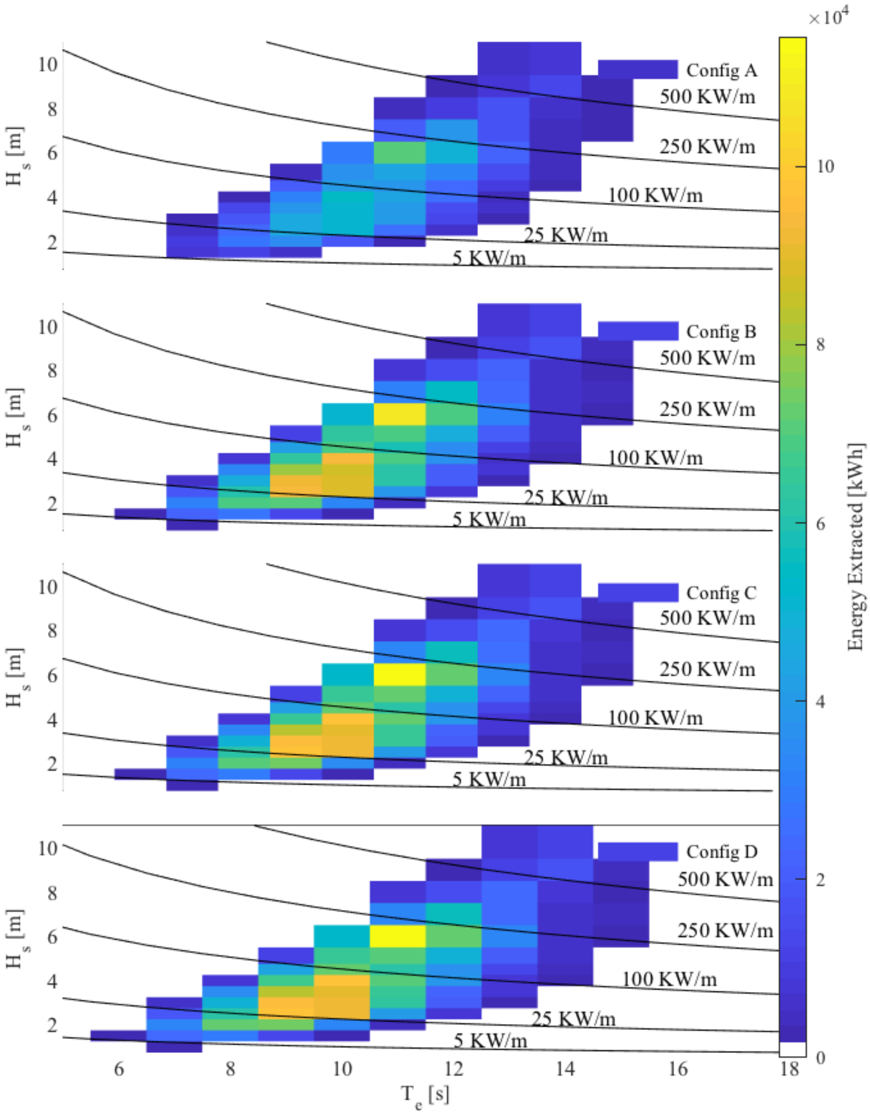

Figure 6.13: Energy extraction matrix for all configurations for the occurrence matrix of Leixões, Portugal.

annual yield predicted for the Leixões deployment site are the direct impact of the interconnecting moorings altering the natural frequency of the devices, resulting in a beneficial phase shift between the water column and the device body. This suggests that the high level of performance enhancement may be specific to OWC type converters, therefore to understand the impact of interconnectivity on other types of converter, further work is required.

It was shown in Section 6.3, that the performance is closely linked to the heave motion response. Physical testing would suggest that the performance of the isolated device, and to a greater degree the arrays, decreases at an incident wave frequency of $f = 0.63$ Hz. However, the numerical model indicates this not to be the case, suggesting that if the devices were in an open ocean situation the heave response may be greater than measured in the physical experiments. Without the modelling of the internal water column, it is not possible to quantify the increase in performance, however as an approximation, if the performance is considered linearly related to the heave response for each frequency, a 30% increase in performance could be expected at $f = 0.63$ Hz in open water. The linearised annual yield predictions do not account for this, indicating that further performance enhancements could be realised in an open ocean scenario.

6.5 Conclusion

Decay test and regular wave RAO results shown the interconnected arrays to have a higher heave natural frequency than that of the individually moored case. This was found to create a beneficial phase shift of the water column relative to the device and thus, an enhanced peak performance by 211%. Similar results were found for testing in operational sea states. The performance enhancement was not found to be related to the level of interconnectivity, however the distribution of the power within the array was. The power attenuation between the front and back of the arrays was shown to be inversely proportional to the level of interconnectivity for the configurations tested. The results were contextualized by predicting an annual energy yield for each array at Leixões, Portugal, where the interconnected arrays were shown to provide a 75% increase.

7

Mooring Line Loading in Interlinked Arrays

The mooring line loading fatigue characteristics of the interconnected devices is considered in regular and irregular waves. The level of interconnectivity on the fatigue loading of the mooring lines is then presented and linked to the motion responses. The chapter concludes with an analysis of the motion responses of the devices and the extreme mooring line loading experienced by each of the configurations in extreme sea states. Results showed the the ability of interconnected mooring systems to reduce the fatigue and peak loading on mooring lines, compared to an individually moored case.

7.1 Line Loading

The line tension characteristics are of vital importance in the progression of the concept of interconnected arrays. If the interlinking of devices results in high line loading, the line costs could exceed the cost saving associated with the reduction in anchor numbers. Furthermore, higher mooring loads would result in the need for larger, more costly anchorage systems with regard to construction material and deployment. The pre-tension and cyclic loading characteristics for each mooring line in regular and irregular wave conditions were studied to assess each configuration.

7.1.1 Mooring Line Pre-Tension

It has been shown that mooring pre-tension plays a significant role in the characteristics of a wave energy converter system [83]. The mooring line pre-tensions are an inherent property of the mooring design as discussed in Section 2.2 and 3.5. It is important to consider the pre-tension when analysing the fatigue loading of mooring systems as fatigue damage is due to the cumulative effect of both the mean and cyclic loading, therefore the pre-tension of each Configuration were measured in still water. In order to compare the mooring line pre-tensions with respect to the individually moored case, the pre-tensions are presented in Table 7.1 as a percentage of pre-tensions realised for each line in Configuration A. For load cell number locations see Figure 4.5 on page 88.

It can be seen from Table 7.1, that the pre-tension in all interconnected cases are lower than in the individually moored configuration.

Table 7.1: Pre-Tension of similarly positioned mooring lines in all array configurations. For Load cell positions, refer to Figure 4.5 on page 88.

	Pre-Tension [%A]							
Line Type	Config A		Config B		Config C		Config D	
Seabed	$TM2_{Aa}$	100.00	$TM2_{Be}$	11.14	$TM2_{Cd}$	28.18	$TM2_{Db}$	24.23
Square	$TM2_{Aa}$	100.00	$TM2_{Ba}$	23.00	$TM2_{Ca}$	22.44	$TM3_{D}$	NA
Diagonal	$TM2_{Aa}$	100.00	$TM3_{Bd}$	51.52	$TM3_{Cd}$	51.71	$TM3_{Dd}$	71.12

The seabed lines in Table 7.1 shows the pre-tension for the front most **seabed line** in each configuration connected to device $TM2$. It can be seen that seabed line $TM2_{Be}$ had tension circa 11% of that of an individually moored device. As expected, when a single seabed line is used to moor the arrays, as in Configuration C and D, the pre-tension rises, but is still significantly lower than $TM2_{Aa}$, due to the reduced mass of the clump weight required to achieve a similar stiffness.

The second row of Table 7.1 shows the **square** interconnections in Configurations B and C. Again, the pre-tension required to achieve similar stiffness is significantly lower than that of the individually moored case. It appears that using one seabed line (Configuration C) rather than two (Configuration B) resulted in little difference to the pre-tension experienced by the square lines. There were no square interconnections in Configuration D and so has been marked NA in Table 7.1.

Again, the removal of the second seabed line in Configuration C, makes little difference to the pre-tension experienced in the diagonal lines. However, when the square interconnections are removed (Configuration D), the pre-tension in the diagonal line $TM2_{Dd}$ increases due to the increased clump weight required to achieve a similar stiffness to that of an individually moored device.

7.1.2 Regular Wave Responses

7.1.3 Seabed Lines

Similar to the motion and performance sections, the array effects on the loading characteristics will be quantified by comparing $TM3_{Ic}$ with $TM3_{Ac}$.

It can be seen from Figure 7.1 that there is very little difference between the cyclic load response of the front most mooring line $TM3_{Ic}$ with $TM3_{Ac}$. This suggests that the similar seabed mooring lines could be utilized regardless of the intended placement of the device (within an individually moored array or an isolated configuration). A reduction in the load is noticed around $f = 0.63$ Hz, particularly for $TM3_{Ac}$. This links to the reductions in performance and motion response seen in previous sections and is linked to the tank resonances that are particularly excited by the width of the array and the basin. At higher frequencies, $f = 0.65$ Hz and $f > 0.8$ Hz, $TM3_{Aa}$ can be seen to suffer from circa 16% higher loads compared to the isolated device. Linking the loads to the motion responses (Figure 6.1) of the devices, it does not appear that the surge motion contributed substantially to the cyclic loading in the front lines. As intuition suggests, the pitch and heave responses appear to be the main contributors to the cyclic loading with a matching increase in heave response for $TM3_A$ at the higher frequencies and increased loading at frequencies close to harmonics of the pitch natural frequency.

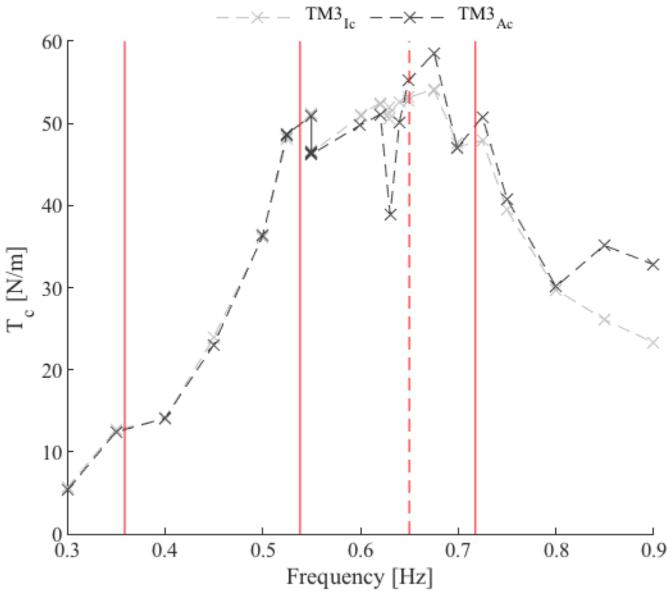

Figure 7.1: Cyclic load response to regular wave excitation of varying frequency and constant amplitude ($A = 0.025$ m) for the front most mooring lines $TM3_{Ic}$ and $TM3_{Ac}$. The solid red vertical lines indicate the second, third and fourth harmonics of the pitch natural frequency and the dashed red line indicates the heave natural frequency.

To compare the interconnected array configurations, the line suffering from the worst cyclic loading was selected for the comparison. In all cases this was found to be the front most facing line connected to $TM2$.

It can be seen from Figure 7.2 that by interconnecting the array the cyclic load is generally reduced for the front most seabed line at frequencies above $f = 0.4$ Hz. This is a highly desirable characteristic for any wave energy conversion development due to the reduced risk of fatigue failures. It should be noted here that the front-most line for each configuration is at slightly different angles apart from Configuration C and D. As described in Section 3.5, the clump weights and floats are different between each Configuration in order to match the surge displacement to that of the isolated case of less than seven device diameters, which can be seen from the motion responses in Figure 9.3 to be close. Neglecting the peaks in $TM2_{Cd}$ and $TM2_{Db}$ due to coupled surge and pitch responses discussed in Section 6.2.1, it appears that by interconnecting the array, the highest loads in the lines are noticed at the extremities of the frequency space, whereas $TM2_{Aa}$ shows the highest loads in the central regions of the frequencies tested. As expected, having two seabed lines on the corner devices (Configuration B) reduced the cyclic load with respect to the cases with only one seabed line (Configurations C and D), as the load is shared between the lines. By comparing $TM2_{Bb}$ with $TM2_{Cd}$, a large spike appears around $f = 0.525$ Hz. A similar, magnified response can be seen in from $TM2_{Db}$. Linking these spikes to the motion responses seen in Figure 6.1 and 9.3, similar spikes can be seen in all the rotational responses, as well as surge at the same frequency. To investigate this further a frequency-domain analysis of the loading time series was done. The amplitude spectrum of the load for each incident wave frequency is plotted in the three dimensional plot shown in Figure 7.3.

For visualization purposes the data from Figure 7.3 can be flattened into a two-dimensional colour plot to highlight differences in each Configuration, as shown in Figure 7.4. In order to fill the frequency space between the incident wave tests, a linear interpolation has been made by the 'pcolor' algorithm in MATLAB for visualization purposes only.

Configuration B looks to be reasonably linear, with a tension response in the line corresponding to the same incident wave frequency. When the

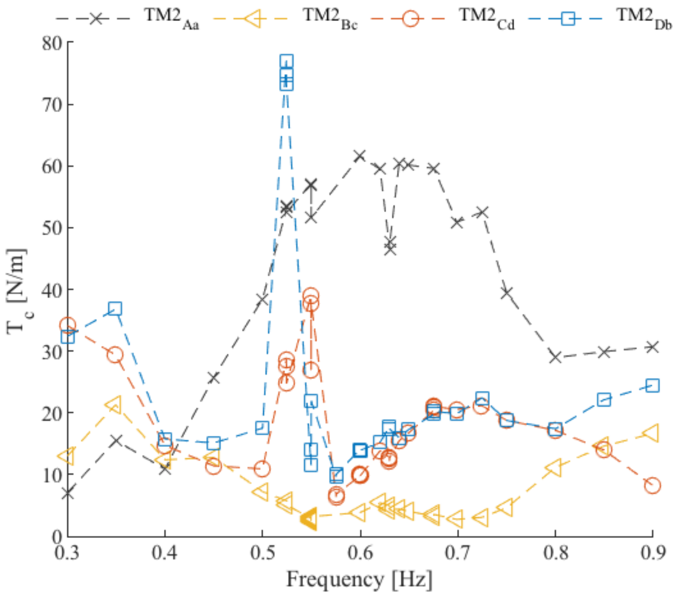

Figure 7.2: Cyclic tension response to regular wave excitation of varying frequency and constant amplitude ($A = 0.025$ m) for the front-most mooring line of the array configurations.

number of seabed lines is reduced from two to one (Configurations B to C) a second-order response around $f = 0.2$ Hz is excited with incident waves of frequency $f = 0.525$ Hz. This response is then magnified in Configuration D, suggesting that the square interconnecting lines present in Configuration C were restricting the motions responsible for this low frequency second order response. It can also be seen from Figure 7.4 that the response again appears very close to the third harmonic of the pitch natural frequency of the individually moored device. However, this is only to be used as an indication as the natural pitch frequency of the device moored in Configuration B, C and D could be very different. Linking this to the colour plots seen in Figure 6.3 of the major motions contributing to the line loads, a similar pattern can be seen in the pitch and surge response, suggesting the coupled surge and pitch

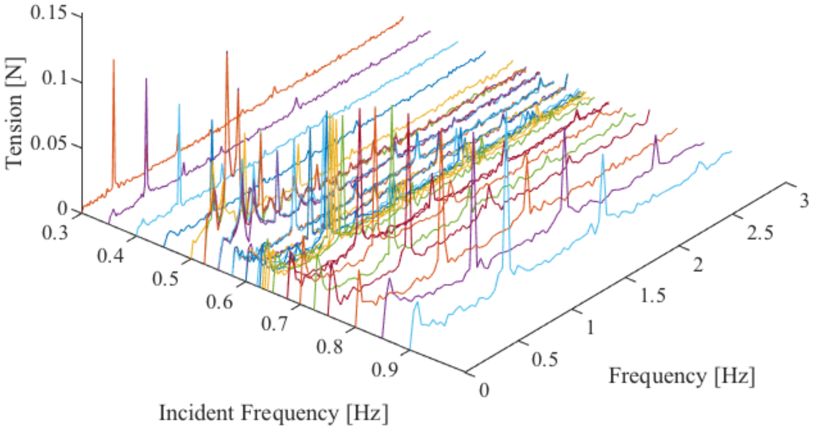

Figure 7.3: Frequency components of $TM2_{Db}$ tension response for all incident wave frequencies tested with constant amplitude ($A = 0.025$ m)

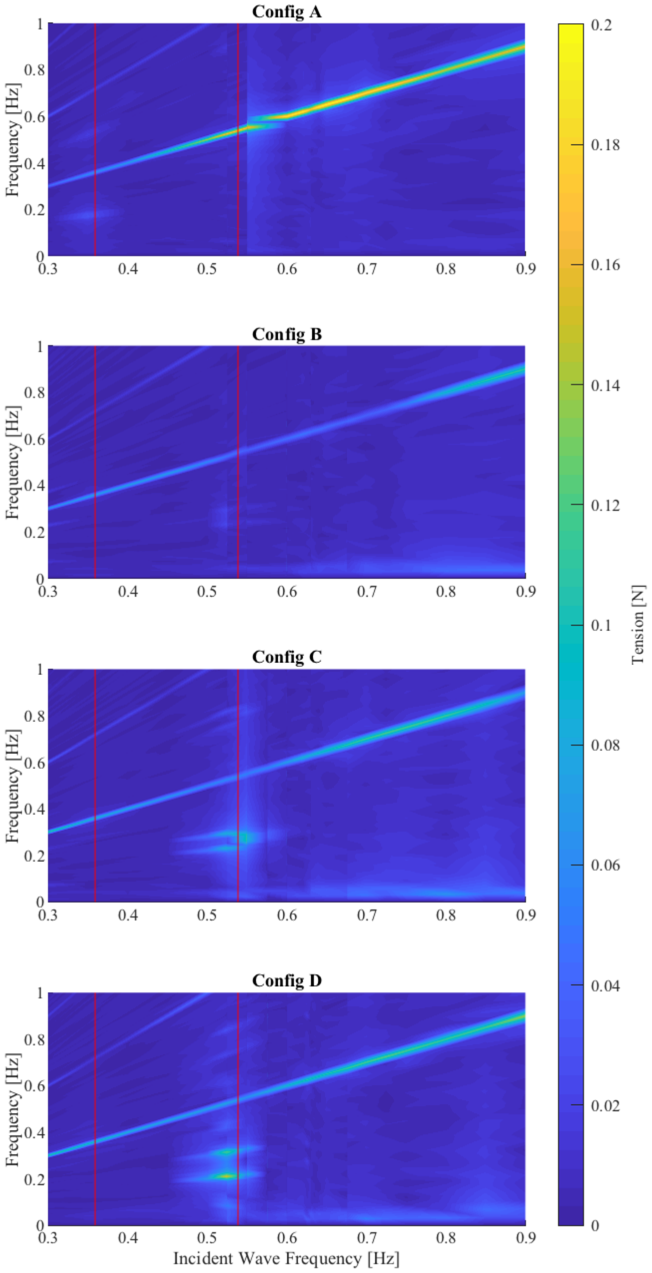

Figure 7.4: Two dimensional colour plot of the tension amplitude spectra for every incident wave frequency tested with the 2^{nd} and 3^{rd} harmonic of the pitch natural frequency indicated with vertical red lines.

motions increase the cyclic loading of the seabed lines.

Regular wave test results indicate that cyclic line loading on the seabed lines can be reduced through the interconnection of devices. Configuration B shows the most promising results with a reduction in cyclic line loading across nearly all frequencies tested. Configuration C and D indicate that if the number of interconnections is reduced beyond a threshold, second order motion responses can cause large cyclic loads at particular frequencies.

7.1.4 Square Lines

The cyclic load in the interconnecting lines is also important to the progression of the concept of interconnected arrays to ensure that the amplitude of cyclic loading is minimized during operation, negating the requirement of expensive high fatigue performance mooring lines.

Figure 7.5 presents the cyclic loading of the square interconnecting line ($TM2_{Bc}$ and $TM2_{Cc}$) with the cyclic loading of seabed line $TM2_{Aa}$. If the array were to be individually moored, the moorings would need to withstand the loading conditions experienced by Configuration A in Figure 7.5. If the cyclic loading of the interconnections is less than this, one could utilize a mooring line with reduced fatigue life properties and benefit from potential lower costs.

It can be seen from Figure 7.5 that the cyclic loading of the square interconnections is lower than that experienced by seabed lines $TM2_{Aa}$ for incident frequencies greater than $f = 0.4$ Hz. The larger loads at lower frequencies is linked to the larger surge motions experienced by the outer

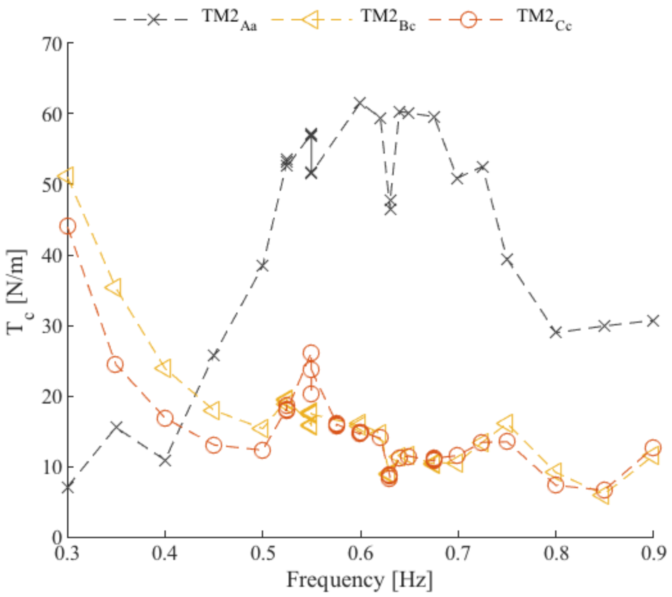

Figure 7.5: Cyclic load response to regular wave excitation for the square interconnecting line ($TM2_{Bc}$ and $TM2_{Cc}$) and for comparison, the worst case seabed line $TM2_{Aa}$.

devices as shown in Figure 6.1. The peak cyclic loads on the square lines is less than that experienced by the seabed line requirements, therefore the regular wave results suggest that moorings with lower fatigue performance could be utilized for these interconnections.

7.1.5 Diagonal Lines

A similar comparison has been carried out for the diagonal interconnecting lines ($TM3_{Bd}$, $TM2_{Cd}$ and $TM3_{Dd}$).

Figure 7.6 shows similar trends to that of the seabed lines in Figure 7.2 with Configurations C and D displaying a cyclic load spike at $f = 0.525$ Hz. This indicates that the diagonal interconnecting lines were sensitive to device surging and pitching. However, similar to the square interconnecting

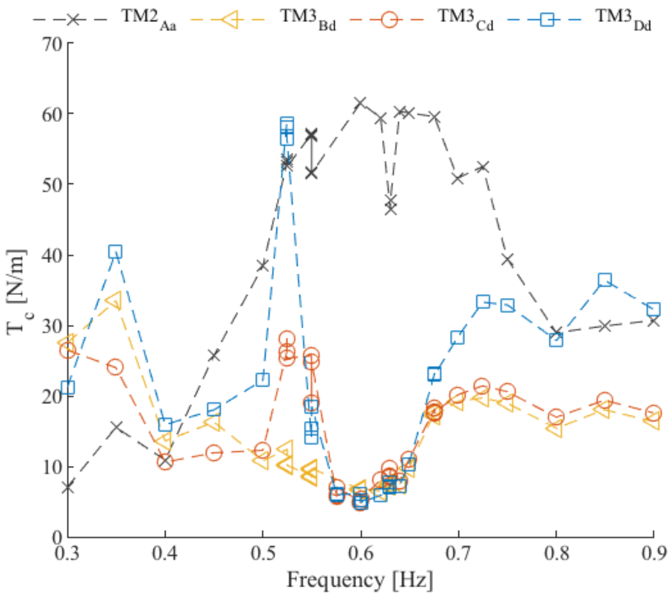

Figure 7.6: Cyclic load response to regular wave excitation for the diagonal interconnecting line (load cell 317) and for comparison, the worst case seabed line for Configuration A $TM3_{Ac}$.

lines, the peak cyclic loading, particularly for Configuration B, is less than that experienced by the seabed line required for individual mooring of the devices. Therefore, lower fatigue performance mooring lines could also be also utilized for the diagonal mooring lines.

It has been shown that when excited by regular incident waves, the interconnected arrays display the potential to reduce the static and cyclic loading in both the seabed and interconnecting lines. Configuration B has displayed the most beneficial characteristics. Next the impact of operational irregular wave conditions on the mooring line loads will be assessed.

Table 7.2: Line load *rms* divided by the empty tank wave surface elevation *rms* for $TM3_{Ic}$ and $TM3_{Ac}$. For load cell location see Figure 4.5 on page 88.

f_p **[Hz]**	**Line**	T_c **[N/m]**	**Line**	T_c **[N/m]**	**%**
0.64	$TM3_{Ic}$	44.02	$TM3_{Ac}$	43.99	<-1%
0.52	$TM3_{Ic}$	44.21	$TM3_{Ac}$	43.52	-2%

7.2 Irregular Wave Responses

7.2.1 Seabed Lines

It is important to understand the loading behaviour of each Configuration in realistic operational sea states.

It can be seen from Table 7.2 that array effects on the cyclic line loading in operational sea states is less than 2% for the cases tested. This stands as the baseline against which the effects of the interconnections can be compared against.

Comparing the array configurations, it can be seen from Figure 7.7 that similar results for the irregular tension characteristics are noticed to those seen in the regular wave tests. The interconnected arrays all display lower cyclic tension characteristics than the individually moored case, with a minimum peak fatigue load reduction of 30%. This difference is significantly greater than the array effects noticed between Configuration A and the isolated cases.

Similar to the regular wave tests, Configuration B had the lowest tensions whilst Configurations C and D behave very similarly. This is to be expected,

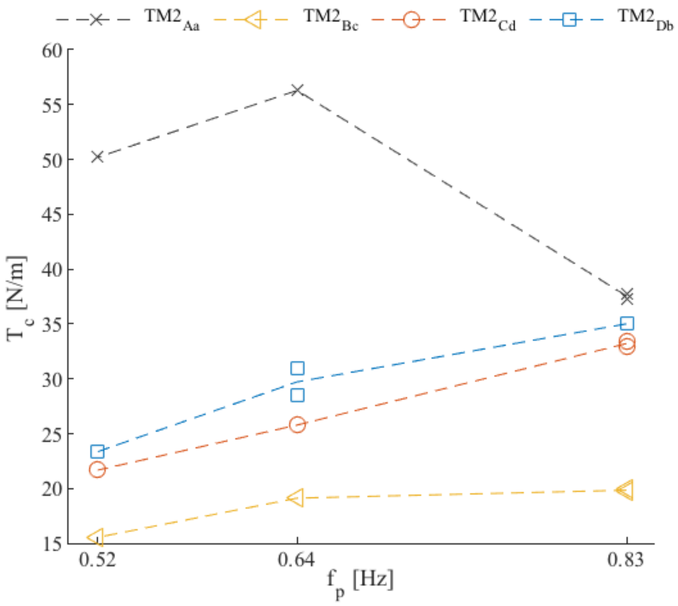

Figure 7.7: The cyclic loading of the front most seabed mooring line attached to device $TM2$ for operational sea states.

as the load is shared between two seabed lines in each corner for configuration B, whereas Configurations C and D have a single seabed line.

Configuration B has been shown to have the most beneficial seabed line pre-tension and cyclic loading characteristics. The interconnections must now be considered, to ensure the loading does not present dangerous conditions that could result in high risk during operation.

7.2.2 Square Lines

It can be seen from Table 7.1, $TM2_{Ba}$ and $TM2_{Ca}$ indicates the pre-tension of square lines is circa 23% of the pre-tension in a seabed line of an isolated device. Figure 7.8 shows the cyclic tension of the square interconnecting lines for Configurations B and C in irregular sea states.

In the seabed line analysis, it was shown that the cyclic and static loading on the seabed lines was significantly reduced by interconnecting the devices.

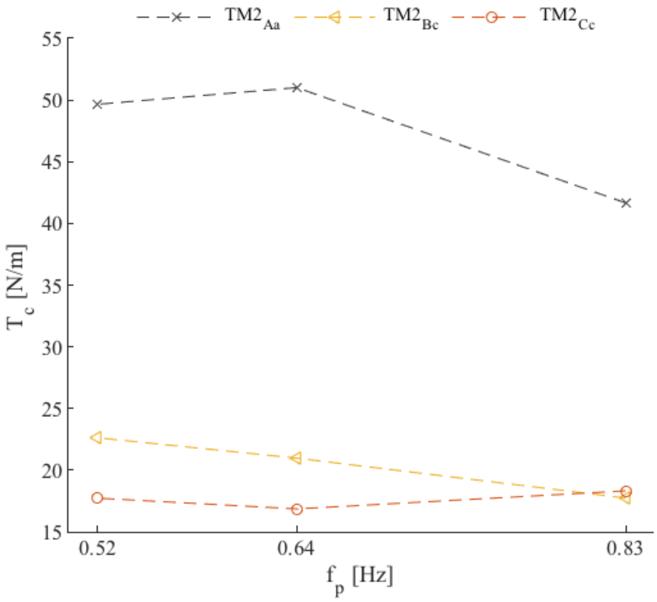

Figure 7.8: Cyclic line loading for the square interconnecting lines and for comparison, the worst case seabed line for Configuration A .

It can be seen from Figure 7.8 that the peak cyclic loading experienced by the square interconnections was 52% less than that experienced by the seabed lines of the individually moored array. Thus, the reduction in pre-tension and cyclic loading response means a reduction in the fatigue life requirements of these lines in operational sea states.

7.2.3 Diagonal Lines

It can be seen from Table 7.1, $TM3_{Bd}$,$TM3_{Cd}$ and $TM2_{Db}$ indicates the pre-tension of diagonal lines is 52%, 52%, and 71% of the pre-tension in a seabed line of an individually moored array for Configurations B,C and D respectively. Furthermore, the pre-tension of the diagonal lines in Configurations B and C is over twice that of the square interconnections.

By comparing the diagonal lines to the seabed line of $TM2_{Aa}$ in Figure 7.9, one can see a minimum of reduction of 26% in the peak cyclic loading

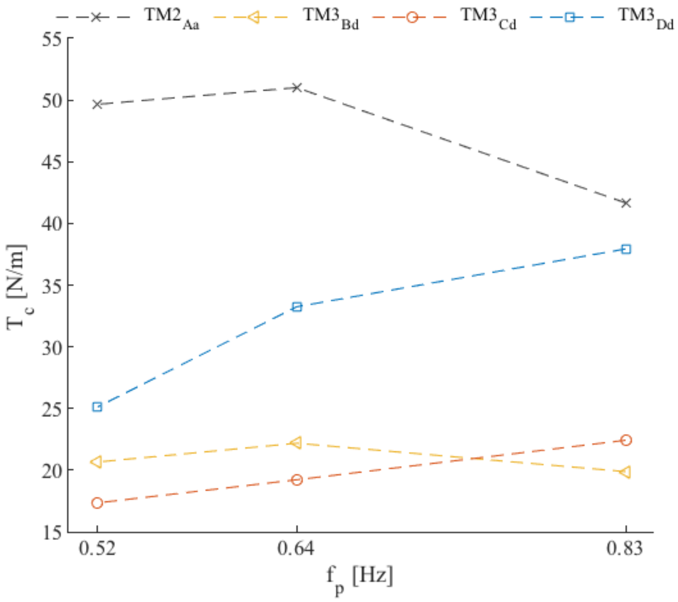

Figure 7.9: Cyclic line loading for the diagonal interconnecting lines and for comparison, the worst case seabed line for Configuration A ($TM2_{Aa}$).

conditions. Considering the static and dynamic loading, the diagonal lines will require higher strength material than the square interconnecting lines that will incur a higher cost. However, the fatigue requirements are still lower than that required for an individually moored seabed line in operational sea states.

7.3 Survivability

As described in the literature review, perceived risk has played a large part in slowing investment into the wave energy sector. The majority of this risk is associated with the system behaviour in storm conditions. At this early stage of development for interconnected arrays, survivability responses need to be addressed, therefore the motions and maximum mooring line loading were analysed.

7.3.1 Motion

Due to the large motions of the devices during 10-, 50- and 100-year return period extreme sea state testing, the measurement error on the motion data was much higher than the operational cases due to the movement of devices out of the calibrated range. This resulted in large gaps in the data acquired, particularly for devices $TM1$, $TM4$ and $TM5$. As a result, comparisons of the motion responses for only $TM3$ and $TM2$ will be made to investigate the effects of interlinking on the inner and outer devices.

It appears from Figure 7.10 that there is a significant difference between the individually moored and the interconnected cases in all degrees of freedom for both $TM3$ and $TM2$. The four-point fairlead connection on $TM3_B$, $TM3_C$ and $TM3_D$ reduced the **surge** restriction and allowed for a near 16% increase in surge between $TM3_A$ and $TM3_B$ and $TM3_C$. $TM3_B$ and $TM3_C$ appear to respond very similarly as would be expected due to the similar fairlead connection. Interestingly, the removal of the square interconnections (Configuration D) decreased the surge response across all extreme sea states for $TM3_D$ and $TM2_D$ compared to the other interconnected arrays.

The **heave** behaviour of $TM3$ across all configurations was very similar, with under 2% difference in the response in the worst-case return period of 10-years ($H_s = 0.3$ m, $f_p = 0.36$ Hz). The heave response of the interconnected cases appear to slightly increase between the 50- and 100-year return period ($H_s = 0.35$ m, $f_p = 0.33$ Hz), whereas $TM3_A$ continues to decrease. Similar to the operational cases, as the level of connectivity is reduced, the difference between the inner and outer device responses increases.

The **roll** response shows a significant divide between the inter and outer device. The magnitude of the responses are the smallest of the rotations with all the central devices showing similar trends. The interconnected configurations display lower roll responses than their individually moored counterparts.

The **pitch** results show a significant difference between the individually moored and the interconnected cases for both the inner and outer devices. The interconnections on the central device are reducing the pitch response by circa 25% across all return periods. Again, $TM3_B$ and $TM3_C$ show very similar pitch response and $TM3_D$ shows the lowest magnitude of pitch motion across the return periods. This indicates that moving from a double to a single bottom mooring line (Configuration B to C) results in little change to the behaviour of the central device in extreme states.

The **yaw** response also shows three distinct groups. $TM3_A$ shows a similar response across all return periods tested, with a magnitude smaller than that of pitch. Again, $TM3_B$ and $TM3_C$ behave very similarly with respect to yaw, again suggesting the change from a double to a single bottom line results in little difference to the response of the central device. However, removing the square interconnections reduced the yaw response on $TM3_D$.

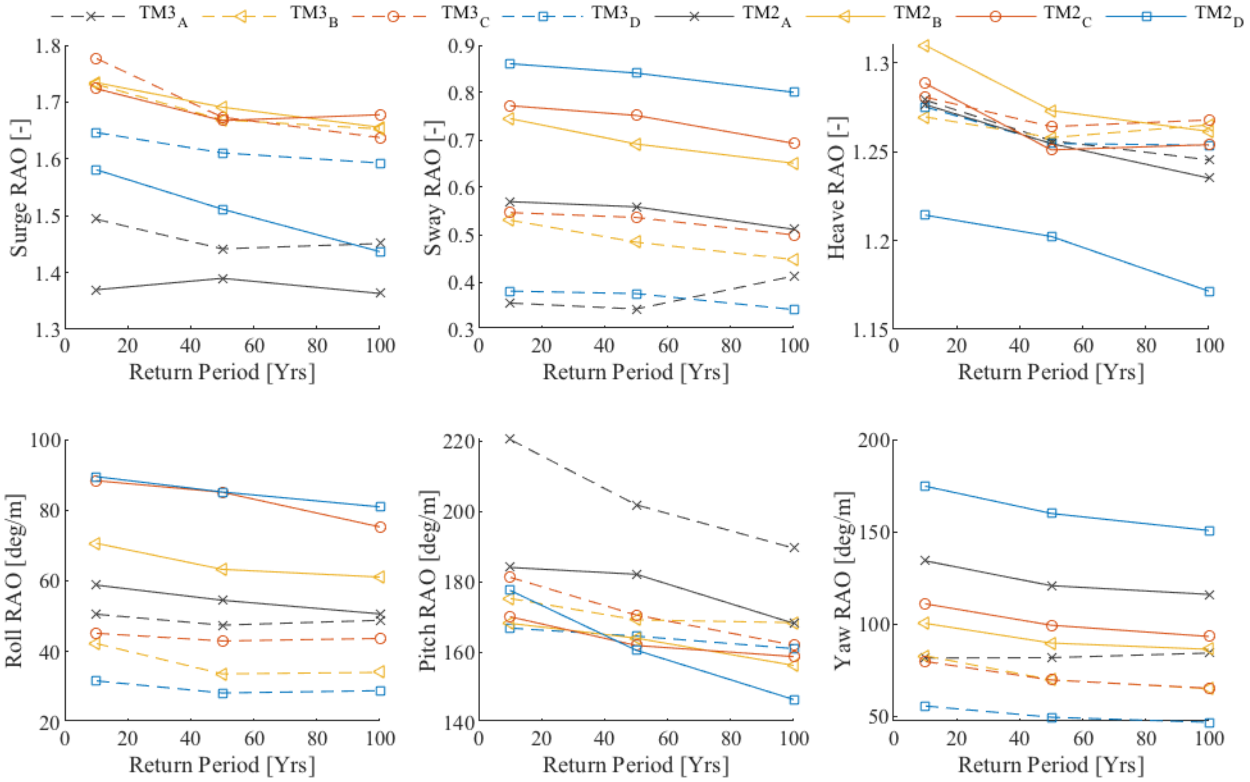

Figure 7.10: Array *rms* motion responses for extreme cases with dashed lines for $TM3$ and solid lines for device $TM2$. Motions are surge, sway, heave, roll, pitch and yaw, (a)-(f) respectively.

Table 7.3: Maximum line tension [N] for the front most seabed line of $TM3_{Ic}$ and $TM3_{Ac}$ device.

	Hs [m]	f_p [Hz]	Hs [m]	f_p [Hz]	Hs [m]	f_p [Hz]
	0.3	0.37	0.325	0.34	0.35	0.33
Return Period	10-Yr		50-Yr		100-Yr	
$TM3_{Ic}$	29.05		23.67		29.84	
$TM3_{Ac}$	26.02		23.34		23.93	
Array Effect	**-10%**		**-1%**		**-20%**	

A key aspect of the extreme state motion responses to note is the difference between the inner and outer devices in all degrees of freedom shows similar traits to that of the operational irregular sea state tests. The fewer the interconnections, the greater the difference becomes.

7.3.2 Seabed Lines

It can be seen from Table 7.3 that the array effects are reducing the line loading of $TM3_A$ across all return periods tested. The magnitude of the array effect appears to be sensitive to the return period, with destructive interference varying from 1 to 20%. The magnitude of the array effects on the line loads measured during extreme states is up to ten times greater than that noticed in the operational cases. This suggests that the array effects on the line loading conditions is non-linearly related to the incident wave conditions, although the testing of further cases would be required to confirm this.

It can be seen from Figure 7.11 that the maximum loading on the front most seabed lines $TM2_{Bc}$ and $TM2_{Cd}$ is *higher* when compared to $TM2_{Aa}$ case for lower return periods. This difference appears to attenuate slightly towards the higher return periods tested. Again, care must be taken when

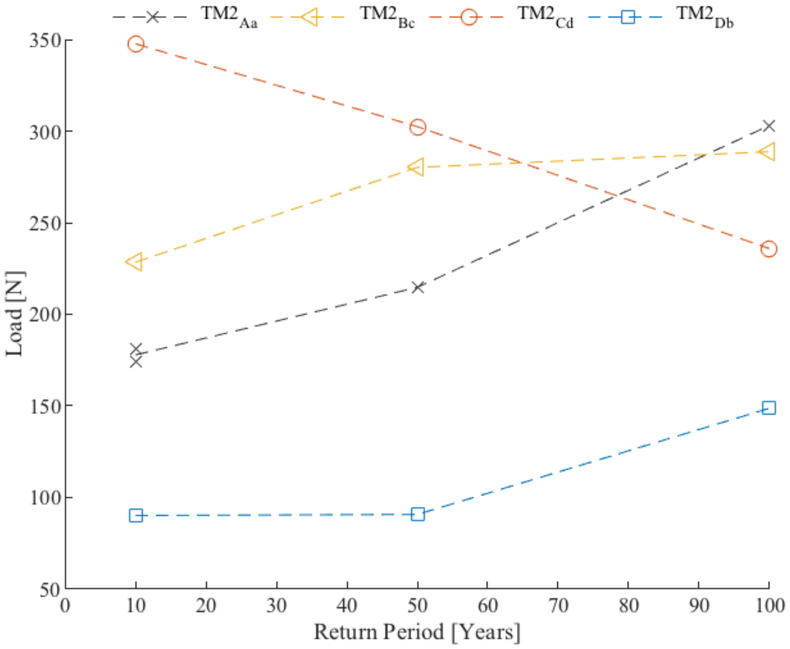

Figure 7.11: The maximum loading of the front-most seabed mooring line for the array configurations in extreme sea states of increasing return period.

interpreting these results as the line $TM2_{Aa}$ is not in the same alignment to the wave fronts as in the interconnected cases. A significant increase in the maximum line loading is noticed when the seabed connections are made with one line rather than two (Configurations B to C), resulting in a of a 53% increase at a return period of 10 years. This result is much greater than the 2% array effect measured in Table 7.3, suggesting that this result is directly related to the mooring interconnections. However, at higher return periods this situation is reversed and the line loading is reduced with the use of a single seabed line (Configuration C). Consistently across all return periods tested, the maximum line loading experienced by the seabed lines of Configuration D is less than that of the individually moored case. The peak maximum load on $TM2_{Db}$, in a 100-year return period storm, is 53% lower than that experienced by $TM2_{Aa}$. Thus, providing evidence to suggest there is a potential for utilizing a lower tensile strength mooring, however further extreme cases require testing.

Upon inspection of the solid lines in Figure 7.10, the main cause of this increase would appear to be from the characteristics of the mooring line, rather than significantly different motion responses. The only motion response that shows a significant difference between $TM2_B$ and $TM2_C$ is the roll response. Due to the angle of the roll motion, it is less likely to be the cause of the higher cyclic tensions on the seabed line.

The reduction in maximum loading noticed in $TM2_{Db}$ can be attributed to the reduction of the motion responses, particularly in surge, heave and pitch. It has been shown in the operational and regular wave cases that the line loading is sensitive to the heave response. It appears that by removing the square interconnections, the heave and surge response of $TM2_D$ is reduced compared to $TM2_C$ as seen in Figure 7.10. Although the yaw response is increased by removing the square lines, this appears to have little effect on the line loading of the connected seabed line.

The highest seabed line loading measured from all configurations is associated with the 10-year return period. To visualize the spatial distribution of the maximum loads, the 10-year return period line tensions are displayed in Figure 7.12. The thickness and colour of the line is used to indicate the magnitude of the maximum loading on each line.

It can be seen from Figure 7.12, that by interconnecting the devices in Configurations B and C, the maximal loading in the front seabed lines is increased compared to Configuration A. However, high maximum loads are also noticed in the interconnecting lines. By moving to a single seabed line, the loading is significantly increased in Configuration C. Again, the interconnections and square lines show high tensions. By increasing the clump weights and removing the square lines, as in Configuration D, the seabed line loading is reduced.

These results indicate that the interconnecting lines may be susceptible to large snatch loading in extreme conditions.

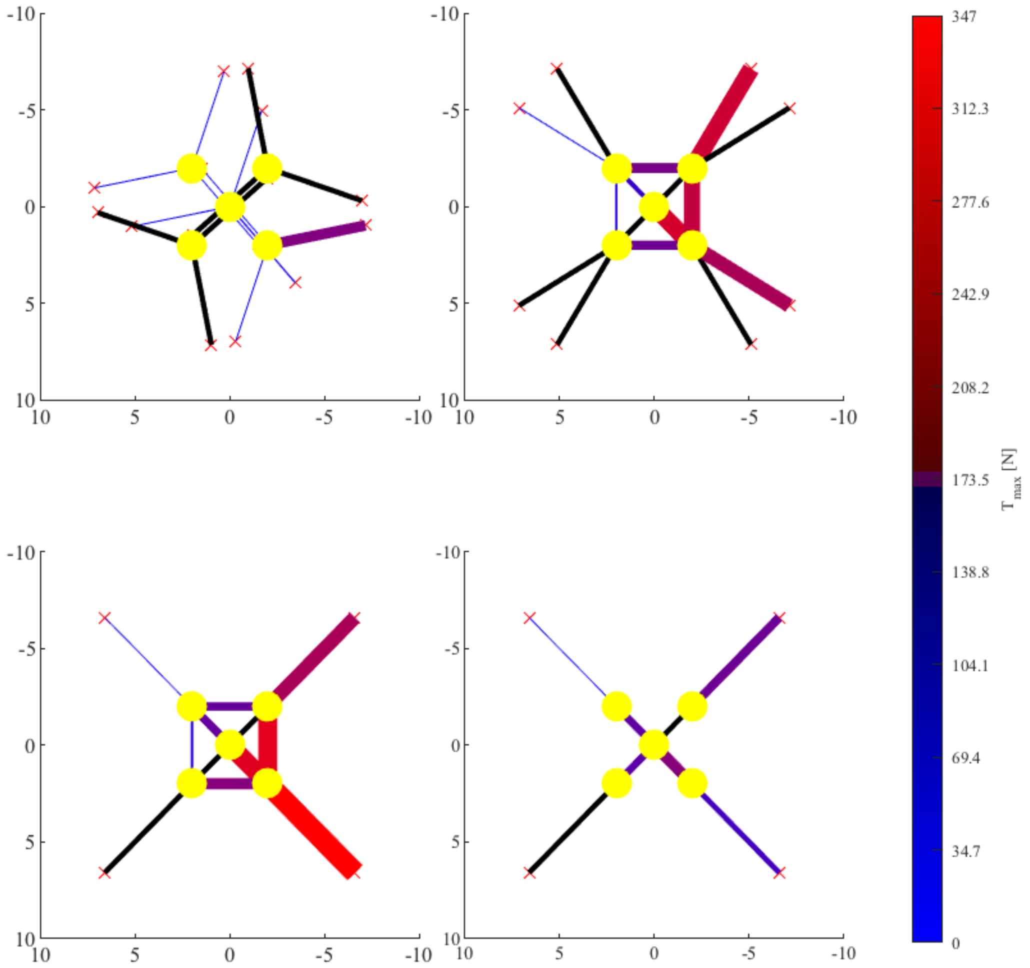

Figure 7.12: Maximum line load for the survivability case with a return period of 10-years for all Configurations, with waves propagating from right to left. The colour and line thickness are proportional to the maximum loading experienced. Black lines are non-instrumented lines.

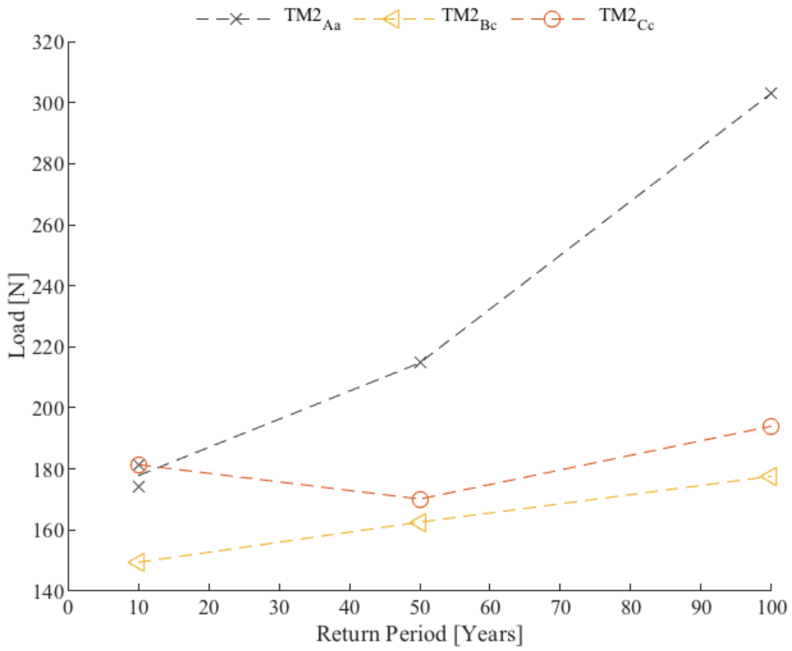

Figure 7.13: Maximum loading for the square interconnecting lines and for comparison, the worst case seabed line for Configuration A in extreme sea state tests

7.3.3 Square Lines

The maximum loading on the square interconnections are summarized in Figure 7.13. Figure 7.13 shows the maximum loading of the square interconnections to be lower than that of the maximum loading of the front most seabed line of Configuration A across all return periods tested. Furthermore, the gentle gradient of Configuration B and C suggests that the loading in the square lines is not as sensitive to the return period as the individually moored case.

7.3.4 Diagonal Lines

The maximal loading on the diagonal interconnections are summarized in Figure 7.14. The operational cases indicate the cyclic loading of diagonal lines to be less than that of the seabed line in Configuration A. The survivability cases indicate that Configuration B and C suffer from circa 60% higher extreme line loading in the diagonal interconnections at lower return periods. At higher return periods, Configurations B and C appear to display similar loading conditions to that experienced by Configuration A. Comparable to that seen in the seabed line loading, Configuration D displays similar maximal loading to that of the individually moored case at lower return periods, where other interconnected arrays suffered, and reduced loading at higher return periods. The reduction in heave and pitch noticed in Figure 7.10 significantly reduced the loading on the diagonal interconnections.

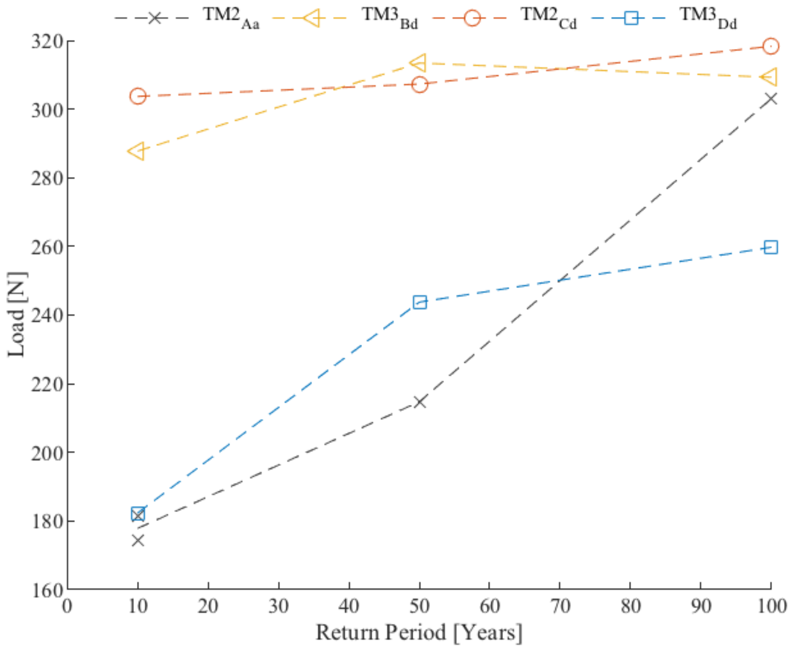

Figure 7.14: Maximum loading for the diagonal interconnecting line and for comparison, the worst case seabed line for configuration A in extreme sea state tests

To summarize the findings of the line loading in extreme sea states, interconnecting of devices is possible, however results show higher maximal loading in some interconnected cases compared to a similar individually moored array. Results particularly highlighted the diagonal interconnecting lines as highly loaded components. This indicates that interconnecting mooring lines need to be specifically designed to their intended location within an array. Operational conditions indicate enhanced fatigue properties for the interconnected arrays. However, the survivability cases indicate that in storm conditions, the interconnecting lines may suffer from snatch loads and so would require a higher tensile strength mooring material.

7.4 Operational Line Loading

Line loading conditions has a direct implication on the mooring costs. The higher the mooring loads, the higher strength mooring lines will be required and thus, higher the cost.

In accordance with DNV mooring guidelines [84], the mooring system should be designed to withstand a 100-year return period extreme sea state. It was shown in Section 7.3 that the maximum loading experienced by the seabed lines was reduced in some of the interconnecting cases. Thus, one could expect a corresponding cost reduction. However, Configuration C showed a higher maximum load compared to an individually moored device, indicating that this cost saving cannot be expected for all interconnected designs. This is further shown in the diagonal interconnections, where Configuration D was shown to experience a lower maximum load than cases where there were other interconnecting lines (Configuration B and C). It is therefore likely, that some interconnections would require a higher cost line than than the seabed mooring lines required for an individually moored array.

It can be seen from Section 7.2.1 that the cyclic line loading in the operational cases is significantly lower for both the seabed and interconnecting lines compared to the individually moored case. The effect of a 50% decreased cyclic loading and lower pre-tension on the service life of the components can be seen in the SN curve shown in Figure 7.15. The figure shows a typical SN curve for a polymer mooring line [85], where R is the ratio of the cyclic loading to the ultimate tensile strength and N_c is the number of cycles to failure. To approximate the effect of the 51% lower pre-tension, similar to that of the diagonal interconnections compared to the seabed lines of Configuration A, the SN curve for the nominal mean stress line (σ_N) has been plotted for the original pre-tension (blue) and 51% lower (red), as shown by the red solid line. Considering both the reduction in pre-tension and the reduced cyclic loading, a significant increase in service life is noticed by comparing the blue and red dashed lines (considering the same mooring material is used for both situations).

Experimental results from extreme sea states indicate that interconnected arrays show the potential for the use of lower strength mooring materials in the seabed lines of Configuration B and D. In operational sea states these configurations also shows a reduction in cyclic fatigue loading compared to

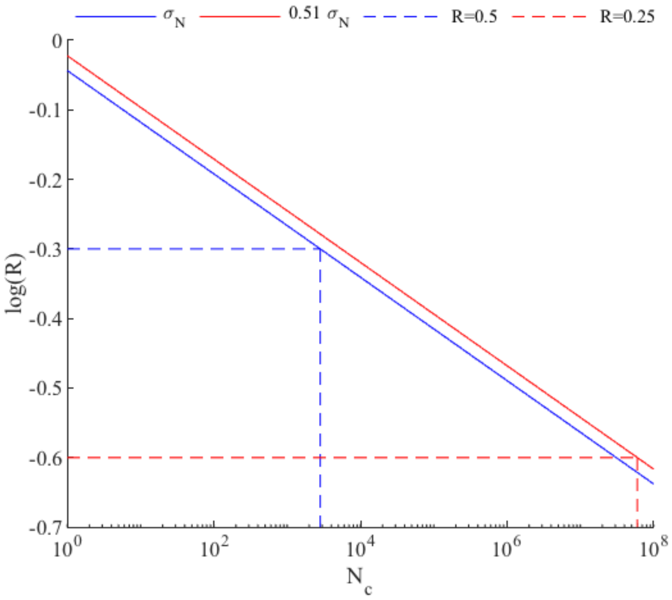

Figure 7.15: The ratio of cyclic stress to tensile strength of a polymer mooring line plotted against cycles to failure [85].

that of an individually moored array, resulting in an extended service life of the mooring lines. This is not the case for the interconnections, where Configuration B would require higher strength mooring lines due to the higher extreme loads experienced compared to the individually moored case. This indicates that loading conditions of interconnected arrays is design specific and not necessarily proportional to the number of interconnections. However, for configurations where an increased service life is attainable, there are cost implications for the energy extraction yield, asset depreciation, site lease agreements, insurance and investment risk levels. These complex interactions require costs modelling which is beyond the scope of this research.

For the cases examined as part of this study, the seabed connections are hybrid catenary lines. As a result, there should never be any loading on the anchor points. This is of great importance to the cost considerations. If the seabed lines were of a taught nature, the higher loading noticed in Figure 7.11 for the interconnected arrays, would result in the need for heavier/more expensive anchorage that could negate prospective cost savings. However, with a catenary design, this is not the case. Providing the chain section of the line is designed in a way to provide the maximum horizontal restoring force required and is never in a taught state, cost savings associated with a reduction in anchor numbers can be realised.

7.5 Conclusion

Hydrodynamic array interactions were shown to account for a 16% increase in cyclic fatigue loading of the seabed lines. Results from interconnected array testing demonstrates the possibility of reducing the fatigue loading of both the seabed and interconnected moorings, although configurations with lower levels of connectivity suffered due to coupled pitch and surge motion responses. In operational sea states the peak fatigue load was reduced by 30% in the seabed lines and 26% for interconnections. In extreme conditions, the peak loading was shown to be dependent on the interconnecting design. Configuration C showed a 17% increase in peak load, whilst Configuration D displayed a 53% decrease, hence demonstrating further potential for interconnected mooring systems.

8

Conclusions

In this chapter the key findings of this research are summarized with reference to the motion responses, performance, mooring line loading conditions and the limitations of the presented analysis. The chapter concludes with further work required to progress the concept of interconnected WEC arrays.

8.1 Conclusions

This research has shown that interconnected arrays have the potential to improve the financial viability of a wave farm, not only through the reduction in the number of seabed anchors required, but also through improved performance and reduced peak mooring line loading.

The hydrodynamic array effects were first quantified in order to isolate the effects of the mooring interconnections alone. Array effects on the heave motion response of the central device accounted for a 10% increase when the device was located within an individually moored array ($TM3_A$). When devices were interconnected, a significant shift in the natural frequency was found with both decay test and RAO results. This natural frequency shift resulted in a beneficial phase difference between the OWC water column and the heave response of the device, thus resulting in a higher power output. Interconnected arrays were shown to yield a 211% increase in peak performance compared to the identical array configuring individually moored to the seabed. Furthermore, all interconnected arrays showed the same performance enhancements within the bounds of measurement uncertainty, regardless of the level of interconnectivity. It was noticed that the homogeneity of the power distribution was related to the level of connectivity, with the power attenuation between the front and rear of the arrays being inversely proportional to level of connectivity. To contextualize these findings a linear approach was adopted to predict the energy yield of each array when exposed to the wave climate of Leixões, Portugal. The methodology was tested by predicting physically tested irregular sea states and was found to be over predicting the energy yield by up to 12% in some cases. However, results indicated an increase in annual energy yield of 75% through the use of interconnected mooring systems. This result being significantly greater than the errors associated with the linear assumptions of the methodology indicates the true potential of interconnected arrays.

Mooring line loading for both seabed and interconnecting lines were analysed separately with regard to operational irregular sea states, as well as in extreme conditions. Hydrodynamic array interactions were shown to cause a 16% increase in the cyclic loading of the seabed lines, contributing to increased fatigue damage and thus a shorter component service life. For most interconnected arrays, the peak cyclic load was shown to decrease compared to the individually moored configuration. For configurations with lower levels of interconnectivity, spikes in cyclic load at particular frequencies were noticed. This was attributed to a coupled pitch and surge motion response during regular wave tests. When multiple frequencies were present in operational sea state testing, this phenomenon was not present, resulting in a minimum reduction of peak fatigue loading of 30% for seabed lines and 26% for interconnecting lines. This suggests that there is further potential for cost saving in the extended fatigue life of the interconnected moorings in asset value at the end of the systems life, providing similar mooring materials are used to that of an individually moored concept.

Arrays were tested in 10-,50- and 100-year return period extreme sea states to analyse the maximum peak load experienced by the mooring lines. DNV guidelines state that moorings should be designed to withstand a return period sea state of 100 years. Thus the cost of the mooring line required will be proportional to this maximum load experienced in these tests. It was shown that in some configurations (Configuration C) the peak load experienced by the seabed lines was increased by 17%. However, Configuration D, which had the fewest number of interconnections, displayed a 53% decrease in peak loading for the 100-year return period storm. A 7% increase in peak load was measured for the interconnecting lines of Configurations B and C, although Configuration D again displayed a 17% decrease. This indicates interconnected mooring systems can also reduce peak loading compared to individually moored arrays, thus offering further potential for cost savings.

8.2 Further Work

To progress this research further, the mooring line loading has been highlighted as an area of interest. Combining the information regarding fatigue loading in operational sea states and the peak loads in extreme conditions, further work is required to quantify this effect on component life. Furthermore, due to time restraints only a small number of operational and extreme sea states were tested. In order to understand the implications of these findings in a greater variety of operating states further tests should be carried out. With this knowledge, a cost model can be built to understand the true implications of the exact mooring line requirements, service life and operation and maintenance schedules required for interconnected arrays. This cost model would be unique to interconnected arrays, considering issues such as accessing interior devices within the array, the requirement of spare devices in the case of a device removal and environmental impacts, which would all effect the LCOE of the concept.

To further understand the interaction between the basin and the array and implications for open ocean deployment, repeats of the experiments with the devices shifted off centre could offer insight to the behaviour that has been measured as part of this thesis. The devices being off centre may not excite the basin resonance in the same way that was shown in these experiments and the associated numerical model.

The interconnected array characteristics in this research have been calculated with all devices being in an operational state. In the case where a device has become damaged, a 'shutdown' mode, where the PTO is completely closed, has been researched [18] and found to have serious implications on device behaviour. Within, an independently moored array, this would alter the local wave field and subsequently, the performance of the other devices. Within an interconnected array, the impact of devices in 'shutdown' mode could have greater implications on the performance and line loading of the remaining devices and requires further testing.

Significant performance enhancements have been demonstrated for OWC type converters due to beneficial phase shifts of the devices in interconnected configurations. However, this may not be the case for other types of converter. Repeating the experiments with other device types would provide information with regard to the level of device specificity the results of this thesis hold.

Finally, directionality of the incident wave field is of vital importance in the evaluation of wave energy converter concepts. The interconnected array performance and line loading conditions with regard to incident wave angle require to be fully understood to ensure that directionality does not result in detrimental characteristics. This work would also refine the predicted energy extraction potentials and improve the component fatigue life estimations.

Bibliography

[1] M. E. McCormick, *Ocean wave energy conversion.* Courier Corporation, 2013.

[2] J. F. Chozas, *Technical and non-technical issues towards the commercialisation of wave energy converters.* River Publishers, 2013.

[3] A. Clément, P. McCullen, A. Falcão, A. Fiorentino, F. Gardner, K. Hammarlund, G. Lemonis, T. Lewis, K. Nielsen, S. Petroncini *et al.*, "Wave energy in europe: current status and perspectives," *Renewable and sustainable energy reviews*, vol. 6, no. 5, pp. 405–431, 2002.

[4] K. Gunn and C. Stock-Williams, "Quantifying the global wave power resource," *Renewable Energy*, vol. 44, pp. 296–304, 2012.

[5] IEA, *World Energy Balances: Overview*, 2018.

[6] P. Gadonneix, F. B. de Castro, N. F. de Medeiros, R. Drouin, C. Jain, Y. D. Kim, J. Ferioli, M.-J. Nadeau, A. Sambo, J. Teyssen *et al.*, "2010 survey of energy resources," Tech. Rep., 2010.

[7] House of Commons., *The future of marine renewables in the UK: Government response to the Committees eleventh report of session 2010-12: first special report of session 2012-12.* Stationery Office, 2012.

[8] N. Guillou and G. Chapalain, "Annual and seasonal variabilities in the performances of wave energy converters," *Energy*, vol. 165, pp. 812–823, 2018.

[9] B. Child and V. Venugopal, "Optimal configurations of wave energy device arrays," *Ocean Engineering*, vol. 37, no. 16, pp. 1402–1417, 2010.

[10] T. Stalled, "Research: Wecwakes," Jan 2013. [Online]. Available: http://universitylivinglab.org/projects/wecwakes

[11] V. Stratigaki, "Experimental study and numerical modelling of intra-array interactions and extra-array effects of wave energy converter arrays," Ph.D. dissertation, Ghent University, 2014.

[12] V. Stratigaki, P. Troch, D. Forehand, T. Stallard, J. P. Kofoed, M. Folley, M. Benoit, A. Babarit, D. Gallach Sanchez, L. De Bosscher *et al.*, "Physical modelling of large wave energy converter arrays in a large-scale wave basin: the wecwakes project," in *Hydralab IV Closing Conference 2014*, 2014, pp. 1–11.

[13] L. Henry, J. Bridge, K. Satahoo, H. Miller, B. Lougheide, and D. Garbutt, "Equator-friendly ocean wave energy conversion," in *Proceedings of the World Congress on Engineering*, vol. 2, 2016.

[14] V. Krivtsov and B. Linfoot, "Physical model investigation of mooring loads in arrays of wave energy converters," in *Proc. 1st European Congress of the IAHR, Edinburgh, Scotland, UK*, 2010.

[15] B. Borgarino, A. Babarit, and P. Ferrant, "Impact of wave interactions effects on energy absorption in large arrays of wave energy converters," *Ocean Engineering*, vol. 41, pp. 79 – 88, 2012. [Online]. Available: http://www.sciencedirect.com/science/article/pii/S0029801812000054

[16] A. Babarit, B. Borgarino, P. Ferrant, and A. Clément, "Assessment of the influence of the distance between two wave energy converters on energy production," *IET renewable power generation*, vol. 4, no. 6, pp. 592–601, 2010.

[17] J. Engström, M. Eriksson, M. Göteman, J. Isberg, and M. Leijon, "Performance of large arrays of point absorbing direct-driven wave energy converters," *Journal of Applied Physics*, vol. 114, no. 20, p. 204502, 2013.

[18] Network, Marine Renewables Infrastructure, "Dynamics of oscillating water column spar-buoy wave energy converters deployed in array and its survivability in extreme conditions," 2015.

[19] F. C. da Fonseca, R. Gomes, J. Henriques, L. Gato, and A. Falcao, "Model testing of an oscillating water column spar-buoy wave energy converter isolated and in array: Motions and mooring forces," *Energy*, vol. 112, pp. 1207–1218, 2016.

[20] V. Krivtsov and B. Linfoot, "Basin testing of wave energy converters in trondheim: investigation of mooring loads and implications for wider

research," *Journal of Marine Science and Engineering*, vol. 2, no. 2, pp. 326–335, 2014.

[21] I. G. Ashton, L. Johanning, and B. Linfoot, "Measurement of the effect of power absorption in the lee of a wave energy converter," in *ASME 2009 28th International Conference on Ocean, Offshore and Arctic Engineering.* American Society of Mechanical Engineers, 2009, pp. 1021–1030.

[22] S. Nallayarasu and P. S. Prasad, "Hydrodynamic response of spar and semi-submersible interlinked by a rigid yoke–part i: regular waves," *Ships and Offshore Structures*, vol. 7, no. 3, pp. 297–309, 2012.

[23] J. DeCew, K. Baldwin, B. Celikkol, M. Chambers, D. W. Fredriksson, J. Irish, R. Langan, G. Rice, M. R. Swift, and I. Tsukrov, "Assessment of a submerged grid mooring in the gulf of maine," in *OCEANS 2010.* IEEE, 2010, pp. 1–9.

[24] G. Rice, "Investigation of a submerged four-bay mooring system for aquaculture," Master's thesis, The school of the thesis, The University of New Hampshire, Durham, 2006.

[25] P. C. Vicente, F. d. O. António, L. M. Gato, and P. A. Justino, "Dynamics of arrays of floating point-absorber wave energy converters with inter-body and bottom slack-mooring connections," *Applied Ocean Research*, vol. 31, no. 4, pp. 267–281, 2009.

[26] S. Yang and J. Ringsberg, *Advances in Renewable Energies Offshore: Proceedings of the 3rd International Conference on Renewable Energies Offshore (RENEW 2018): Analysis of interaction effects between WECs in four types of wave farms, October 8-10, 2018, Lisbon, Portugal.* CRC Press, 2018.

[27] D. W. Fredriksson, J. DeCew, M. R. Swift, I. Tsukrov, M. D. Chambers, and B. Celikkol, "The design and analysis of a four-cage grid mooring for open ocean aquaculture," *Aquacultural engineering*, vol. 32, no. 1, pp. 77–94, 2004.

[28] K. Collins, D. Greaves, G. Iglesias, M. Hann, B. Howey, and V. Harnois, "D6.1 - analysis of different potential configurations of non-rigid inter-moored devices," WETFEET, Deliverable 6.1, Apr 2016.

[29] G. Chang, C. A. Jones, J. D. Roberts, and V. S. Neary, "A comprehensive evaluation of factors affecting the levelized

cost of wave energy conversion projects," *Renewable Energy,* vol. 127, pp. 344 – 354, 2018. [Online]. Available: http://www.sciencedirect.com/science/article/pii/S0960148118304798

[30] B. Teillant, R. Costello, J. Weber, and J. Ringwood, "Productivity and economic assessment of wave energy projects through operational simulations," *Renewable Energy,* vol. 48, pp. 220 – 230, 2012. [Online]. Available: http://www.sciencedirect.com/science/article/pii/S096014811200314X

[31] L. Martinelli, P. Ruol, and G. Cortellazzo, "On mooring design of wave energy converters: The seabreath application," *Coastal Engineering Proceedings*, 2012.

[32] R. E. Harris, L. Johanning, and J. Wolfram, "Mooring systems for wave energy converters: A review of design issues and choices," *Marec2004*, 2004.

[33] A. Vickers and L. Johanning, "Comparison of damping properties for three different mooring," in *Proceedings of the 8th European Wave and Tidal Energy Conference, Uppsala, Sweden*, 2009, pp. 7–10.

[34] W. Sheng, T. Lewis, R. Alcorn, L. Johanning, and P. Kirrane, "Experimental investigation of hydrodynamic characteristics of a moored floating wec," in *Proceedings of 3rd International Conference on Ocean Energy*, 2010.

[35] H. E. Jones, "Marine buoy," Jan. 30 1990, uS Patent 4,896,620.

[36] P. A. Lynn, *Electricity from wave and tide: an introduction to marine energy.* John Wiley & Sons, 2013.

[37] Seabased Wave Power. (2018) The technology. [Online]. Available: https://www.seabased.com/the-technology

[38] R. Henderson, "Design, simulation, and testing of a novel hydraulic power take-off system for the pelamis wave energy converter," *Renewable energy*, vol. 31, no. 2, pp. 271–283, 2006.

[39] A. Henry, K. Doherty, L. Cameron, T. Whittaker, and R. Doherty, "Advances in the design of the oyster wave energy converter," in *RINA Marine and Offshore Energy Conference*, 2010.

[40] R. Curran, T. Stewart, and T. Whittaker, "Design synthesis of oscillating water column wave energy converters: performance matching," *Proceedings of the Institution of Mechanical Engineers, Part A: Journal of Power and Energy*, vol. 211, no. 6, pp. 489–505, 1997.

[41] T. Heath, "A review of oscillating water columns," *Phil. Trans. R. Soc. A*, vol. 370, no. 1959, pp. 235–245, 2012.

[42] Wave Dragon. (2018). [Online]. Available: http://www.wavedragon.net/

[43] D. Valério, P. Beirão, and J. S. da Costa, "Optimisation of wave energy extraction with the archimedes wave swing," *Ocean Engineering*, vol. 34, no. 17-18, pp. 2330–2344, 2007.

[44] A. Falcão, J. Henriques, R. Gomes, P. Vicente, F. Fonseca, J. Varandas, and L. Trigo, "Dynamics of oscillating water column spar-buoy wave energy converters deployed in array and its survivability in extreme conditions," Marinet, Infrastructure Report 01, 09 2015.

[45] J. Falnes, *Ocean Waves and Oscillating Systems: Linear Interactions Including Wave-Energy Extraction.* Cambridge University Press, 2002. [Online]. Available: https://books.google.co.uk/books?id=bl1FyQjCklgC

[46] G. P. Thomas and D. V. Evans, "Arrays of three-dimensional wave-energy absorbers," *Journal of Fluid Mechanics*, vol. 108, p. 67âĂŞ88, 1981.

[47] A. F. Falcão, "Modelling of wave energy conversion," *Instituto Superior Técnico, Universidade Técnica de Lisboa*, 2014.

[48] A. Falcão, "The shoreline owc wave power plant at the azores," in *Fourth European Wave Energy Conference, Aalborg, Denmark*, 2000, pp. 4–6.

[49] T. Setoguchi and M. Takao, "Current status of self rectifying air turbines for wave energy conversion," *Energy conversion and management*, vol. 47, no. 15-16, pp. 2382–2396, 2006.

[50] M. Takao and T. Setoguchi, "Air turbines for wave energy conversion," *International Journal of Rotating Machinery*, vol. 2012, 2012.

[51] M. Folley, *Numerical modelling of wave energy converters: State-of-the-art techniques for single devices and arrays.* Academic Press, 2016.

[52] A. F. Falcão, J. C. Henriques, and J. J. Candido, “Dynamics and optimization of the owc spar buoy wave energy converter,” *Renewable Energy*, vol. 48, pp. 369 – 381, 2012. [Online]. Available: http://www.sciencedirect.com/science/article/pii/S0960148112003229

[53] R. Gomes, J. Henriques, L. Gato, and A. d. O. Falcão, “Hydrodynamic optimization of an axisymmetric floating oscillating water column for wave energy conversion,” *Renewable Energy*, vol. 44, pp. 328–339, 2012.

[54] A. Babarit, J. Hals, M. Muliawan, A. Kurniawan, T. Moan, and J. Krokstad, “Numerical benchmarking study of a selection of wave energy converters,” *Renewable Energy*, vol. 41, pp. 44 – 63, 2012. [Online]. Available: http://www.sciencedirect.com/science/article/pii/S0960148111005672

[55] L. Johanning, G. H. Smith, and J. Wolfram, “Measurements of static and dynamic mooring line damping and their importance for floating wec devices,” *Ocean Engineering*, vol. 34, no. 14, pp. 1918 – 1934, 2007. [Online]. Available: http://www.sciencedirect.com/science/article/pii/S0029801807001126

[56] V. Harnois, S. Weller, L. Johanning, P. Thies, M. Le Boulluec, D. Le Roux, V. SoulÃČÂľ, and J. Ohana, “Numerical model validation for mooring systems: Method and application for wave energy converters,” vol. 75, pp. 869–887, 03 2015.

[57] M. Penalba, T. Kelly, and J. V. Ringwood, “Using nemoh for modelling wave energy converters: a comparative study with wamit,” *Centre for Ocean Energy Research (COER), Maynooth University, Co. Kildare, Ireland*, 2017.

[58] M. Hall, “Moordyn user guide,” *Department of Mechanical Engineering, University of Maine: Orono, ME, USA*, 2015.

[59] M. Lawson, Y.-H. Yu, K. Ruehl, C. Michelen *et al.*, “Development and demonstration of the wec-sim wave energy converter simulation tool,” 2014.

[60] (2015, Jan) Theory. [Online]. Available: https://wec-sim.github.io/WEC-Sim/theory.html

[61] K. Collins, P. Arber, and B. Howey, “D6.3 - report on the 1:40 physical models,” WETFEET, Deliverable 6.4, Dec 2017.

[62] S. A. Hughes, *Physical models and laboratory techniques in coastal engineering.* World Scientific, 1993, vol. 7.

[63] J. D. C. M. Ferreira, "Experimental study of the dynamic instability in the oscillating water column spar buoy," Masters Thesis, IST, 07 2016.

[64] P. F. Hinrichsen, "Bifilar suspension measurement of boat inertia parameters," *Journal of Sailboat Technology*, vol. 1, pp. 1–37, 2014.

[65] A. Sarmento, "Wave flume experiments on two-dimensional oscillating water column wave energy devices," *Experiments in fluids*, vol. 12, no. 4-5, pp. 286–292, 1992.

[66] F. Thíebaut, R. Pascal, and A. Andreu, "Investigation into the calibration of orifices used in owc tank testing," in *11th European Wave and Tidal Energy Conference (EWTEC), September 6e11, Nantes, France*, 2015.

[67] W. Sheng, F. Thiebaut, M. Babuchon, J. Brooks, A. Lewis, and R. Alcorn, "Investigation to air compressibility of oscillating water column wave energy converters," in *ASME 2013 32nd International Conference on Ocean, Offshore and Arctic Engineering.* American Society of Mechanical Engineers, 2013, pp. V008T09A005–V008T09A005.

[68] T. Verbrugghe, V. Stratigaki, P. Troch, R. Rabussier, and A. Kortenhaus, "A comparison study of a generic coupling methodology for modeling wake effects of wave energy converter arrays," *Energies*, vol. 10, no. 11, p. 1697, 2017.

[69] U. A. Korde and J. Ringwood, *Hydrodynamic control of wave energy devices.* Cambridge University Press, 2016.

[70] S. Astariz and G. Iglesias, "The economics of wave energy: A review," *Renewable and Sustainable Energy Reviews*, vol. 45, pp. 397–408, 2015.

[71] J. W. Ringsberg, H. Jansson, S.-H. Yang, M. Örgård, and E. Johnson, "Comparison of mooring solutions and array systems for point absorbing wave energy devices," in *ASME 2018 37th International Conference on Ocean, Offshore and Arctic Engineering.* American Society of Mechanical Engineers, 2018, pp. V11AT12A037–V11AT12A037.

[72] B. Cahill and T. Lewis, "Wave period ratios and the calculation of wave power," in *Proceedings of the 2nd Marine Energy Technology Symposium*, vol. 10, 2014.

[73] P. Lamont-Kane, M. Folley, and T. Whittaker, "Investigating uncertainties in physical testing of wave energy converter arrays," in *Proceedings, 10th European Wave and Tidal Energy Conference (EWTEC 2013), Aalborg, Denmark*, 2013.

[74] J. Orphin, J.-R. Nader, I. Penesis, D. Howe *et al.*, "Experimental uncertainty analysis of an owc wave energy converter," in *European Wave and Tidal Energy Conference, Cork, Ireland*, 2017.

[75] M. McCormick, *Ocean Wave Energy Conversion*, ser. Dover Civil and Mechanical Engineering Series. Dover Publications, 2007. [Online]. Available: https://books.google.co.uk/books?id=kK0YAQAAIAAJ

[76] R. Gomes, J. Henriques, L. Gato, A. Falcão, and C. Guedes Soares, "Testing of a small-scale model of a heaving floating owc in a wave channel and comparison with numerical results," *Renewable Energies Offshore (ed. C. Guedes Soares)*, pp. 445–454, 2015.

[77] R. Gomes, J. Henriques, L. Gato, and A. d. O. Falcão, "Wave channel tests of a slack-moored floating oscillating water column in regular waves," in *Proceedings of the 11th European Wave and Tidal Energy Conference, Nantes, France*, 2015.

[78] V. Harnois, K. Collins, D. Greaves, B. Howey, R. Gomes, J. Portillo, P. Vicente, and M. Vicente, "D6.4 - validated numerical simulation of hydrodynamic interaction between devices for different compact array layouts," WETFEET, Deliverable 6.4, Dec 2017.

[79] R. Gomes, J. Henriques, L. Gato, and A. Falcão, "Wave power extraction of a heaving floating oscillating water column in a wave channel," *Renewable Energy*, vol. 99, pp. 1262–1275, 2016.

[80] A. Babarit, "A database of capture width ratio of wave energy converters," *Renewable Energy*, vol. 80, pp. 610 – 628, 2015. [Online]. Available: http://www.sciencedirect.com/science/article/pii/S0960148115001652

[81] OFGEM. (2011, 01). [Online]. Available: https://www.ofgem.gov.uk/ofgem-publications/76112/domestic-energy-consump-fig-fs.pdf

[82] "Model-prototype similarity of oscillating-water-column wave energy converters," *International Journal of Marine Energy*, vol. 6, pp. 18 – 34, 2014. [Online]. Available: http://www.sciencedirect.com/science/article/pii/S2214166914000058

[83] L. Johanning, G. H. Smith, and J. Wolfram, "Measurements of static and dynamic mooring line damping and their importance for floating wec devices," *Ocean Engineering*, vol. 34, no. 14-15, pp. 1918–1934, 2007.

[84] D. N. Veritas, "Offshore standard dnv-os-e301 position mooring," *Det Norske Veritas: Høvik, Norway*, 2010.

[85] S. Banfield, T. Versavel, R. Snell, R. Ahilan *et al.*, "Fatigue curves for polyester moorings-a state-of-the-art review," in *Offshore Technology Conference*, vol. 12175. Offshore Technology Conference, 2000.

9

Appendix

9.1 Pugh Matrix

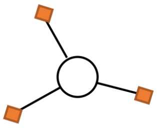

Individually moored

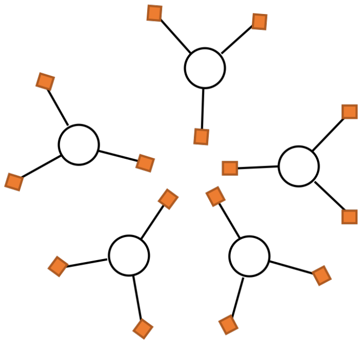

Hexagon

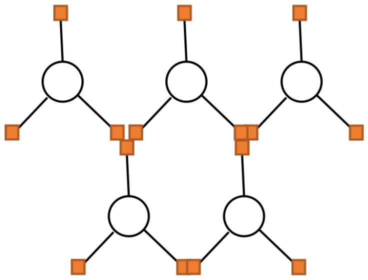

Staggered

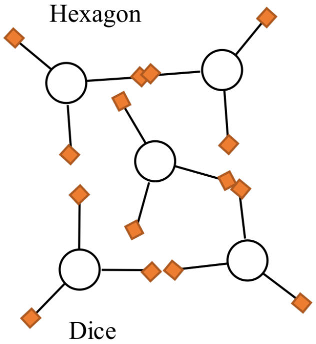

Dice

	Weighting	Individually moored	Hexagon	Staggered	Dice
Redundancy	18	0	-1	-1	1
All units accessible for maintenance	13	0			
Survivability	18	0	0	0	0
No Clashing of devices	18	0	0	0	0
No of anchors	13	0	1	1	1
Directional dependency	13	0	0	-1	0
Ability to replace components	8	0	0	-1	-1
Manufacture	8	0	0	0	0
Risk of mooring tangle	10	0	1	1	1
Simple installation	10	0	1	1	1
Pugh Score	129	0	2	0	3
Kesselring score		0	15	-6	43

9.2 Anchor Positions

Table 9.1: Anchor positions for all configurations

Device	**Configuration**	**X [m]**	**Y [m]**
TM1	A	-0.970	-7.143
TM1	A	1.953	1.468
TM1	A	-6.965	-0.306
TM2	A	-7.143	0.970
TM2	A	1.468	-1.953
TM2	A	-0.306	6.965
TM3	A	-1.688	-4.971
TM3	A	5.149	1.024
TM3	A	-3.462	3.947
TM4	A	-1.468	1.953
TM4	A	0.306	-6.965
TM4	A	7.143	-0.970
TM5	A	6.965	0.306
TM5	A	0.970	7.143
TM5	A	-1.953	-1.468
TM5	B	5.108	7.123
TM5	B	7.123	5.108
TM2	B	-5.108	7.123
TM2	B	-7.123	5.108
TM1	B	-5.108	-7.123
TM1	B	-7.123	-5.108
TM4	B	7.123	-5.108
TM4	B	5.108	-7.123
TM5	C	6.590	6.590
TM2	C	-6.590	6.590
TM1	C	-6.590	-6.590
TM4	C	6.590	-6.590
TM5	D	6.590	6.590
TM2	D	-6.590	6.590
TM1	D	-6.590	-6.590
TM4	D	6.590	-6.590

9.3 Full RAO Motion Responses

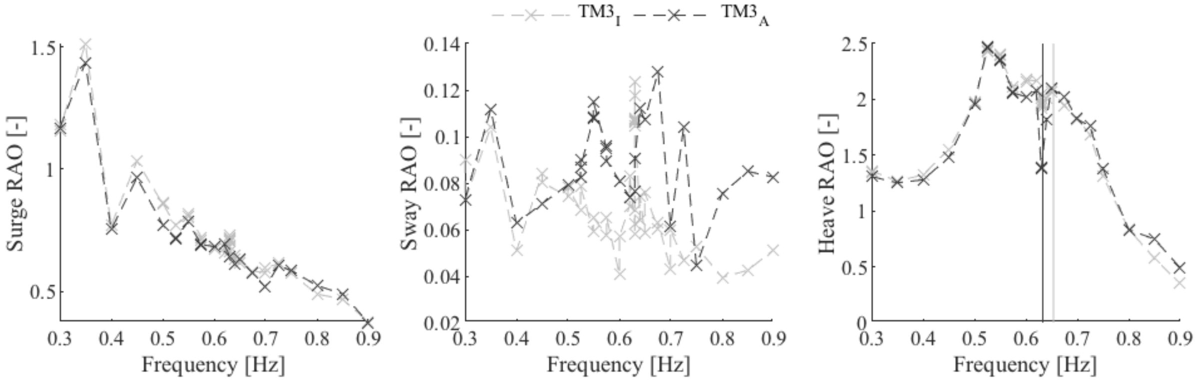

(a)Surge (b)Sway (c)Heave

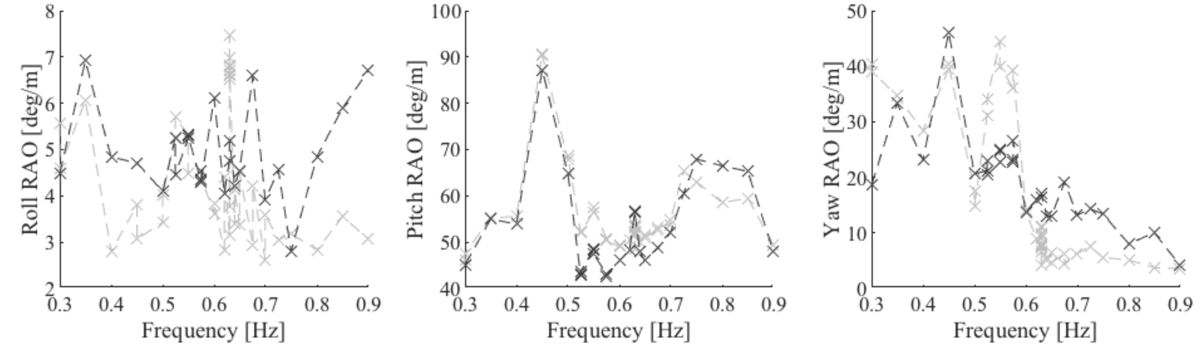

(d)Roll (e)Pitch (f)Yaw

Figure 9.1: Motion response amplitude operators for device $TM3_I$ and $TM3_A$, highlighting the array effects. Motions are surge, sway, heave, roll, pitch and yaw, (a)-(f) respectively. Vertical black and grey lines indicate the natural frequencies calculated from decay tests from Configuration A and an isolated device respectively.

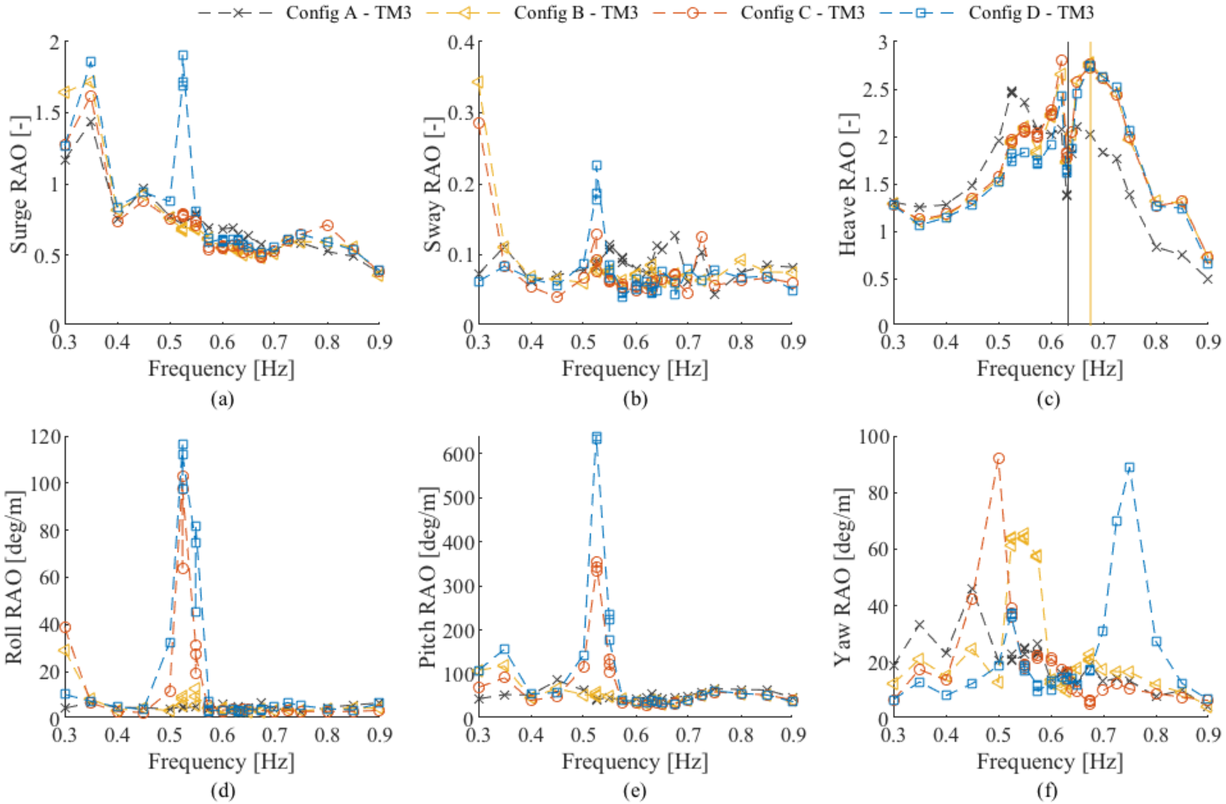

Figure 9.2: Motion response amplitude operators for the inner device ($TM3$) of the arrays in all configurations. Motions are surge, sway, heave, roll, pitch and yaw, (a)-(f) respectively. Vertical black and orange lines indicate the natural frequencies calculated from decay tests from Configuration A and B respectively.

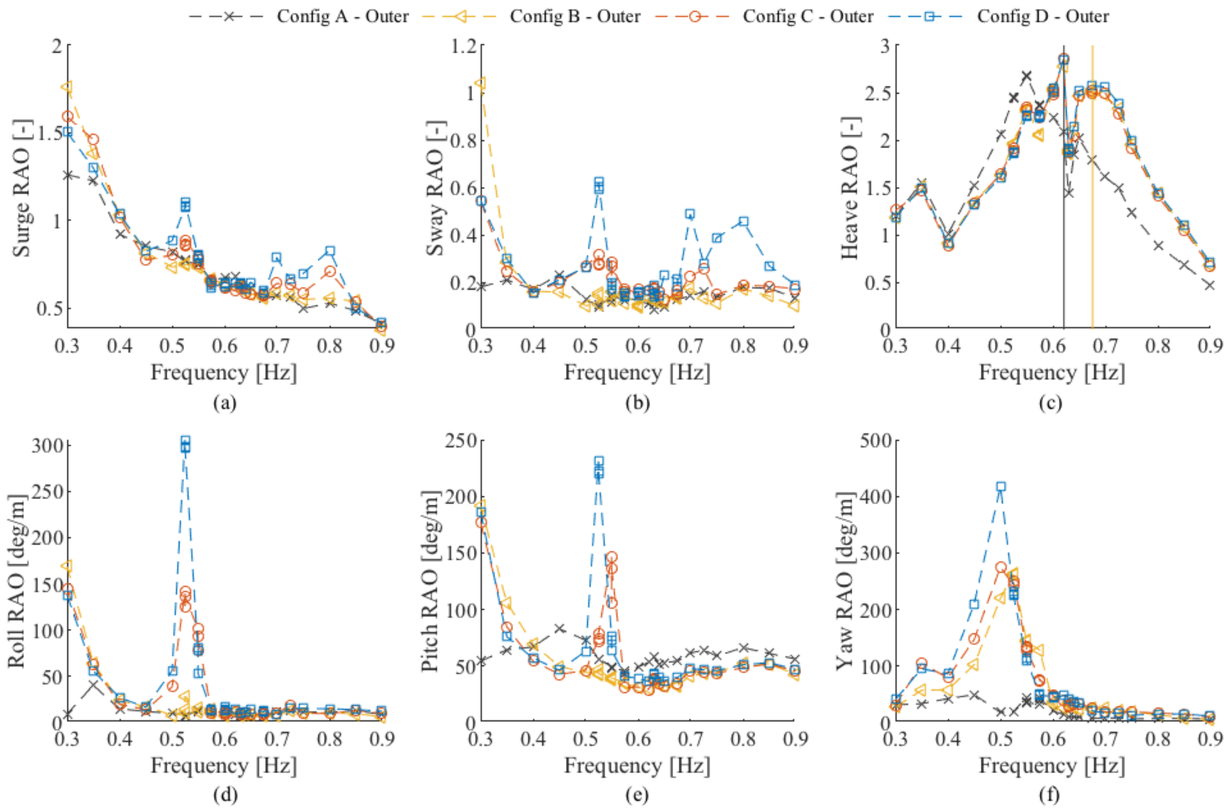

Figure 9.3: Average motion response amplitude operators for the outer devices (TMO) of the arrays in all configurations. Motions are surge, sway, heave, roll, pitch and yaw, (a)-(f) respectively. Vertical black and orange lines indicate the natural frequencies calculated from decay tests from Configuration A and B respectively.

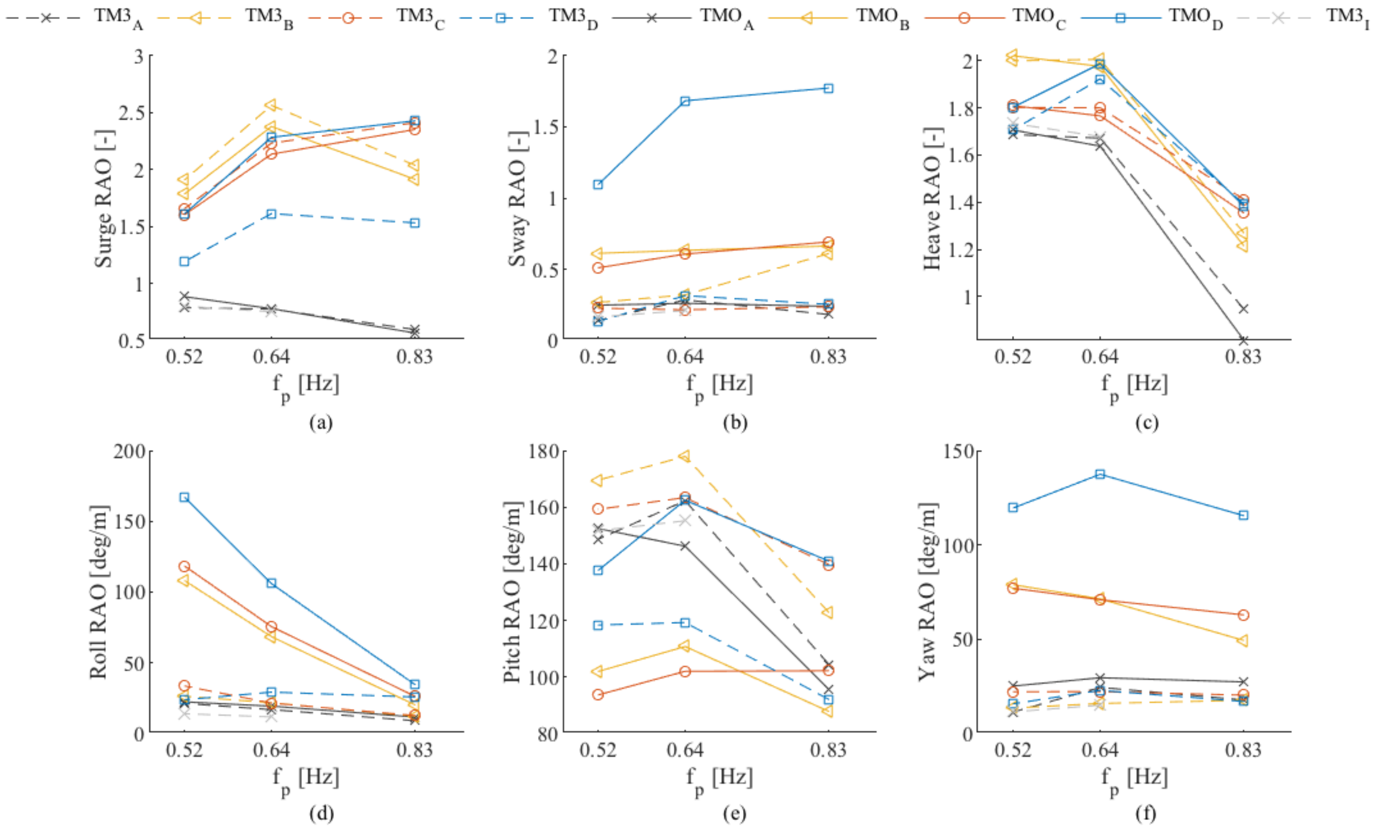

Figure 9.4: Array *rms* motion responses for irregular cases with dashed lines for $TM3$ and solid lines for the average of the outer devices. Degrees of freedom are surge, sway, heave, roll, pitch and yaw, (a)-(f) respectively.

9.4 SparBuoy Manufacturing Drawings

MARINE SCIENCE & ENGINEERING WITH PLYMOUTH UNIVERSITY

ITEM NO.	PART NUMBER	DESCRIPTION	QTY.
1	OWC	Purchased to length from manufacturer	1
2	Floater	Purchased to length from manufacturer	1
3	InnerCone	Laser cut from 2mm Aluminium	1
4	TopEndRing	CNC turned from Aluminium	1
5	OuterCone	Laser cut from 2mm Aluminium	1
6	Ballast1	CNC turned from Aluminium	1
7	Lid	turned from 10mm Acrylic	1
8	FloaterBase	Laser cut from 2mm Aluminium	1
9	CounterDisk1	Water jet cut from 16mm Aluminium	1
10	CounterDisk2	Water jet cut from 16mm Aluminium	1
11	PTORing	Laser cut from 10mm Acrylic	1
12	PTOorifice	Laser cut from 3mm Acrylic	1
13	CounterWeight	Cut and turned from 50mm rod	4
14	B18.3.5M - 5 x 0.8 x 20 Socket FCHS -- 20C		4
15	B18.3.5M - 4 x 0.7 x 10 Socket FCHS -- 10C		4
16	Oring	Made from 5mm silicon cord	1
17	Oring2	Made from 5mm silicon cord	1
18	Jubilee Clip-Size 12_5-300mm Dia	Worm Drive Hose Clip Mild Steel and Stainless Steel	1
19	PressureRing	3D printed from STL file	1
20	Rod	M8 stainless steel studding	4

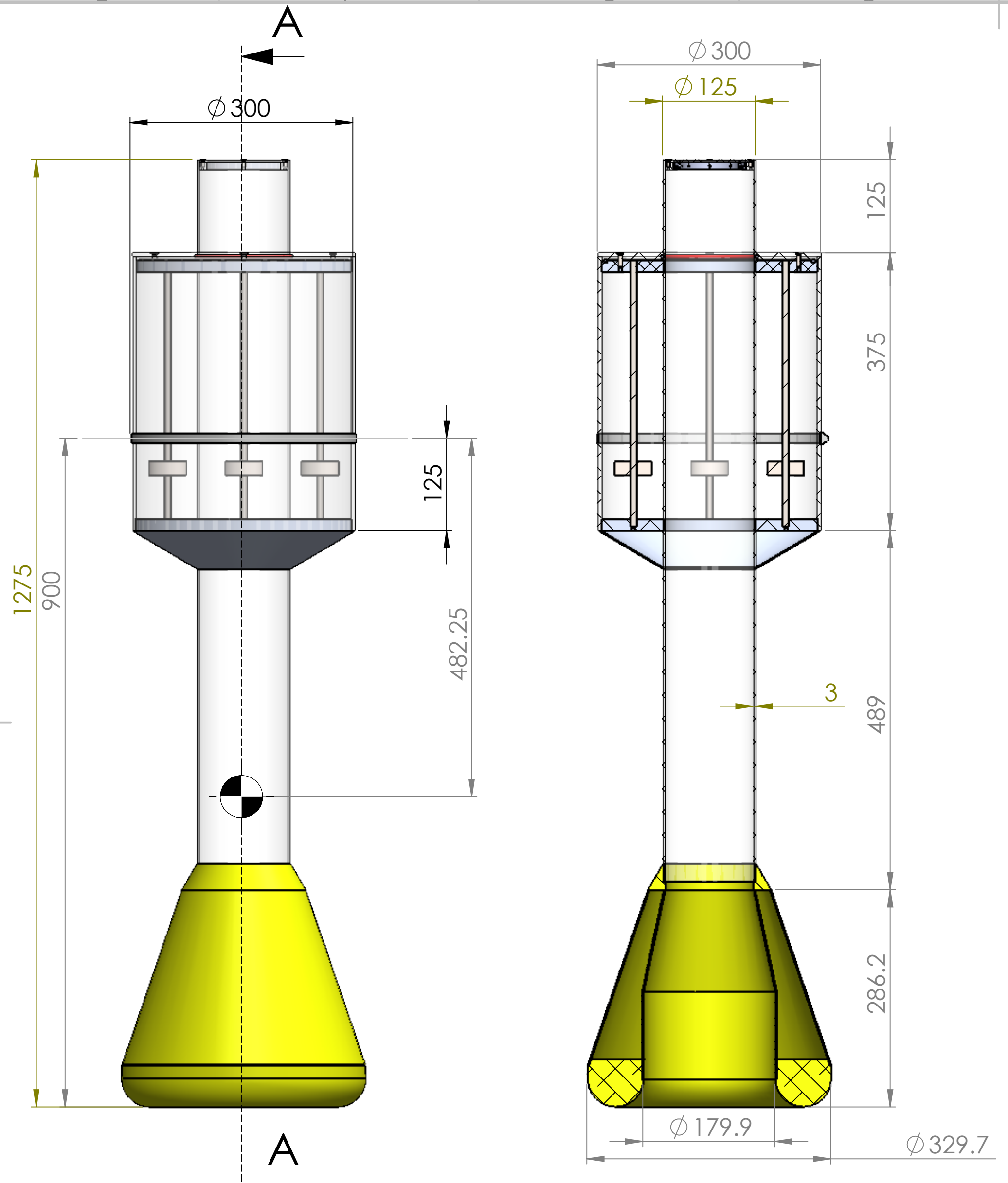

SECTION A-A

Total mass - 18.88 Kg
Ballast - 8.92 Kg
Iyy (=Ixx) - 3.83 Kg m2
Izz - 0.28 Kg m2
zg - -482.25 mm

Aluminium density - 2700 Kg/m3
Acrylic density - 1200 Kg/m3
Water density - 1000 Kg/m3

Moments about CoM

SOLIDWORKS Educational Product. For Instructional Use Only

UNLESS OTHERWISE SPECIFIED:
DIMENSIONS ARE IN MILLIMETERS
SURFACE FINISH:
TOLERANCES:
LINEAR:
ANGULAR:

FINISH:

DEBURR AND BREAK SHARP EDGES

DO NOT SCALE DRAWING

REVISION

	NAME	SIGNATURE	DATE
DRAWN	Ben Howey		12/10/2016
CHK'D			
APPV'D			
MFG			
Q.A			

TITLE:
Plymouth University
1:40th SparBuoy - TMX

MATERIAL: Aluminium
Stainless Steel
Acrylic

DWG NO.
SparBuoy001

A3

WEIGHT: 18873.74 g

SCALE:1:7

SHEET 1 OF 13

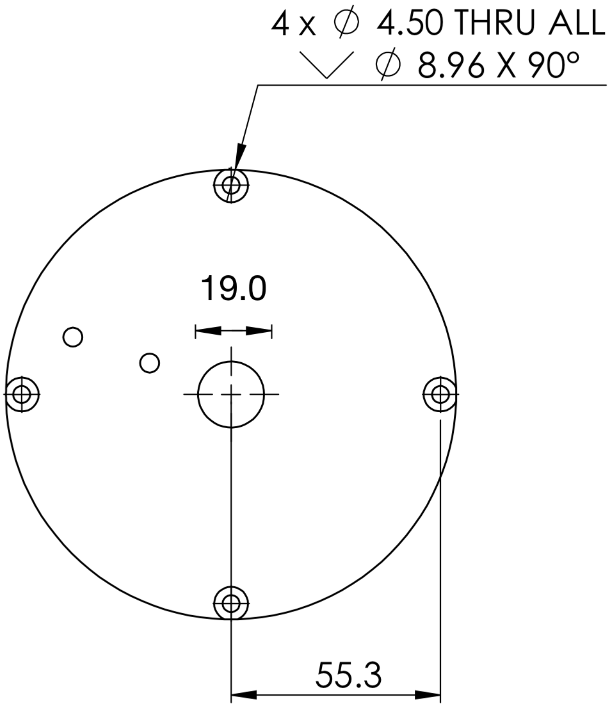

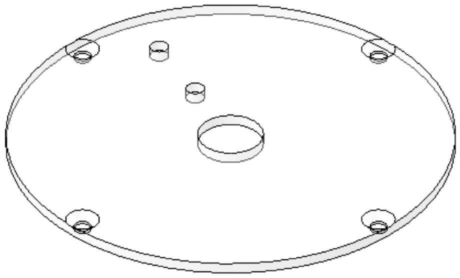

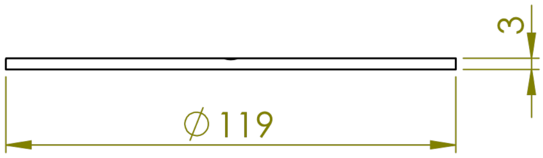

Mass = 38.58 g

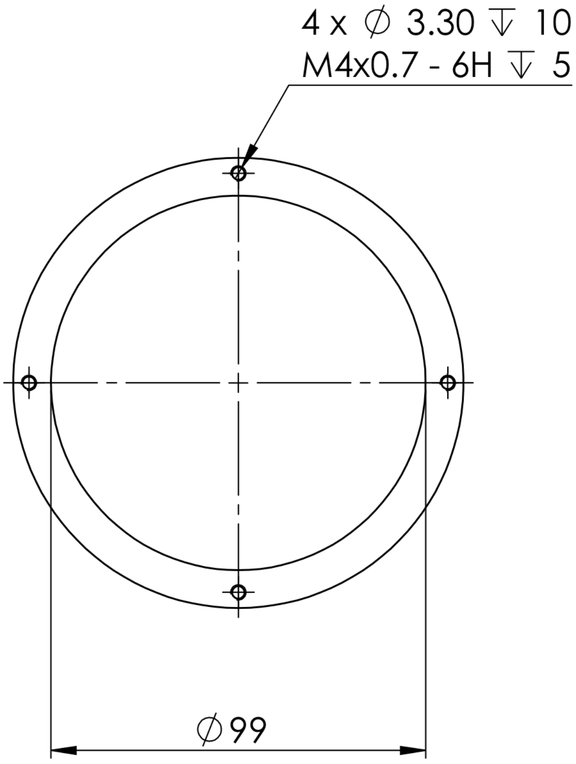

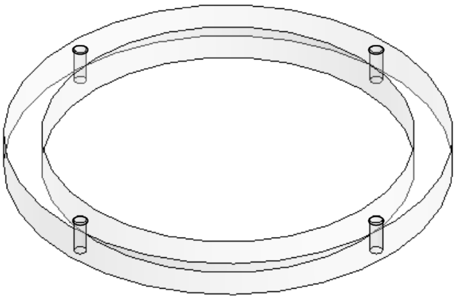

Mass = 40.68 g

UNLESS OTHERWISE SPECIFIED:
DIMENSIONS ARE IN MILLIMETERS
SURFACE FINISH:

TOLERANCES:
x. 1mm/1 deg
.x .1mm/.1 deg
.xx .01mm/.01 deg

FINISH: DEBUR AND
BREAK SHARP
EDGES

DO NOT SCALE DRAWING

REVISION 1A

	NAME	SIGNATURE	DATE
DRAWN	Ben Howey		01/07/16
CHK'D			
APPV'D			
MFG			
Q.A			

MATERIAL:
Acrylic (Medium-high impact)

WEIGHT:

TITLE:

SparBuoy PTO Assem

DWG NO.

SB_PTO_001

A4

SCALE:1:2

SHEET 2 OF 13

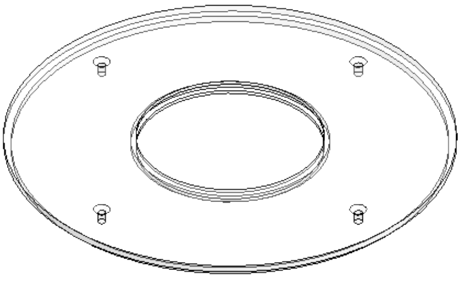

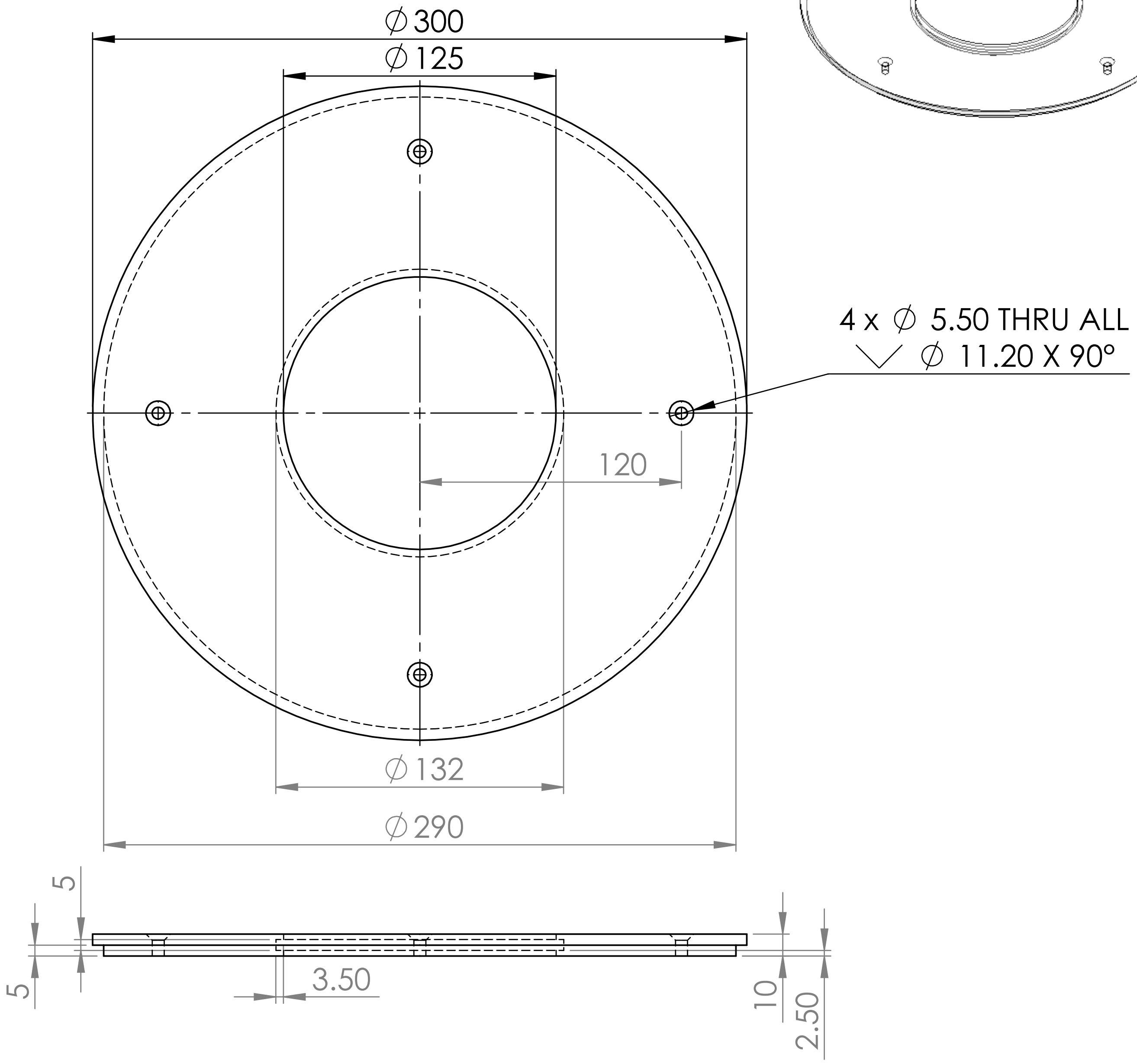

UNLESS OTHERWISE SPECIFIED: DIMENSIONS ARE IN MILLIMETERS SURFACE FINISH:	TOLERANCES: x. 1mm/1 deg .x .1mm/.1 deg .xx .01mm/.01 deg	FINISH: DEBUR AND BREAK SHARP EDGES	DO NOT SCALE DRAWING

REVISION 1A

	NAME	SIGNATURE	DATE
DRAWN	Ben Howey		01/07/16
CHK'D			
APPV'D			
MFG			
Q.A			

MATERIAL:
Acrylic (Medium-high impact

WEIGHT: 663.09 g

TITLE:

SparBuoy Lid

DWG NO. SB_LD_001

A4

SCALE:1:5

SHEET 3 OF 13

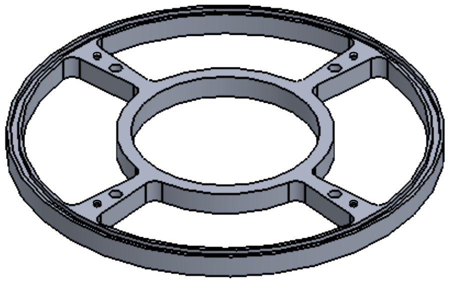

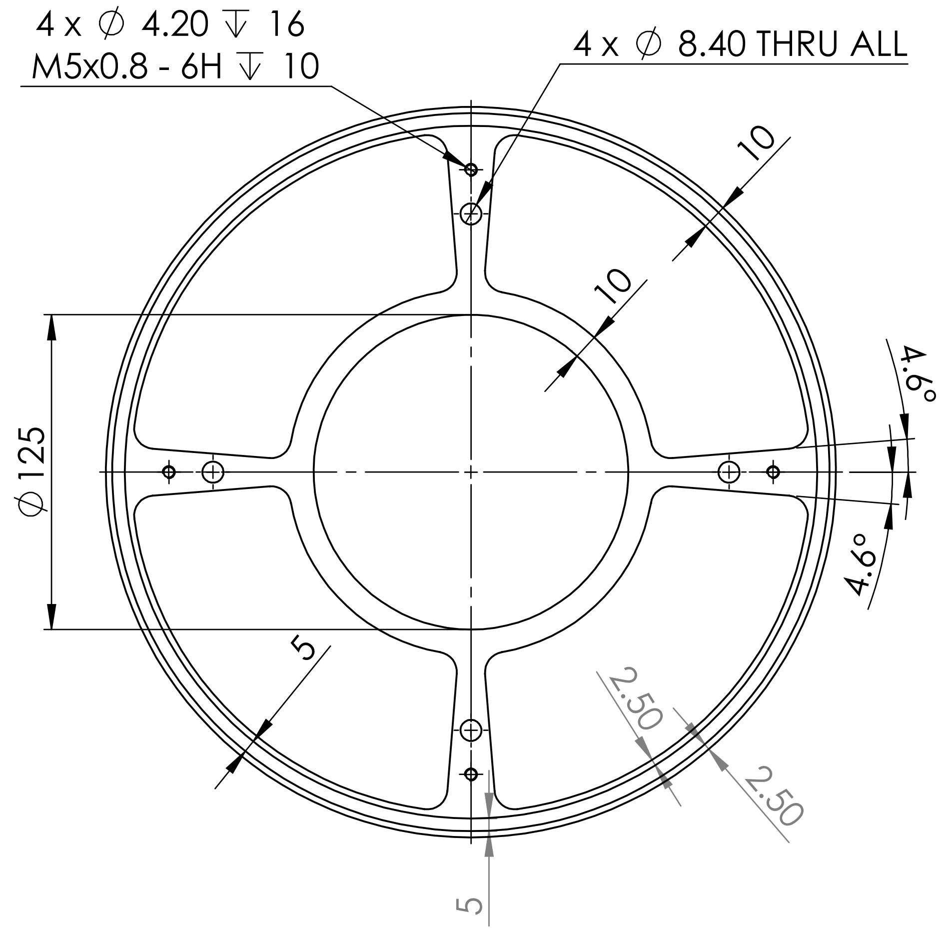

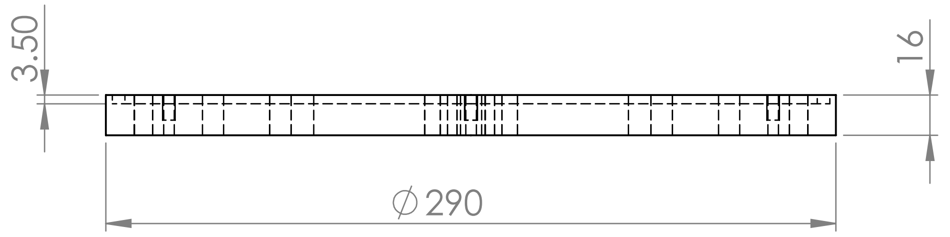

UNLESS OTHERWISE SPECIFIED:
DIMENSIONS ARE IN MILLIMETERS
SURFACE FINISH:

TOLERANCES:
x. 1mm/1 deg
.x .1mm/.1 deg
.xx .01mm/.01 deg

FINISH: DEBUR AND
BREAK SHARP
EDGES

DO NOT SCALE DRAWING

REVISION 1A

	NAME	SIGNATURE	DATE
DRAWN	Ben Howey		01/07/16
CHK'D			
APPV'D			
MFG			
Q.A			

MATERIAL:
1060 Alloy

WEIGHT: 681.13 g

TITLE:

SparBuoy Counter Disk 2

DWG NO. SB_CD2_001

A4

SCALE:1:3

SHEET 4 OF 13

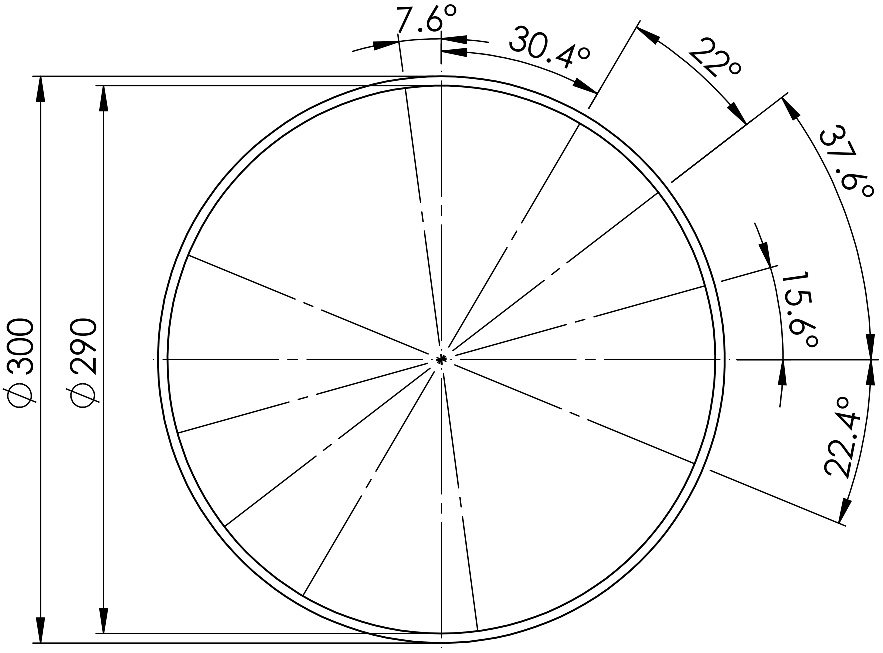

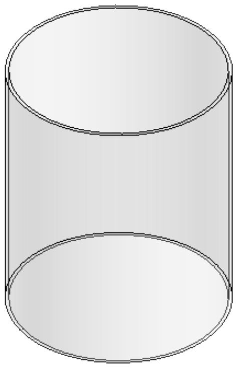

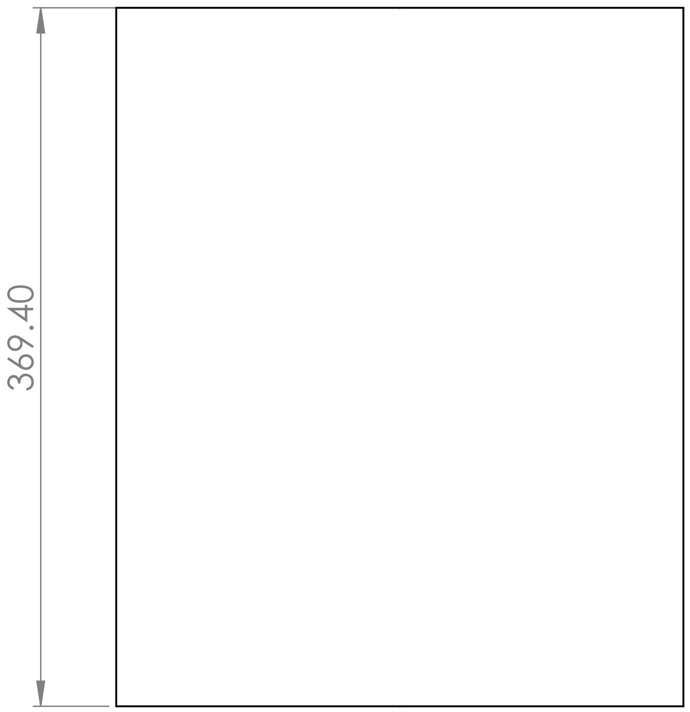

UNLESS OTHERWISE SPECIFIED:
DIMENSIONS ARE IN MILLIMETERS
SURFACE FINISH:

TOLERANCES:
x. 1mm/1 deg
.x .1mm/.1 deg
.xx .01mm/.01 deg

FINISH: DEBUR AND BREAK SHARP EDGES

DO NOT SCALE DRAWING

REVISION 1A

	NAME	SIGNATURE	DATE
DRAWN	Ben Howey		01/07/16
CHK'D			
APPV'D			
MFG			
Q.A			

MATERIAL:
Acrylic (Medium-high impact

WEIGHT: 2.059 Kg

TITLE:

Floater

DWG NO.

SB_Fl_001

A4

SCALE:1:4

SHEET 5 OF 13

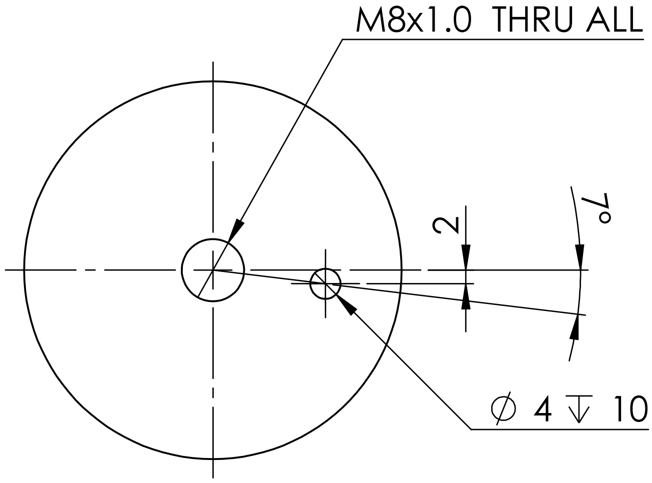

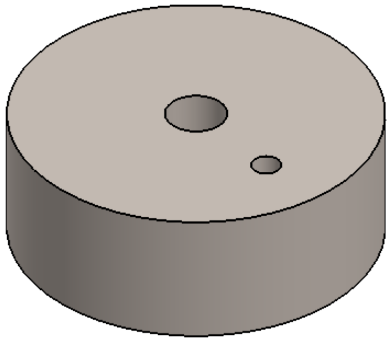

4 Off Counter Weight

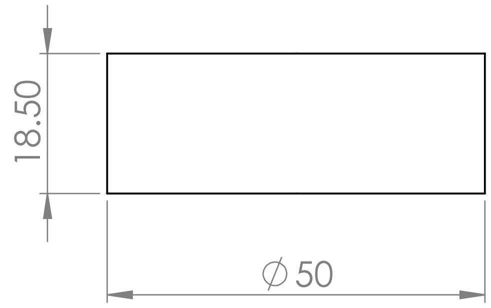

Mass = 276.71 g

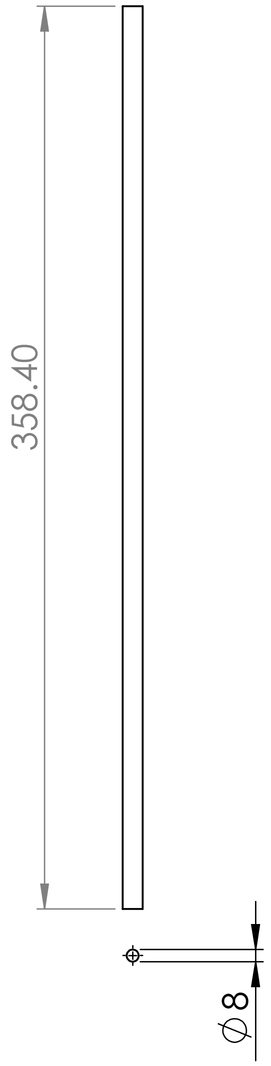

4 Off threaded M8 rod

Mass = 141.78 g

UNLESS OTHERWISE SPECIFIED:
DIMENSIONS ARE IN MILLIMETERS
SURFACE FINISH:

TOLERANCES:
x. 1mm/1 deg
.x .1mm/.1 deg
.xx .01mm/.01 deg

FINISH: DEBUR AND
BREAK SHARP
EDGES

DO NOT SCALE DRAWING

REVISION 1A

	NAME	SIGNATURE	DATE
DRAWN	Ben Howey		01/07/16
CHK'D			
APPV'D			
MFG			
Q.A			

MATERIAL:
201 Annealed Stainless Steel (SS)

WEIGHT:

TITLE:

SparBuoy Counter Weightand Rod

DWG NO.

SB_CWR_001

A4

SCALE:

SHEET 6 OF 13

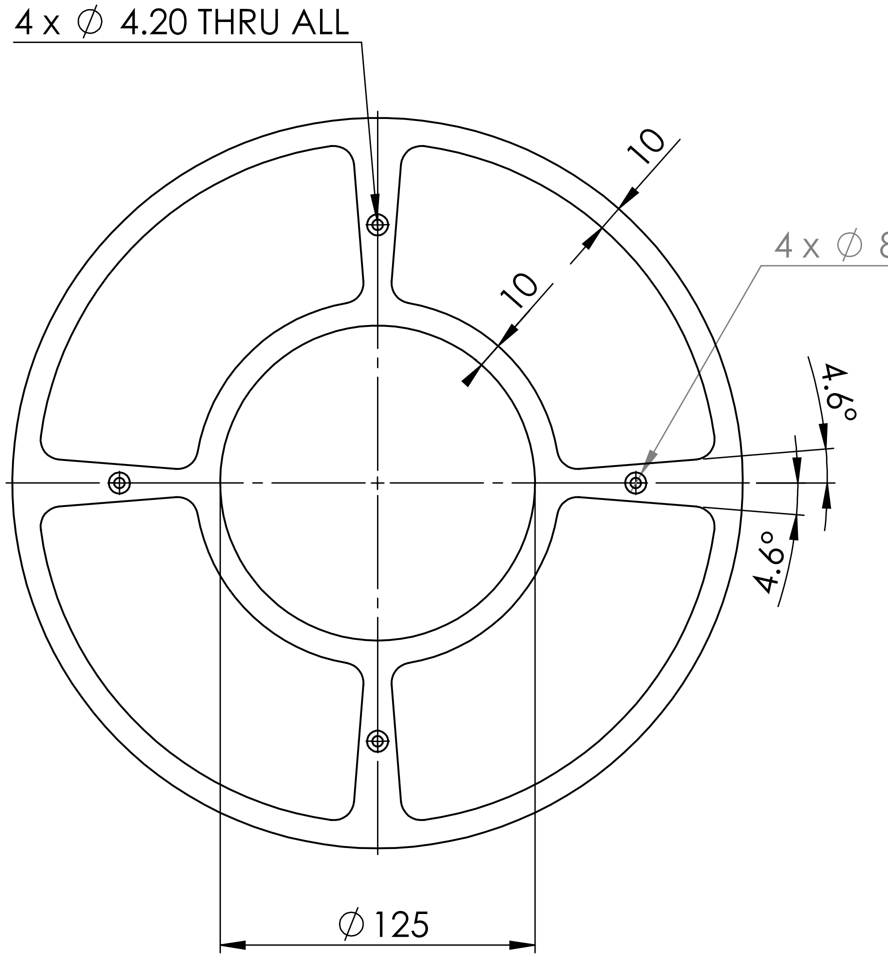

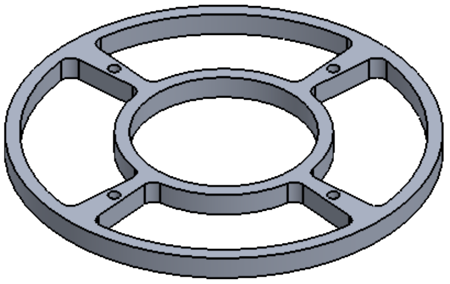

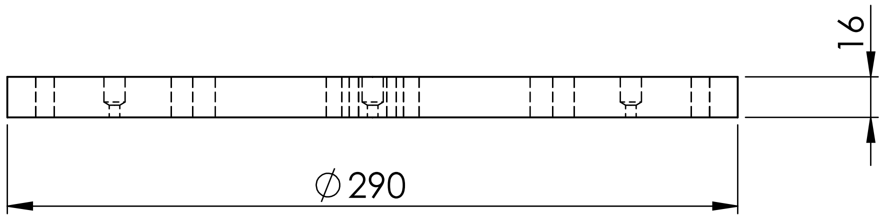

UNLESS OTHERWISE SPECIFIED: DIMENSIONS ARE IN MILLIMETERS SURFACE FINISH:	TOLERANCES: x. 1mm/1 deg .x .1mm/.1 deg .xx .01mm/.01 deg	FINISH: DEBUR AND BREAK SHARP EDGES

	NAME	SIGNATURE	DATE
DRAWN	Ben Howey		01/07/16
CHK'D			
APPV'D			
MFG			
Q.A			

MATERIAL:
1060 Alloy

WEIGHT: 0.73 Kg

DO NOT SCALE DRAWING

REVISION 1A

TITLE:

SparBuoy Counter Disk1

DWG NO. SB_CD1_001

A4

SCALE:1:3

SHEET 7 OF 13

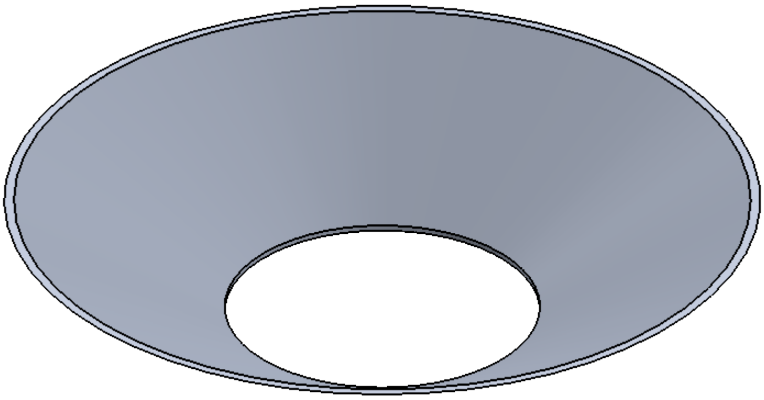

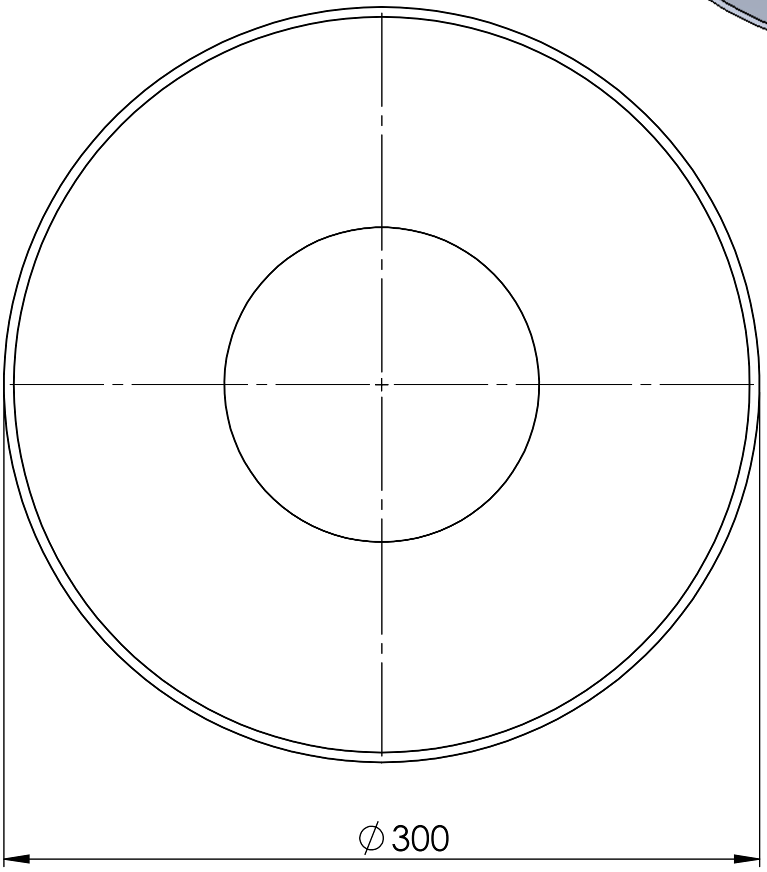

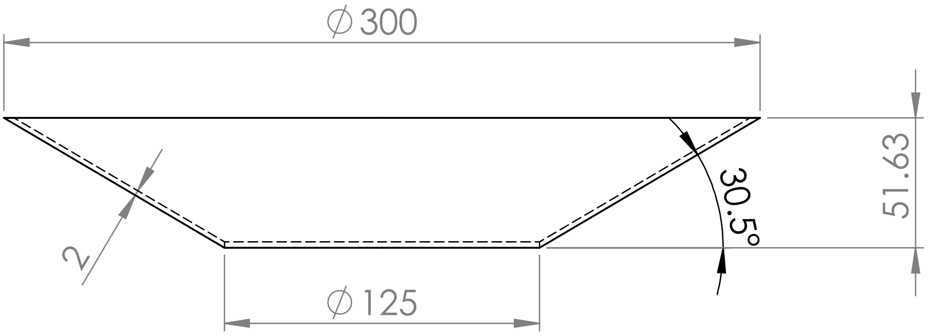

UNLESS OTHERWISE SPECIFIED: DIMENSIONS ARE IN MILLIMETERS SURFACE FINISH:	TOLERANCES: x. 1mm/1 deg .x .1mm/.1 deg .xx .01mm/.01 deg	FINISH: DEBUR AND BREAK SHARP EDGES

DO NOT SCALE DRAWING

REVISION 1A

	NAME	SIGNATURE	DATE
DRAWN	Ben Howey		01/07/16
CHK'D			
APPV'D			
MFG			
Q.A			

TITLE:

SparBuoy Floater Base

MATERIAL:
1060 Alloy

DWG NO. SB_FB_001

A4

WEIGHT: 0.35 Kg

SCALE:1:5

SHEET 8 OF 13

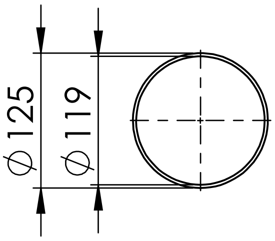

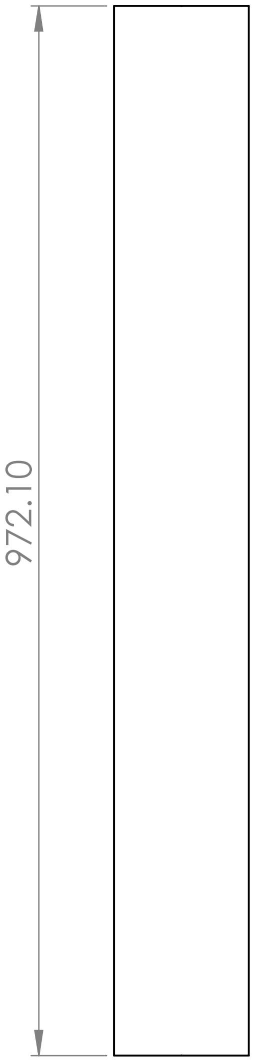

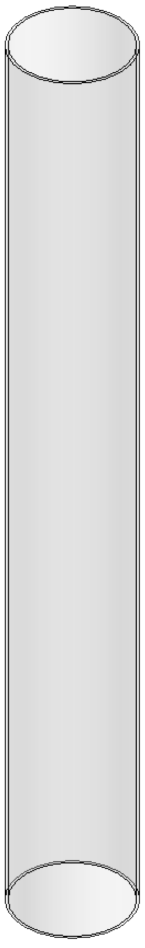

UNLESS OTHERWISE SPECIFIED: DIMENSIONS ARE IN MILLIMETERS SURFACE FINISH:	TOLERANCES: x. 1mm/1 deg .x .1mm/.1 deg .xx .01mm/.01 deg	FINISH: DEBUR AND BREAK SHARP EDGES	DO NOT SCALE DRAWING	REVISION 1A

	NAME	SIGNATURE	DATE
DRAWN	Ben Howey		01/07/16
CHK'D			
APPV'D			
MFG			
Q.A			

TITLE:

SparBuoy OWC

MATERIAL:
Acrylic (Medium-high impact)

DWG NO. SB_OWC_001

A4

WEIGHT: 1341.29 Kg

SCALE:1:5

SHEET 9 OF 13

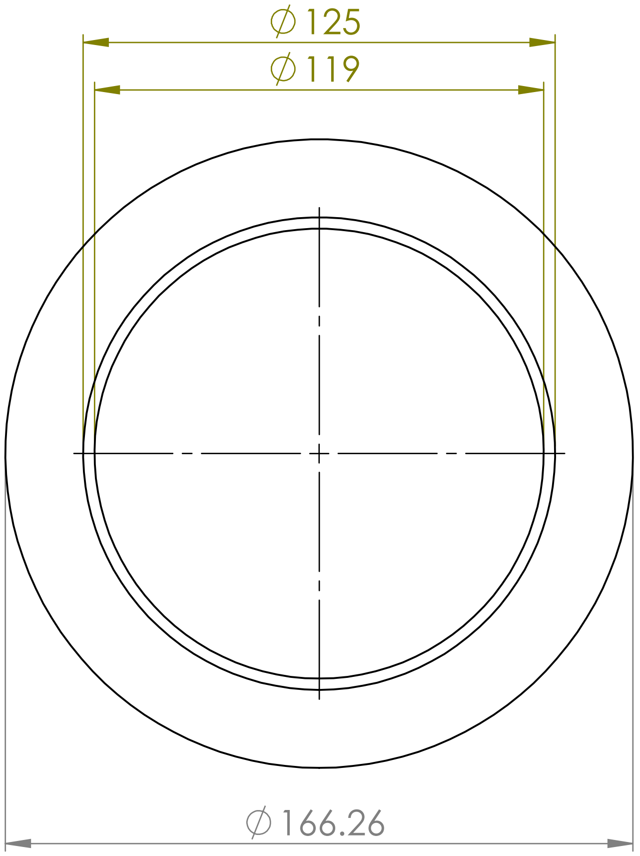

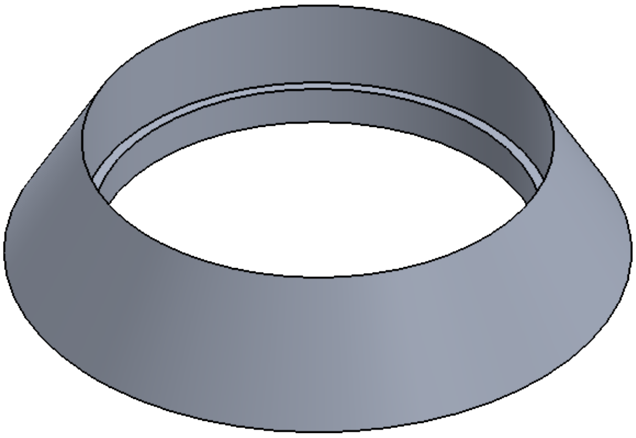

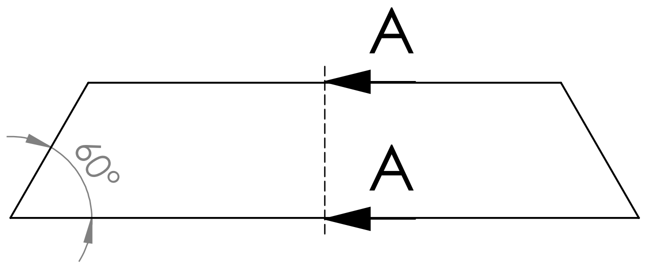

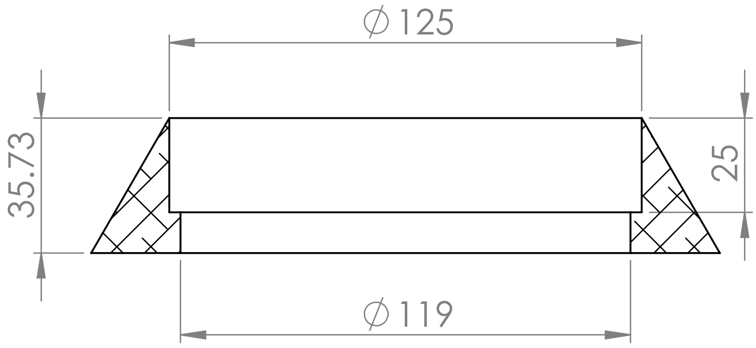

SECTION A-A

UNLESS OTHERWISE SPECIFIED:
DIMENSIONS ARE IN MILLIMETERS
SURFACE FINISH:

TOLERANCES:
x. 1mm/1 deg
.x .1mm/.1 deg
.xx .01mm/.01 deg

FINISH: DEBUR AND
BREAK SHARP
EDGES

DO NOT SCALE DRAWING

REVISION 1A

	NAME	SIGNATURE	DATE
DRAWN	Ben Howey		01/07/16
CHK'D			
APPV'D			
MFG			
Q.A			

TITLE:

SparBuoy Top end Ring

MATERIAL:
1060 Alloy

DWG NO.
SB_TER_001

A4

WEIGHT: 467.02 g

SCALE:1:5

SHEET 10 OF 13

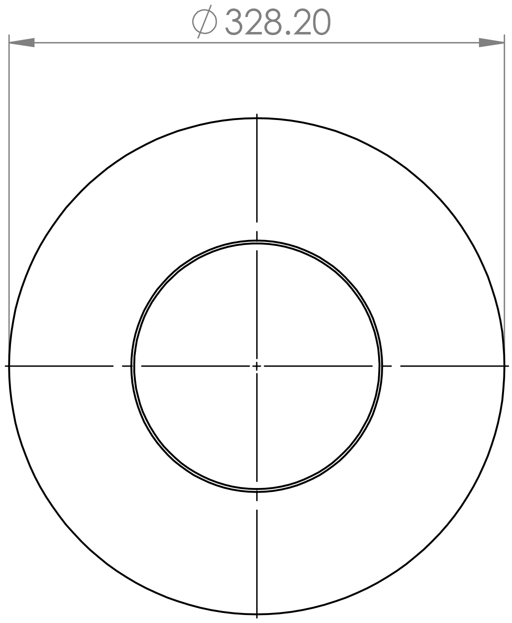

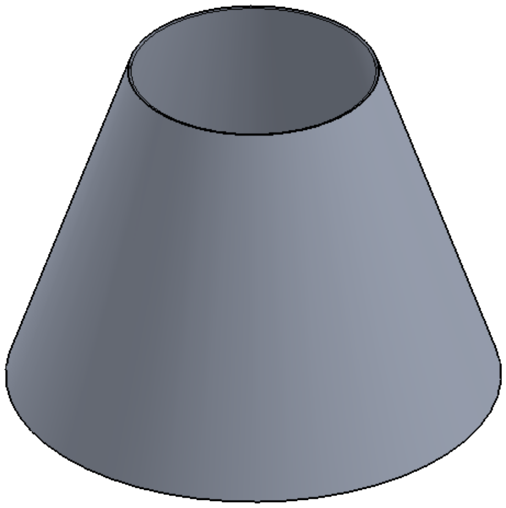

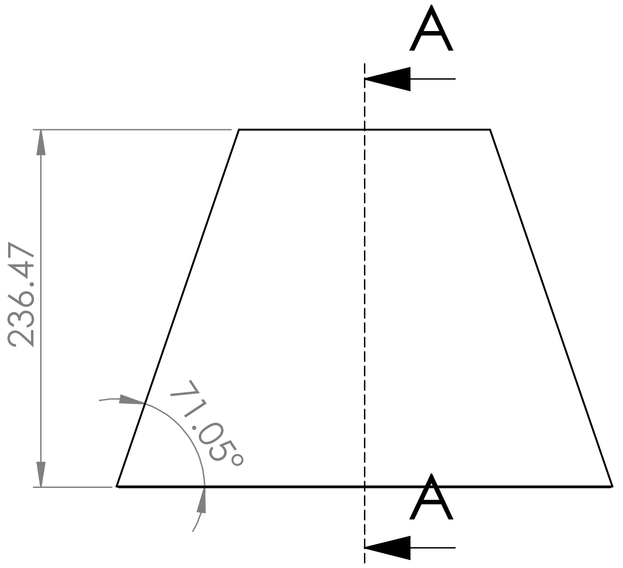

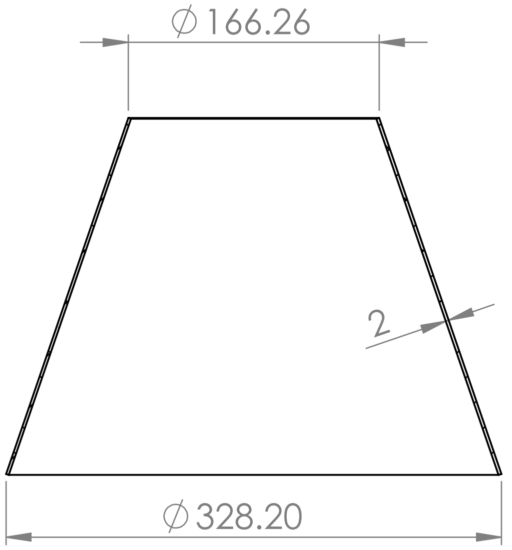

SECTION A-A

Dimensions to fit the outer dims of Ballast 1 and OWC.

UNLESS OTHERWISE SPECIFIED:
DIMENSIONS ARE IN MILLIMETERS
SURFACE FINISH:

TOLERANCES:
x. 1mm/1 deg
.x .1mm/.1 deg
.xx .01mm/.01 deg

FINISH: DEBUR AND BREAK SHARP EDGES

DO NOT SCALE DRAWING

REVISION 1A

	NAME	SIGNATURE	DATE
DRAWN	Ben Howey		01/07/16
CHK'D			
APPV'D			
MFG			
Q.A			

MATERIAL:
1060 Alloy

WEIGHT: 1037.75 g

TITLE:

Outer Cone

DWG NO. SB_OC_001

A4

SCALE:1:5

SHEET 11 OF 13

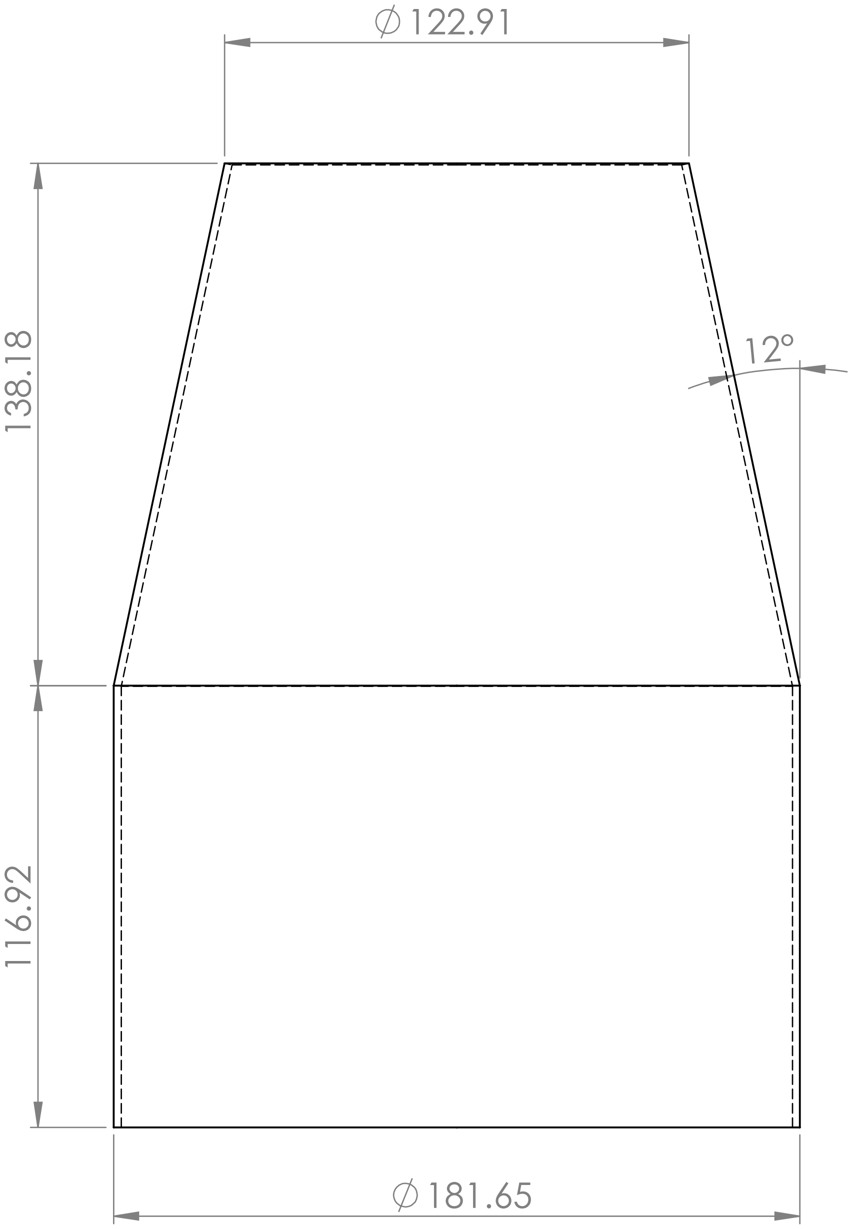

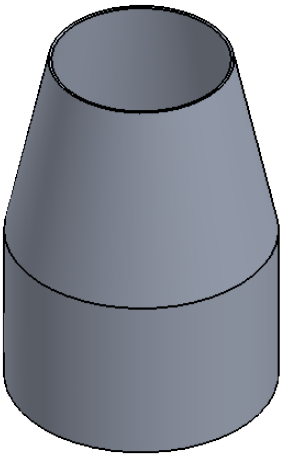

To fit Ballast 1
upper inner diameter

UNLESS OTHERWISE SPECIFIED:
DIMENSIONS ARE IN MILLIMETERS
SURFACE FINISH:

TOLERANCES:
x. 1mm/1 deg
.x .1mm/.1 deg
.xx .01mm/.01 deg

FINISH: DEBUR AND
BREAK SHARP
EDGES

DO NOT SCALE DRAWING

REVISION 1A

	NAME	SIGNATURE	DATE
DRAWN	Ben Howey		01/07/16
CHK'D			
APPV'D			
MFG			
Q.A			

TITLE:

SparBuoy Inner Cone

MATERIAL:
1060 Alloy

DWG NO. SB_IC_001

A4

WEIGHT: 0.72 Kg

SCALE:1:2

SHEET 12 OF 13

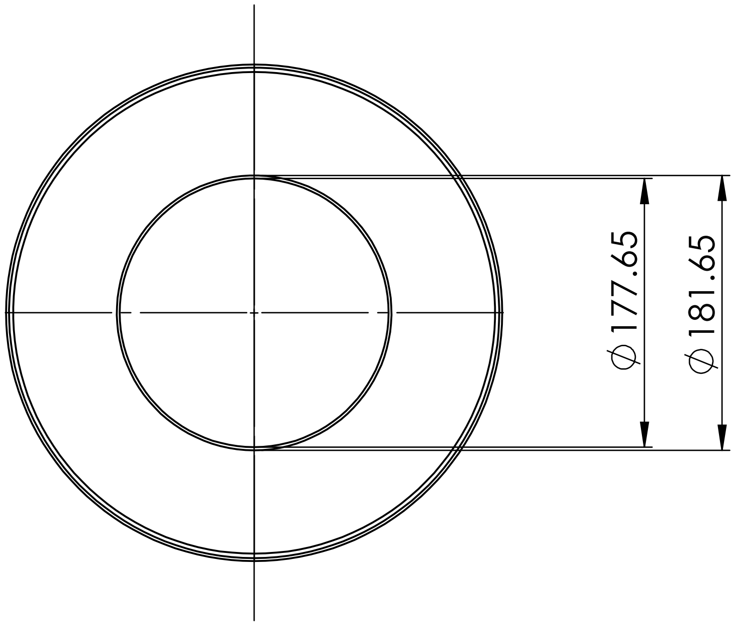

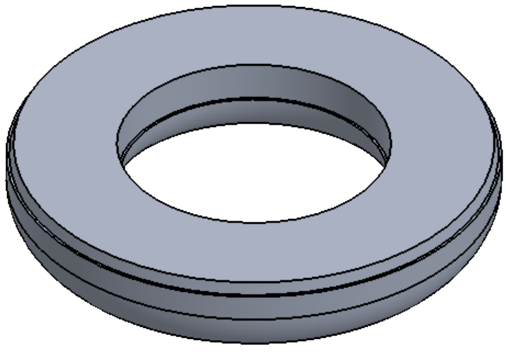

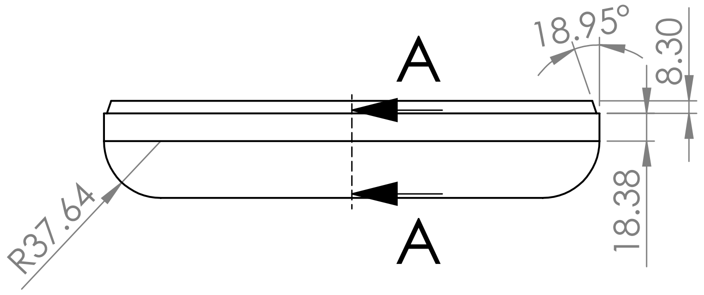

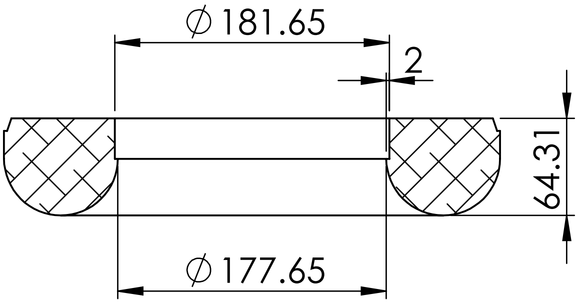

SECTION A-A

If the density of the aluminium varies from 2700 kg/m^3
the height of the part can be adjusted to achieve the part mass.

UNLESS OTHERWISE SPECIFIED: DIMENSIONS ARE IN MILLIMETERS SURFACE FINISH:	TOLERANCES: x. 1mm/1 deg .x .1mm/.1 deg .xx .01mm/.01 deg	FINISH: DEBUR AND BREAK SHARP EDGES	DO NOT SCALE DRAWING	REVISION	1A
	NAME	SIGNATURE	DATE		
DRAWN	Ben Howey		01/07/16		
CHK'D					
APPV'D					
MFG					
Q.A					

TITLE:

SparBuoy Ballast 1

SOLIDWORKS Educational Product. For Instructional Use Only

MATERIAL:
1060 Alloy

DWG NO. SB_Ballast1_001 A4

WEIGHT: 8.92 Kg

SCALE:1:5

SHEET 13 OF 13